Lunar Mineralogy with SIR-1 and Clementine UVVIS/NIR

Legend (plot):
- • SIR−1 spectrum
- ○ 3 UVVIS filter
- — Model spectrum

Bar chart legend:
- Agglutinate
- Ilmenite
- Plagioclase
- Augite
- Pigeonite
- Orthopyroxene
- Fe−Clinopyroxene
- Olivine

Manuela Wiese

International Max Planck Research School
on Physical Processes in the Solar System and Beyond
at the Universities of Braunschweig and Göttingen

Lunar Mineralogy with SIR-1 and Clementine UVVIS/NIR

Dissertation

zur Erlangung des Doktorgrades

der Mathematisch-Naturwissenschaftlichen Fakultäten

der Georg-August-Universität zu Göttingen

vorgelegt von

Manuela Wiese

aus Frankfurt/Oder

Göttingen 2009

Contents

Contents

4

List of Figures

List of Tables

Summary

Within this thesis the mineralogy of the moon is investigated. To this end remotely sensed reflectance spectra in the near infrared observed with the SIR-1 point spectrometer during the SMART-1 mission are analyzed in combination with Clementine UVVIS/NIR camera images. I introduce a suite of tools for combining both datasets. First an interactive, automated lightcurve alignment procedure corrects for slight differences in the coordinate systems of both instruments, resulting in general consistency of both datasets. Hence the reproducibility of remote measurements from lunar orbit is proven. Second, an automatic detection routine extracts less weathered spectra with strong absorption features from the 28 million reflectance spectra taken by SIR-1. Thereby 10000 "active spectra" were identified and are now available for further studies of unweathered surface features observed with SIR-1. Finally, a regolith reflectance model based on the bidirectional reflectance theory, made accessible through a graphical user interface, models the mineral compositions from these spectra. Case studies of selected spectra from Mare Humorum and the Mare Crisium area including Mare Anguis were conducted, and results are presented in this thesis.

1   INTRODUCTION

"Der Mond ist unsere Sonne"

Moonbootica feat. Jan Delay

For millions of years the Moon has occupied the thoughts of mankind. This dry, rocky wasteland, with bright highlands and dark plains, heavily cratered by millions of violent impacts, inspired early concepts of other worlds like our own. Unlike the Earth the Moon cannot be easily accessed by geologic fieldwork. Thus, aside from returned material from nine sites visited by the Apollo and Luna spacecrafts, our knowledge of the vast majority of the surface comes from remotely sensed data.

As we leave fingerprints when touching a glass of water, the Moon leaves fingerprints in the reflected sunlight when interacting with the solar radiation in the upper micrometers of its surface. In this thesis, I will track those fingerprints back to the minerals of the lunar surface that caused them.

To achieve this, I analyzed solar light reflected by the lunar surface in the visible and near infrared wavelength range. At these wavelengths the most abundant lunar minerals leave clear traces of their existence and composition. This thesis is based on data from the SIR-1 infrared spectrometer. SIR-1 was developed and built by the Max-Planck-Institute for Solar System Research. The instrument was sent on board the SMART-1 mission to the Moon were it took around 28 million reflectance spectra of the lunar surface. Combining and analyzing these spectra, along with the images available from the UVVIS and NIR cameras from the Clementine mission, is the aim of this thesis. With this type of analysis for the first time reflectance spectra taken from lunar orbit by two different missions could be shown to agree on a large number of surface sites. The verification of these space-based measurements boosted confidence for further combined interpretation of the two datasets.

Because the Moon is a very dry planetary body, the mineralogy of the lunar surface is much simpler than that of Earth. During its violent formation most of the water and other volatiles evaporated, although wet impactors could have added some water later that could have been stored in permanently shadowed craters at the lunar poles. These theoretically predicted deposits of ice at the lunar poles are not yet beyond dispute. Lack of water on the Moon precludes all those minerals that contain water or need water as a major agent to form, leaving us with a restricted sample of about 100 minerals identified in lunar sam-

ples. Most are present in insignificant amounts only relevant to laboratory analysis but not for remote sensing. Our analysis focuses on four major minerals that account for most of the lunar surface materials, namely the silicates plagioclase, pyroxene, and olivine and the oxide mineral ilmenite. Some of these minerals belong to mineral families and mineral solid solution series, where the composition varies between endmembers due to successive exchange of elements, and thus their spectral characteristics vary.

Materials on the lunar surface are not just a pure mixture of the above mentioned minerals. Rather, they represent highly complex conglomerates composed of pure mineral grains, glasses created by impacts or pyroclastic eruptions, amorphous rims from deposition of vaporised rocks and all possible combinations of these welded together by the action of frequent small impacts at the lunar surface. These highly evolved materials cover the surfaces of atmosphereless rocky bodies in the solar system and are called regoliths. Also the Earth's surface is covered by a kind of regolith that we call soil, but which has a completely different formation history than lunar regolith. The complexity of the lunar regolith complicates the analysis and the modeling efforts. Fortunately the extensive laboratory analysis of the returned samples from the Apollo missions provides additional information to increase the reliability of our geological models.

Based on the theory of bidirectional reflectance developed by Bruce Hapke (Hapke 1981) which provides the background to compose an intimate mixture of several mineral endmembers, a model software for regolith reflectance was developed. A graphical user interface also developed during this thesis, grants easy access to all people wishing to analyze lunar reflectance spectra between 0.4 and 2.7 micrometer.

While the complex character of the upper regolith is mainly caused by an accumulation of the effects of many small impacts and constant solar wind exposure the large scale structure of the lunar surface is a result of the big basin forming events, which became extremely rare in our era but were much more frequent when the moon and the solar system were still young. Planetesimals, the remnants of solar system formation reshaped the solidified early crust of the Moon. Large scale ejecta piled up to form the lunar highlands and mountain chains and left deep basins to be filled by lava from deeper strata of the lunar crust and mantle through surface cracks and shattered bedrock produced by giant impacts.

From lunar orbit we can only see the outermost layer of the Moon. The depth to which we can observe is depending on the wavelength range we employ. The reflected light measured in the near infrared originates in the upper micrometer of the lunar surface, while ground penetrating radar observations can reach hundreds of meters deep into the surface, depending on their energy and the material observed. This restricts our remote investigations of the Moon to its outermost layer at the crustal highlands, and to the samples we have from deeper strata in the form of mare basalts.

12

1.1 Highlands and Crust

The crust represents the outermost layer of a differentiated planetary body. On the Moon the visible bright areas, the highlands, are what we see from the lunar crust. Those highlands consist of large-scale rock fragments ejected by big impacts. Even if these impacts probably did not penetrate through the crust into the mantle, deep enough to mix crustal and mantle material, they still caused a moon-wide displacement of crustal material. So how did the lunar crust form in the beginning? It is generally agreed that the Moon formed by a giant impact between the protoearth and a Mars-sized planetesimal. Due to the high energies involved in the lunar formation, the entire surface and probably the whole Moon was molten. This stage of the lunar evolution is called the lunar magma ocean, first suggested by Wood et al. (1970) and Smith et al. (1970). The detailed evolution of the magma ocean is still under debate. Probably not all of the Moon was molten, but only an outer layer of approximately 500 kilometers, as predicted by a seismic discontinuity detected at this depth during the Apollo missions. During cooling of the magma, minerals crystallized in regions where pressure, temperature and composition allowed their formation. According to their specific density, relative to the existing magma environment, they either sank down to the bottom of the magma ocean or ascended up. This model predicts a low density plagioclase-rich crust, and a mantle richer in the mafic minerals pyroxene and olivine. KREEP materials (Potassium, Rare Earth Elements, Phosphorus), exposed in basalts of the Procellarum basin are rich in incompatible elements and represent the latest crystallized part of the magma ocean.

The model offers a good explanation for the highly anorthostic lunar crust. Anorthosite is a rock, rich in anorthite, a type of plagioclase rich in calcium and aluminium. Anorthite has a lower specific density than pyroxene or olivine and thus floats on top of the magma ocean. It has a very light color which also explains the high albedo of the highlands (i.e. the percentage of light reflected back from the surface). Based on Clementine iron (FeO) maps (Lucey et al. 1998) and Lunar prospector thorium maps from the gamma-ray spectrometer (Lawrence et al. 1998), Jolliff et al. (2000) proposed division of the crust into three different crustal provinces: the Procellarum KREEP Terrane, rich in incompatible elements as indicated by high thorium levels measured with Lunar Prospector and located within the Oceanus Procellarum and the Mare Imbrium; the Feldspatic Highlands Terrane, representing ancient lunar crust built from flotation and crystallization of anorthosites in a lunar magma ocean; and finally, the South-Pole-Aitken Terrane, probably lower crust materials exposed by the large impact that formed the South-Pole Aitken basin and stripped away the upper crust.

Of special interest is the large South Pole Aitken basin SPA (Pieters et al. 1992, Spudis et al. 1994). With a diameter of 2100 to 2500 kilometer and a depth of 12 to 14 kilometer, it offers a window into the materials of the lower crust and it belongs to the farside highlands. Here large amounts of the upper crust were stripped away by an impact, but no large scale lava flooding occurred like in the nearside basins due to the thicker crustal strata on the lunar farside and maybe a lack of heat producing elements below the SPA basin. It is still not agreed on whether this large impact penetrated only the lower crust or even reached the mantle, but a crustal scenario is preferred by most at present (Pieters
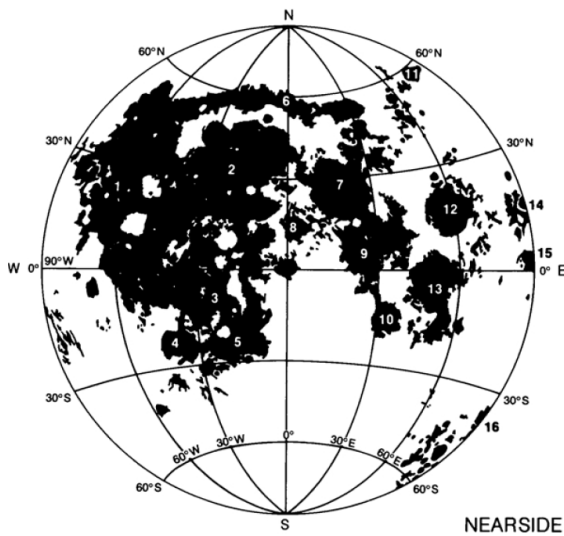
Figure 1.1: Lunar nearside mare: Oceanus Procellarum (1) and Mare Imbrium(2), Cognitum(3), Humorum(4), Nubium(5), Frigoris(6), Serenitatis(7), Vaporum(8), Tranquillitatis(9), Nectaris(10), Humboldtianum(11), Crisium(12), Fecunditatis(13) (Image: "Lunar Sourcebook" (Heiken et al. 1991, p.96))
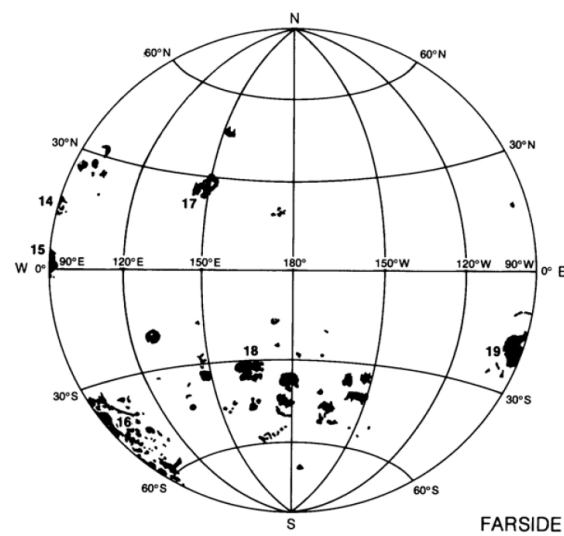
Figure 1.2: Lunar farside mare: Mare Marginis(14), Smythii(15), Australe(16), Moscoviense(17), Ingenii(18), Orientale(19)(Image: "Lunar Sourcebook" (Heiken et al. 1991, p.96))

et al. 1997, 2001). If even the large SPA impact did not penetrate through the crust it is unlikely that elsewhere, apart from mare basalts or cryptomare, for example in central crater peaks, material from the mantle would be exposed, even if the crust on the nearside of the moon is on average about 12 kilometer thinner than on the farside. It is more likely that those peaks represent different crustal materials than those from upper mantle. But mantle material is exposed in the mare and cryptomare areas.

1.2   Mare and Cryptomare

The dark mare of the Moon clearly stand out against the bright highlands. Here, remolten material from depth is exposed on the surface. Those basalts originate from partial melting of materials 200 to 400 kilometer below the surface (Heiken et al. 1991, p.103). Of the six Apollo missions five sampled mare material of different sites on the lunar nearside. From laboratory analysis of those samples we know that the mare are mainly basaltic in composition. They are richer in mafic minerals and opaques like ilmenite than the highlands, and thus they are darker. Lunar mare originate from distinct flooding events. Usually these events took place in former impact basins or craters were the crust was shattered and cracks offered an easy path for the lava to reach the surface and fill the topographic lows. This can be easily seen in the round shapes of many mare deposits which trace the topography of the impact basin they filled. From crater counts we know that the flooding events did not follow immediately onto the impact events, because the surrounding highlands are more heavily cratered than the mare deposits. There was a delay of many million years, between basin formation and basalt flooding. For example

the Imbrium basin impact occurred probably 3.85 billion years ago while the lavas of the basin sampled by Apollo 15 are about 600 million years younger (Heiken et al. 1991, p.102). For large mare, basalt flows from different source regions and different times, with varying compositions formed the final basalt deposit. Thus, for such mare areas the surface composition is not uniform. Different mare basalt flow units at the surface can be distinguished either from compositional variations, from crater counts, or from visible flood fronts observed at low sun angle. Mare deposits can be very thick at the center of filled basins. Head (1982) found a thickness of about 8 kilometer for the basalt layer in the center of the orientale basin, while Dehon and Waskom (1976) suggested an average thickness between 200 and 400 meter for the irregular outer basin areas. The thickness of mare deposits can be inferred remotely from buried craters, using theoretical assumptions about the ratio between crater radius and crater rim height. Furthermore, craters penetrating through the mare deposit and excavating underlying crustal material can give clues on the basalt thickness through theoretical assumptions of the ratio between crater diameter and crater depth. With remote sensing direct laser altimeter measurements of the depth can be used instead. With seismic measurements at a site, the depth of the basalt deposits can be measured directly.

Cryptomaria are mare deposits covered and thus not directly accessible, either by subsequent lava flooding events, or by bright crustal ejecta. The same mechanism which covered them on large scale with ejecta can also uncover them in smaller areas via small craters which penetrate through the covering layers and deposit dark ejecta of the underlying cryptomare onto the brighter surface. These craters are called dark halo impact craters and are an important tool for studying cryptomare, together with the detection of chemical and spectral anomalies (Antonenko et al. 1995). But the younger mare making up most of the accessible mare deposits, cover more of the lunar surface and are thus the one more intensively studied. Research on lunar mare concentrates on compositional analysis of the different lava bodies, on chronology of deposition, and on the conclusions we can draw from this about the source regions of the lava, about the mantle composition, as well as about the history and evolution of the lunar surface. Figure 1.1 and 1.2 shows the positions and names of the most prominent lunar mare deposits.

Regardless of which surface feature we observe, either highland or mare areas, what we see is mostly lunar regolith, and not pristine rock samples.

1.3   Regolith

Regolith is a material common to most atmosphereless bodies in the solar system. Even if the characteristics of planetary regolith vary according to its unique formation history and the location of its parent body in the solar system, the mechanisms of formation follow similar paths. Starting from a bedrock surface, with time this surface is exposed to meteorite impacts. These impacts are not evenly distributed in time. At the end of solar system formation impacts were much more frequent, due to the large amount of planetary building blocks still straying through the solar system. Those objects are on regular orbits within the solar system and are sometimes disturbed by the gravity of larger bodies (e.g.

Figure 1.3: Lunar surface image taken by Apollo 17 crew. The surface exhibits smooth slopes covered by regolith and isolated stones.

Jupiter) and sent on collisional courses, or simply captured by planets or moons. Each impact if big enough, fractures the bedrock, ejects material, melts rock and mineral fragments into glasses and produces a plume of vaporised material. Impacts come in many different sizes. From crater counts of the lunar surface we can retrieve the number of projectiles that will hit a unit surface within a unit time at the Moon's distance from the sun. These measurements are extrapolated towards different Sun distances and towards earlier ages were the bombardment of surfaces was stronger due to a larger source of impactors available immediately after solar system formation. Hence the Moon is an important messenger and archivist of the bombardment history of the solar system.

A second process that influences the formation of regolith is the constant bombardment by particles of the solar wind and from galactic cosmic rays, with the effect of the solar wind dominating. The strength of the solar wind decreases with increasing distance from the Sun. Hence this effect is less important in the outer solar system, but it influences the formation of regolith significantly on bodies like the Moon, Mercury, the martian moons Phobos and Deimos and the objects of the asteroid belt.

The process of regolith formation can be divided in 2 different phases: during phase one the regolith layer is still relatively thin. Large and small impacts can penetrate through the regolith and excavate new bedrock material. The thickness of the regolith layer increases. In phase two when the regolith thickness exceeds one meter only larger and rarer impacts are able to excavate new bedrock material. Smaller events only redistribute and fracture already existing regolith, a process called gardening. The lunar regolith has a thickness of 10 to 15 meters in highland areas and 4 to 5 meters in the younger mare areas (Heiken et al. 1991, p.286), which were for shorter times exposed to the destructive forces of meteoritic bombardment. Nevertheless, depending on the uniqueness of each

16

site the layer thickness varies, as it can be seen in the regolith thickness maps calculated by Shkuratov and Bondarenko (2001) from radar measurements at 70 cm, and iron and titanium contents for the lunar nearside. Particularly thin regolith layers are found in mare areas and on younger crater floors, from which older regolith bodies have been ejected. Under this upper regolith lies the megaregolith, an extended layer of large scale ejecta and cracked bedrock formed by large basin impacts. Simulations, were the cumulative effect from ejecta blankets of lunar basins and large craters are computed, give the possibility to access the large scale distribution of ejected material on the lunar surface (Petro and Pieters 2008)

For interpretation of the reflectance spectra taken in the near infrared a deep understanding of the formation process of the regolith is essential.

First, we have to validate the assumption that the regolith of a sampling site represents approximately the composition of the underlying bedrock if we want to use our results to draw conclusions about deeper strata or the formation of the Moon. How strong is the influence of vertical and lateral mixing? Demonstrative evidence is given by the sharp borders between the dark mare and bright highland areas. But this is only conclusive for the time after the large visible mare deposits formed. The visible mare formed after the first strong bombardment phase ended. Since then, the frequency of large impacts that eject material over wide distances decreased dramatically. The youngest basin on the moon, the Orientale basin, formed already over 3 billion years ago. The majority of the impacting projectiles is to small to distribute material over considerable distances. Nevertheless, all Apollo mare soil samples contain small amounts of highland material and vice versa (Korotev and Gillis 2001). The amount of foreign material in the regolith of a certain site can be estimated from calculations of cumulative impact ejecta (Korotev and Gillis 2001, Petro and Pieters 2007). Foreign material is mixed into the local regolith through large impacts. An example of long distant mixing in recent times are the rays of Tycho crater. Tycho is about 100 million years old and its rays extend up to 1500 kilometer from the impact site. On a smaller scale, a process called "gardening" regulates the evolution of regolith.

1.3.1 Gardening

Gardening is the process of constant overturning and mixing of regolith by numerous small impacts. On human timescales the regolith seems unchanging, impacts are rare and short time erosional forces like wind and rain are absent. On longer timescales the surface regolith is constantly mixed with new ejecta from meteoritic impacts. Thus with time much of the regolith is exposed at the near surface.

The solar wind which constantly strikes the lunar dayside alters the grains of the surface regolith. Some attributes of soil grains, like the amount of implanted solar wind ions, the number of high energy particle tracks and the amount of nanophase iron change in a regular way and are thus used as maturity indices to estimate the accumulated surface age of a regolith. Of course, a regolith mass does not represent a closed system of grains that stayed together from their formation till the time it is sampled. Rather, every regolith

sample is a mixture of grains, and each grain has a unique history. It is impossible to discover the history of each grain: thus we observe spectra from regolith samples which at least for a while shared the same history in a confined area of about 300 to 1000 meter within one SIR-1 footprint diameter. The light from the surface in the field of view of the instrument, the so called footprint, is bundled into an optical fiber and detected as an average point spectrum of the footprint. To take an equivalent sample for these remotely sensed reflectance spectrum into the laboratory, material would have to be racked together from the uppermost millimeter of lunar soil of an area corresponding to the SIR-1 instrument footprint. Due to the constant mixing of regolith down to a certain depth the upper layer is representative for the surface regolith of a site.

1.3.2   Space weathering

While a regolith grain resides directly on or close to the surface it is exposed to several effects of the space environment. The various effects are summarized in the term space weathering, caused by the combined influence of solar wind exposure and micrometeorite impacts on planetary soils. A sample of mineral grains freshly exposed on the lunar surface for the first time would undergo several changes. The energetic particles of the solar wind produce tracks within grains and sometimes become implanted within them, leading to an enrichment of solar wind atoms within the lunar regolith. The vertical concentration profile of these atoms has been measured within the drill cores returned by the Apollo program.

The other main agent of space weathering is the constant bombardment by micrometeorites. During an impact four things may happen depending on the size and energy of the impactor:

1. Material is ejected from the impact site.

2. Material is fractured and broken below and at the impact site.

3. Part of the target is evaporated and an impact plume forms. The projectile is usually completely evaporated at common lunar impact energies. This impact vapor partly escapes into space and partly recondensates on the surfaces of regolith grains. Due to fractionation during the condensation process small metallic iron particles form, which are observed within the rims of lunar regolith grains. It is referred to as small microscopic iron (SMFe) or nanophase iron (npFe). Due to the strong absorption of these iron particles the albedo of a soil decreases with increasing surface exposure. This absorption is wavelength dependent, and stronger at shorter wavelength leading to the development of a red slope within lunar reflectance spectra.

4. During impact the target material is heated. Regolith material melts and forms pure impact glasses, or mixtures of grains, partly molten grains and glasses welded together into agglutinates. Those agglutinates and glasses can make up over 60 percent of mature soils, which is a major problem for modeling reflectance spectra cause it is no well-ordered process, and an average agglutinate glass spectrum is difficult to define. At present a spectrum of agglutinates separated from a Luna 20
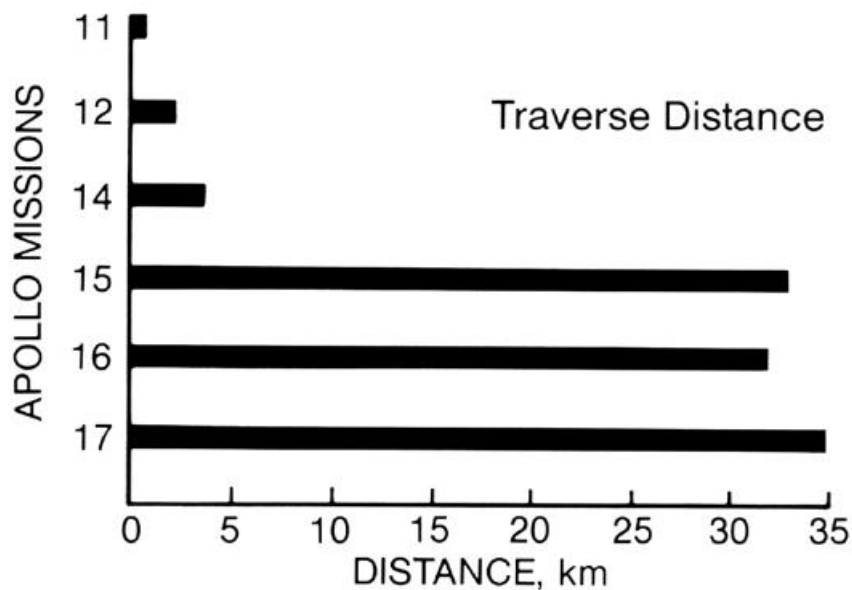
Figure 1.4: Covered distance for the six Apollo missions. The known size of the Apollo sampling areas and the measured spectra of Apollo soil samples (Figure 1.16), give an impression about the diversity of soil spectra already present in small surface areas.

soil is used to represent this component in the regolith reflectance model developed in this thesis.

So after regolith formation and alteration by surface exposure and constant gardening, each regolith grain becomes unique. There might be types which originated from the same bedrock and shared similar impact history and thus belong to the same ejecta blanket, but on a small scale, the lunar regolith is extremely complex. Nevertheless from space this complexity cannot be directly sampled. We perform an average of the regolith spectra of an area, and thus certain simplifications become inevitable. One of these simplifications is the assumptions that the reflectance spectrum of a given area can be modeled using a single compositions for the four major minerals (plagioclase, pyroxene, olivine and ilmenite) for the whole site and one average grain size. Samples from a certain area within one of our footprints, in reality would have varying compositions and grain sizes. This can be easily tested analyzing the compositional and grain size variation for Apollo samples originating from a restricted area. In Figure 1.4 the traverses for the six Apollo missions are shown and Figure 1.16 displays selected spectra of soils sampled by the Apollo teams, already showing variations for one single sampling site. Apollo 11,12 and 14 stayed within the size of an average SIR-1 footprint of one square kilometer, during extravehicular activity (EVA). Unfortunately only one real soil sample (10084) is available and analyzed for Apollo 11. The compositions of two Apollo 12 mare soils (Taylor et al. 2001) and four Apollo 14 highland soils (Taylor et al. 2003) show already variations of several percent in the amount of the major lunar minerals. Furthermore, even
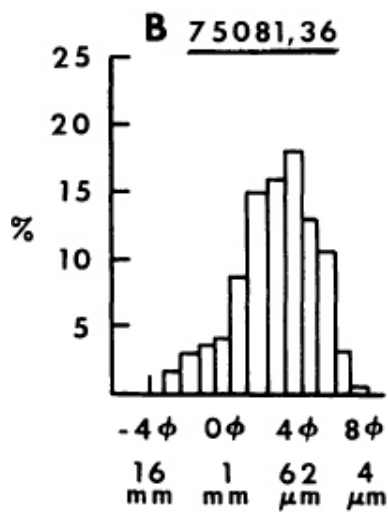
Figure 1.5: Apollo 17 grain size histogram. The mean graphical grain size of this sample with sizes smaller than 1 cm is 81.9 μm (Sample 75081,36) (McKay et al. 1974b).
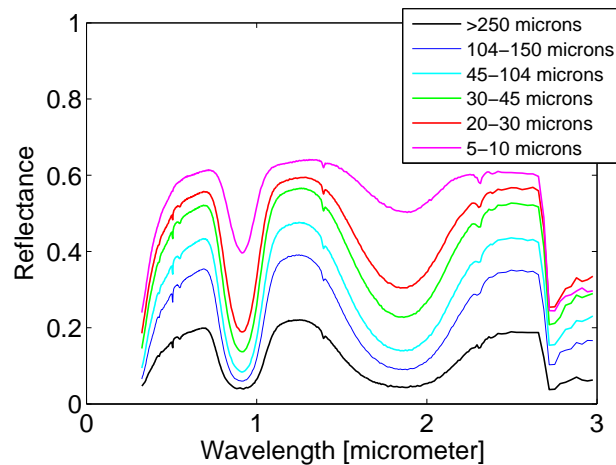
Figure 1.6: This image shows reflectance spectra of a hypersthene powder sieved to 6 different grain size intervals. With decreasing grain size, the overall intensity increases, while the absorption bands get weaker and narrower. The data is taken from the USGS spectral library (Clark et al. 2007), and was originally published by Clark et al. (1993).

if represented by an average grain size, not all regolith particles have the same size.

1.3.3   Grain size distribution

In reality the sizes of regolith particles in a sample can be described by a grain size distribution (McKay et al. (1974a), Carrier (1973), McKay et al. (1974b)). For example McKay et al. (1974b) measured the mean grain size for 42 Apollo 17 samples and derived mean grain sizes between 40 and 170 micrometer. A histogram of grain sizes of one Apollo 17 soil taken from McKay et al. (1974b) is shown in Figure 1.5.

During comminution of lunar bedrock large rocks are progressively crashed into smaller blocks and finally into grains. With time this leads to an increase in number density of small grains, till they not only become the dominant type but also represent the largest mass. Not only destructive processes are at work on the lunar surface: the formation of agglutinates is a constructive process welding small particles together leading towards a kind of equilibrium grain size distribution in mature soils. All Apollo landing sites were characterized by wide smooth plains covered by dusty regolith and sporadic cobbles. Image 1.3 from the Apollo 17 mission illustrates the most common lunar landscape. In the more heavily cratered highlands, around rims and within ejecta of younger craters we might find either rougher surfaces with larger stones or fresh surface uncovered by recent gravitational slumpings. The bulk of the lunar surface is older than 3 billion years and probably resembles the Apollo landing sites. The reflectance spectrum of a typical lunar surface is dominated by its fine grained soil cover. The term lunar soils refers to the fraction of lunar regolith with grain sizes smaller than 1 centimeter (1000 micrometer). From

measurements of Apollo soil samples we know the grain size distributions of typical lunar soils. An example for an Apollo 17 soil is shown in Figure 1.5. Prior to laboratory analysis the Apollo samples were often sieved to certain grain size intervals with a maximum and minimum grain size. The overall mineral composition of these grain size fractions can vary within those size separates as can be seen in the measurement of mare and highland soils by Taylor et al. (2001, 2003).

Laboratory measurements show that particle grain sizes have a major influence on reflectance spectra. Given the sample of one single mineral powder, sieved into different grain size intervals, the sample with the smallest grain size will exhibit the strongest reflectance, and the reflectance will continuously decrease with increasing grain size. Smaller grains have a larger surface volume ratio which makes them reflect more light than larger grains. Additionally, they dominate the soils in number and volume and thus have larger impact on the overall reflectance spectrum of a soil. This was confirmed by Pieters et al. (1993) showing that when reflectance spectra of several Apollo bulk soils were compared to reflectance spectra of the soils size separates, the finest fraction of grains smaller than 25 micrometer resemble most the spectrum of the bulk soil.

1.4   Lunar minerals and their spectra

Around 100 different minerals were identified within the Apollo and Luna samples from the Moon. Most of them, however, only in small amounts or within isolated samples. We will concentrate on the most abundant minerals, those which define the lunar reflectance spectra and are accessible through remote sensing. The main minerals on the Moon are the silicates plagioclase, pyroxene, and olivine. Another strong influence on the reflectance spectra comes from the oxide minerals, ilmenite and sometimes spinel which play an important role for the overall albedo of a surface site; these minerals are present in many varieties. The different mineral varieties and their significance for remote observations of the moon will be described below. As already mentioned, the brightness of the lunar highlands derives from their high plagioclase feldspar content.

1.4.1   Plagioclase and alkali feldspars

The mineral chemistry of the feldspar group varies between the endmembers albite, anorthite and potassium feldspars (K-feldspars). Figure 1.7 shows the composition triangle representing the feldspar endmembers. Feldspars of the solid solution series between albite and anorthite are called plagioclase. Arbitrary boundaries separate the minerals of this series according to their content of sodium and calcium (Table 1.1). Feldspars in composition between potassium feldspars and albite are called alkali feldspars.

The feldspar variety anorthite, is the main mineral in the common lunar highland rock type Anorthosite. This rock consists of plagioclase feldspars with commonly less than ten percent mafic components. In laboratory analysis of the composition of lunar samples the feldspar content is usually combined under the label "plagioclase" without subdividing into the actual endmembers of the feldspar triangle. This custom will be followed
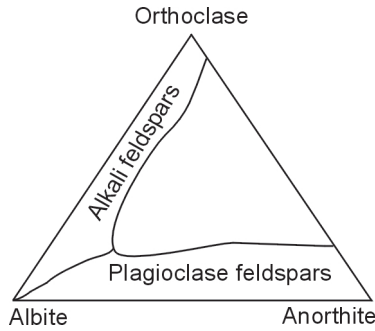
Figure 1.7: Triangle diagram for the endmembers of the plagioclase and the alkali feldspar solid solution series.
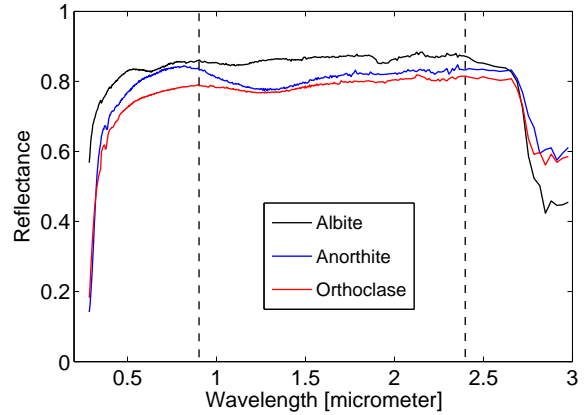
Figure 1.8: Reflectance spectra of the endmembers (albite, anorthite, orthoclase) of the plagioclase feldspars and alkali feldspars solid solution series. The data is taken from the USGS spectral library (Clark et al. 2007).

Table 1.1: Chemistry of plagioclase and alkali feldspars. The alkali feldspars (Microcline, Sanidine, Orthoclase) are polymorph, having the same chemistry but variant structures, caused by differing distributions of aluminium and silicon atoms due to different formation temperatures.

Plagioclase feldspars	Chemistry	Alkali feldspars	Chemistry
Albite	$NaAlSi_3O_8$		
Oligoclase	$Na(90-70\%)Ca(10-30\%)(Al,Si)AlSi_2O_8$	Microcline	$KAlSi_3O_8$
Andesine	$Na(70-50\%)Ca(30-50\%)(Al,Si)AlSi_2O_8$	Sanidine	$KAlSi_3O_8$
Labradorite	$Ca(50-70\%)Na(50-30\%)(Al,Si)AlSi_2O_8$	Orthoclase	$KAlSi_3O_8$
Bytownite	$Ca(70-90\%)Na(30-10\%)(Al,Si)AlSi_2O_8$	Anorthoclase	$(Na,K)AlSi_3O_8$
Anorthite	$CaAl_2Si_2O_8$		
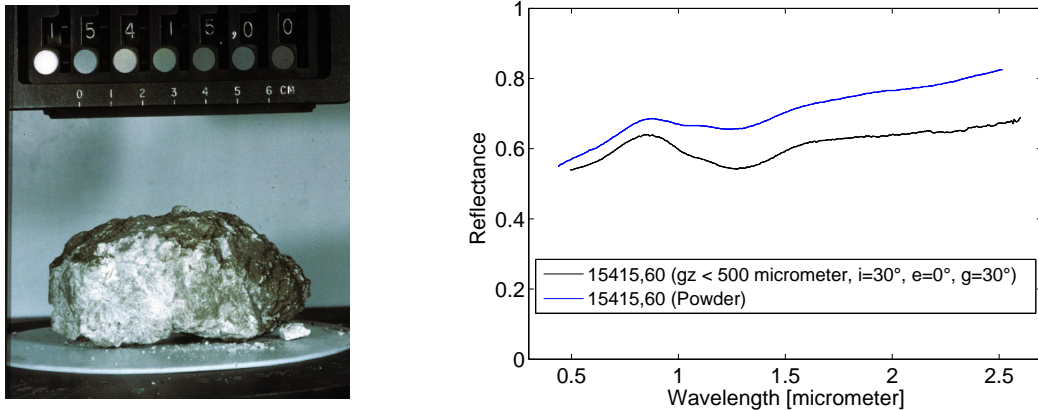
Figure 1.9: **Left panel:** Apollo 15 anorthosite rock number 15415 from Spur crater in the laboratory. The bright color is due to the high (99 %) plagioclase content of the rock. **Right panel:** Two reflectance spectra of the powdered rock subsample 15415,60. Both are dominated by an absorption band of Fe^{2+} within the plagioclase. The plagioclase of this sample are in average 96 % anorthite. Both spectra are darker then laboratory measured pure anorthite mineral reflectance spectra (compare to Figure 1.8).

within this work. From lunar samples we have good estimates on what percentage of feldspars we can expect in lunar regolith. Mineral compositions in the 20 to 90 micrometer soil fractions, of Apollo and Luna landing sites yield a percentage of plagioclase between 12 and 70 percent for highlands. Mare soils have usually a lower plagioclase content between 12 and 35 percent; nevertheless the unsampled farside highlands could have even higher feldspar amounts. Within the wavelength range of SIR-1, the laboratory reflectance curves (Figure 1.8) of the three feldspar endmembers exhibit no strong absorptions, between 0.9 and 2.4 micrometer. Even if the feldspar structure does not regularly incorporate absorbing cation species, such as Fe^{2+}, sometimes trace amounts of iron in plagioclase lead to a weak absorption band at 1.2 micrometer. Measurements of plagioclase separates from Apollo samples show this absorption (Pieters et al. 2008). Calcic pyroxenes (clinopyroxenes), also exhibit an absorption at this wavelength. For an unambiguous detection of the plagioclase absorption band near 1.2 micrometer it is necessary to verify that this absorption is not caused by pyroxene. Such a detection would only be reliable in the total absence of pyroxenes.

Another aspect that could affect the reflectance of feldspars at the lunar surface, is the exposure to high shock pressures as for almost all highland material. Johnson and Hörz (2003) have shown that high shock pressures between 17 and 55 Gigapascal reduce the albedo of anorthite and albite. As an example for an anorthosite rock, sample rock 15415 is shown in Figure 1.9. This rock consists almost entirely of plagioclase (99 %) with minor pyroxene contributions. Two reflectance spectra are available from the RELAB database for a powdered rock subsample 15415,60. Those spectra already show albedo differences of about 10 % (see Figure 1.9). For one spectrum (blue), the observing geometry and the particle size is not known, which might account for the differences in

Table 1.2: Chemistry of magnesium-iron and calcic pyroxenes. Diopside-augite-hedenbergite build a solid solution series of clinopyroxenes. Enstatite-hypersthene-ferrosilite build a solid solution series of orthopyroxenes. Hyperstene is often referred to as orthopyroxenes and expressed in proportions of the two endmembers enstatite and ferrosilite of the solid solution series

Clinopyroxene	Chemistry	Orthopyroxene	Chemistry
Diopside	$CaMg(SiO_3)_2$	Enstatite	$Mg_2(SiO_3)_2$
Hedenbergite	$CaFe(SiO_3)_2$	Hypersthene	$(Mg, Fe)_2(SiO_3)_2$
Augite	$(Ca, Mg, Fe)SiO_3$	Ferrosilite	$(Fe, Mg)_2(SiO_3)_2$
Pigeonite	$(Ca, Mg, Fe)(Mg, Fe)(SiO_3)_2$		
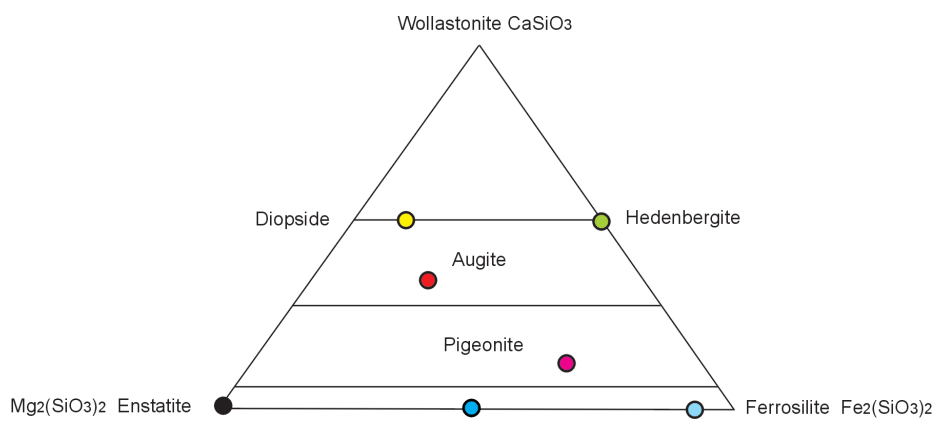
Figure 1.10: Pyroxene quadrilateral for magnesium-iron and calcic pyroxenes. The circles indicate the composition of pyroxene powder spectra displayed in Figure 1.11. Endmembers of the quadrilateral are enstatite, ferrosilite, hedenbergite and diopside. Wollastonite ($CaSiO_3$) is no pyroxene and there are no solid solutions with the calcium-rich diopside and hedenbergite. Nevertheless it is used for declaring pyroxene compositions as the "percentages" of wollastonite (Wo), enstatite (En) and ferrosilite (Fs) they contain.

reflectance. Highlighting again the importance of carefully, well documented laboratory measurements. Nevertheless both spectra are dominated by the Fe^{2+} plagioclase band.

1.4.2   Pyroxene

The minerals of the pyroxene group, are the second most abundant on the lunar surface. The pyroxene structure provides two crystallographic sites to incorporate different cations (eg. $Fe^{+2}, Mg^{+2}, Ca^{2+}$), the M1 and M2 site. The number of cations suitable for these crystallographic sites and the varying percentages of different cations within a crystal result in a large number of distinct pyroxenes. For lunar science the magnesium-iron (orthopyroxenes) and the calcic pyroxenes (clinopyroxenes) are of special interest. Here magnesium, iron and calcium cations populate the different crystal sites in variable amounts. According to crystal symmetry those pyroxenes are distinguished into clinopyroxenes with monoclinic symmetry, which contain calcium, and orthopyroxenes, with no
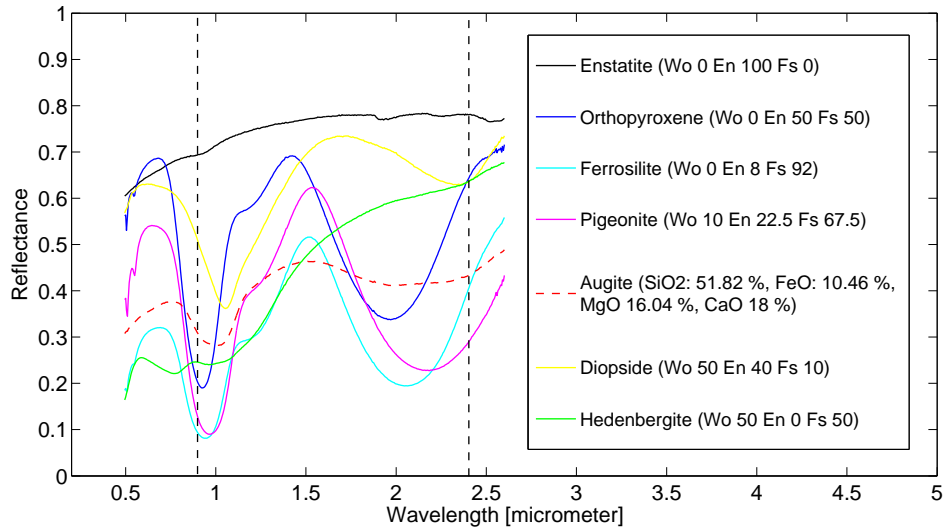
Figure 1.11: Representative pyroxene spectra of compositions indicated by circles in the pyroxene quadrilateral diagram for magnesium-iron and calcic pyroxenes (Figure 1.10). Except for the iron -free enstatite all spectra exhibit the characteristic pyroxene absorptions at 1 and 2 micrometer. All spectra, except the hedenbergite (grain size: 45-90 micrometer) spectrum are measured from mineral powders with grain sizes smaller than 45 micrometer. Spectra are taken from the RELAB database. For the augite spectrum the percentage of the major oxids gives the approximate position in the quadrilateral. The dashed black lines, indicate the SIR-1 wavelength range.

or only little calcium and orthorhombic symmetry. The chemical formulas of the pyroxenes of interest are given in Table 1.2. Pyroxene absorption bands are caused by the ion Fe^{2+} when located in the M1 and M2 site. Fe^{2+} prefers the M2 site where it produces the strong absorption bands at 1 (range: 0.9-1.03) and 2 (range: 1.8-2.3) micrometer. With increasing iron content in calcium-free pyroxenes the relative site population $n_{Fe^{2+}(M1)}/n_{Fe^{2+}(M2)}$ between the M1 and M2 site increases (Klima et al. 2007b) and thus the strength of the 1.2 micrometer absorption band which originates from Fe^{2+} in the M1 site. When calcium enters the pyroxene structure it can only be incorporated into the M2 site, due to its larger size. With the larger Ca^{2+} cation the M2 site becomes more distorted and absorptions at 1 and 2 micrometer caused by Fe^{2+} in these crystallographic sites shift to longer wavelength (lower energy). The shift of the absorption bands is clearly seen between the spectra of the calcium-free orthopyroxene and the calcium-rich augite in Figure 1.11. Adams (1974) reported the systematic change of the relative positions of the 1 and 2 micrometer with changing pyroxene composition, with orthopyroxenes having absorptions at shorter wavelength compared to clinopyroxenes at longer wavelength. Iron in the M1 site produces weak absorptions around 1.2 micrometer. In a series of studies of natural and synthetic pyroxenes (Klima et al. 2005, 2007a,b), almost all pyroxenes exhibited the absorption band at 1.2 micrometer. In Figure 1.11, were several pyroxene reflectance spectra are displayed, an inflection due to the 1.2 micrometer absorption is present for the ferrosilite, the pigeonite and the orthopyroxene spectra. Solid solution series exist be-
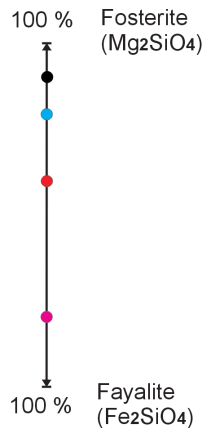
Figure 1.12: Solid solution series between fosterite and fayalite. The circles represent the compositions of the olivine reflectance spectra in Figure 1.13.
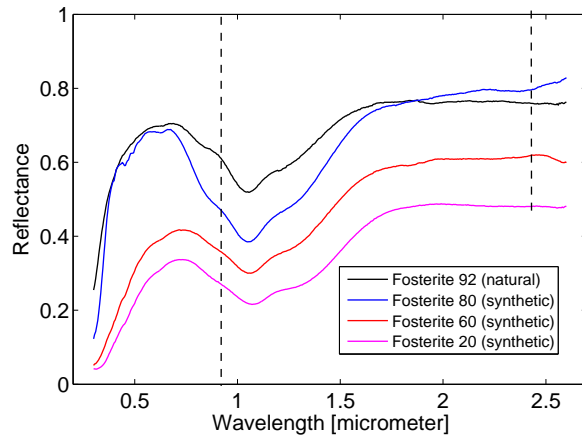
Figure 1.13: Reflectance spectra of three synthetic and one natural olivine powder of different fosterite content. All samples have grain sizes smaller than 45 micrometer. With increasing iron content (more fayalitic than fosteritic) the reflectance spectra become darker. In Figure 1.12 the positions of the four olivines within the olivine solid solution series are marked.

tween the orthopyroxenes enstatite and ferrosilite and the calcic clinopyroxenes diopside and hedenbergite. Lunar soils contain between 8 and 62 percent pyroxene in the 20 to 90 micrometer size fraction.

1.4.3 Olivine

The term olivine $(Fe, Mg)_2 SiO_4$ refers to a mineral from the solid solution series between the pure iron endmember fayalite $Fe_2 SiO_4$ and the pure magnesium endmember forsterite $Mg_2 SiO_4$ (Figure 1.12). Four reflectance spectra of synthetic and natural olivines of the olivine solid solution series are displayed in Figure 1.13. All spectra exhibit a broad absorption feature at 1 micrometer, which is composed of three different bands around 0.9, 1.05 and 1.25 micrometer. The olivine structure offers two sites for incorporation of cations (Fe^{2+} and Mg^{2+}), the M1 and M2 site. While magnesium is non-absorbing, iron in the M1 site causes the outer absorption bands at 0.9 and 1.25 micrometer, and iron in the M2 site causes the center absorption at 1.05 micrometer. King and Ridley (1987), Sunshine and Pieters (1998) investigated a suite of olivines between 2 % to 97 % fosterite composition and found a shift of all band centers to longer wavelength with increasing iron (more fayalitic) content. The slightly larger Fe^{2+} ions lead to an increase in oxygen-cation distance, resulting in a reduction of crystal field splitting and thus photons of lower energy (longer wavelength) are absorbed by Fe^{2+} ions, hence the absorption shifts to longer wavelength. Lunar soils contain between 2 and 18 percent olivine in the 20 to 90 micrometer size fraction.

26
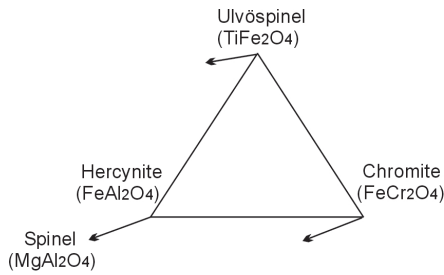
Figure 1.14: Simplified spinel triangle. Adding an additional dimension of increasing magnesium content, leads to the pure magnesian spinel itself ($MgAl_2O_4$).
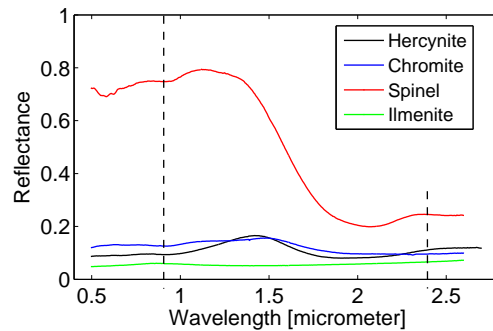
Figure 1.15: Laboratory reflectance spectra for ilmenite and three spinel endmembers. Lunar spinels are rich in titanium, iron and chromium and thus show a low albedo almost flat reflectance spectrum without prominent absorptions in the SIR-1 wavelength range (−−).

1.4.4   Ilmenite and Spinel

Ilmenite and minerals of the spinel group are respectively the first and second most abundant oxide minerals found in lunar samples. Ilmenite ($FeTiO_3$) has a solid solution series with geikelite ($MgTiO_3$) but the lunar ilmenites are usually iron-rich with only little magnesium and cluster around the ilmenite endmember of the series. The ilmenite content of lunar samples varies strongly and reaches up to 20 percent in some mare basalts. Since ilmenite is an opaque mineral, its main effect on lunar reflectance spectra is a general spectral darkening. In Figure 1.15 an ilmenite spectrum (green) is displayed together with different spinel spectra. Ilmenite would be an important resource in lunar exploration, because of its high titanium and iron content.

The Spinel mineral group has many members. the magnesium rich endmember spinel itself ($MgAl_2O_4$) is uncommon on the Moon. In lunar samples, phases between chromite (($Fe, Mg)Cr_2O_4$) and ulvospinel ($TiFe_2O_4$) are found and can be classified in a simplified triangle between the endmembers chromite, ulvospinel and hercynite ($FeAl_2O_4$) (Figure 1.14). In some lunar mare samples spinel contents of up to 10 percent where measured. Even if some iron-poor spinels can have high albedos, the lunar spinels are iron-rich and have on average an albedo lower than 0.1 in the near infrared. They cause, as ilmenite a general darkening of the spectra.

1.5   The shape of lunar spectra

Lunar spectra from different surface sites, although showing variation with composition and maturity exhibit common features. Figure 1.16 shows selected reflectance spectra of lunar samples collected during the Apollo 12, 14, 15, 16 and 17 missions. They exhibit the two prominent characteristics of lunar surface regolith reflectance spectra: an increasing slope from shorter to longer wavelength and absorption features around 1 and 2 micrometer due to mafic minerals present in the regolith. The mature Apollo 16 high-
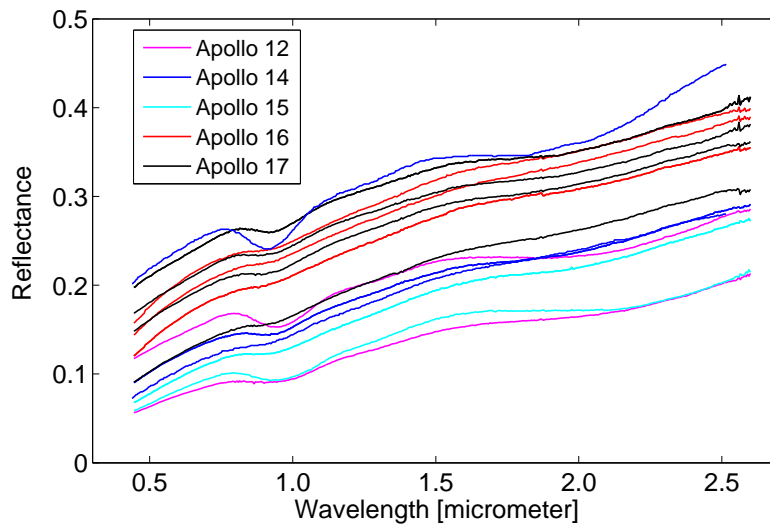
Figure 1.16: Selected reflectance spectra of lunar soils with grain sizes smaller 1mm, sampled at the Apollo 12, 14, 15, 16 and 17 landing sites. All soils exhibit a strong slope caused by small iron particles produces by space weathering, and weaker or stronger absorption features at 1 and 2 micrometer.

land soils have only very weak absorption features. They contain less mafic minerals than mare soils. Apollo 15 and 17, the two missions send to mare-highland boundaries, also sampled some highland soils.

A surface regolith contains mineral and rock fragments, agglutinates, volcanic and impact glasses, and fine grained metal. Reflected light is affected by the reflection and absorption characteristics of each component, the grain size distribution, the maturity (degree of space weathering), the porosity, and the microscopic and macroscopic surface roughness. This work is focused on deriving mineral compositions from lunar surface reflectance spectra.

1.6   Different modeling approaches

Several approaches can be employed to investigate the amount of the major minerals on the lunar surface from near-infrared reflectance spectra. A simple estimate for the composition is done by comparing the measured surface reflectance spectra with sample spectra measured in the laboratory. Recently, increased efforts have been made to model these spectra using basic theories. In planetary science extensive use is made of the Bidirectional Reflectance Theory by Hapke (1981), for surface reflectance spectra of planets, moons, asteroids and comets in the solar system. Another approach is the Modified Gaussian Model (MGM) by Sunshine et al. (1990, 1999), developed to model the strength, width and band centers of mineral absorption bands. In this thesis, Hapke's theory is applied.

1.6.1   Bidirectional Reflectance Theory

The bidirectional reflectance theory developed by Hapke (1981, 1993) provides an approximate solution to the radiative transfer equation. Several expressions for reflectance ratios are in use that can be obtained remotely for a planetary body. At the center of this theory stands the bidirectional reflectance of a surface which is given by

$$r_B = \frac{w}{4\pi} \frac{\mu_0}{\mu_0 + \mu}([1 + B(g)]P(g) + H(\mu_0)H(\mu) - 1) \tag{1.1}$$

The observation geometry is represented by μ_0, the cosine of the incident angle i, μ, the cosine of the emergence angle e and g the phase angle. The angular scattering pattern of particles in case of nonisotropic scattering is introduces by the phase function P(g), which equals 1 in case of isotropic scatterers. Unusual surface brightening at small phase angles due to shadow-hiding were less shadows from upper grains on lower grains are visible is described by the coherent backscatter function B(g). This effect is also called opposition effect. The Chandrasekhar H-function accounts for the multiple scattered part of the light. The ratio between light scattered, and light extinct in a single scattering event is described by the single scattering albedo w, which is close to 1 for nonabsorbing mineral particles. In the two datasets that are used in this work the radiance coefficient is used. The radiance coefficient is the bidirectional reflectance relative to a Lambert sphere which has a reflectance of $r_L = \mu_0/\pi$. Division of r_B by r_L leads to

$$r_c = \frac{w}{4} \frac{1}{\mu_0 + \mu}([1 + B(g)]P(g) + H(\mu_0)H(\mu) - 1) \tag{1.2}$$

which differs by a factor $\frac{\mu_0}{\pi}$ from the bidirectional reflectance. All reflectances in this work, from laboratory, spacecraft observations and modeling are given as radiance coefficient, even if simply referred to as reflectance. Using the radiance coefficient together with a least-square modeling routine and reasonable initial assumptions based on data from lunar samples, provides the mass percentages of the four major lunar minerals, an average particle sizes and a space weathering parameter for each modeled reflectance spectra. Because of the large number of free parameters, noise in the remotely measured reflectance spectra, and the limited wavelength range of the measurements nonunique solutions are observed. Future increases in wavelength range and measurement accuracy will lead to less nonunique solutions.

Another approach for analysis of reflectance spectra is to decompose the spectrum into a continuum and independent overlying absorption bands using the Modified Gaussian Model (MGM) developed by Sunshine et al. (1990, 1999).

1.6.2   Modified gaussian model

As the name already implies this model is a modification of an original gaussian model, where absorption bands are modeled using a gaussian distribution

$$G(x) = s \cdot exp\{\frac{-(x - m)^2}{2\sigma^2}\} \tag{1.3}$$

of the random variable x, which is in our case the wavelength (equivalent to energy). The center of the distribution is characterized by m, the width by σ and the strength by s. As Sunshine et al. (1990) remarked, this gaussian approach is sufficient to reproduce the broad 1 micrometer absorption band of olivine which is composed of three different bands with three gaussian distributions. Nevertheless modeling of the 1 and 2 micrometer pyroxene absorption bands requires two distributions for each band to successfully model the band shape for a pyroxene of a single composition. This conflicts with the fact that these bands are produced by only one single energy transition, thus making a physical interpretation of the simple gaussian model unreliable. Sunshine et al. (1990) suggest rather to treat the bond length than the energy as the statistical variable. Following their argumentation, in crystal field theory a relationship of $e \propto r^n$ between the absorption energy e, and the average bond length r is proposed. Thereupon they suggest a modified gaussian distribution

$$M(x) = s \cdot exp\{\frac{-(x^n - m^n)^2}{2\sigma^2}\} \qquad (1.4)$$

where the exponent n was determined as -1 from a best fit to the 0.9 micrometer absorption feature of one orthopyroxene. With this new distribution the 1 and 2 micrometer absorption bands of pyroxene can be modeled accurately. For clinopyroxenes a second weaker band at 1.2 micrometer is necessary to fully reproduce the whole spectrum. This band is frequently seen as an inflection of the 1 micrometer band for calcic and high-iron pyroxenes (see Figure 1.11). The advantage of this new approach is that no starting assumptions have to be made for the endmembers of a mixture, which makes this modeling routine especially suitable for deconvolution of mixtures with unknown endmembers as is usually the case for remotely sensed reflectance spectra. The MGM-model rather finds the kind of average mineral that dominates the reflectance of the absorbing species by defining the exact center position of each absorption band. In lunar spectra minerals with strong distinct absorption bands are pyroxene and olivine. To fully model a reflectance spectrum these modified gaussian distributions are superimposed on a continuum which is described by (Noble et al. 2006)

$$C(\lambda) = \frac{c_{-1}}{\lambda} + c_0 + c_1\lambda \qquad (1.5)$$

were λ is the wavelength and c_{-1}, c_0 and c_1 are variable constants to fit the measured spectrum. The continuum includes such diverse effects as the continuum reflectivity of each mineral species outside the absorption bands, the effect of space weathering products, and the effect of different average grain sizes. Because these parameters are removed before the analysis of the absorption bands, they cannot be derived from this modeling approach. The model is able to reproduce the general trend of pyroxene absorption band shifts between orthopyroxenes and clinopyroxenes, but the strength of the different absorption bands cannot directly be converted in mass percentages of a mixture. Noble et al. (2006) used the modified gaussian model for a suit of lunar soil spectra which was previously analyzed by the Lunar Soil Characterization Consortium (LSCC). In the range between 0.6 and 2.6 micrometer they modeled most of the reflectance spectra with 6 modified gaussion distribution and a continuum. All band strengths showed strong correlation with the overall pyroxene content. Furthermore, the MGM model was able to reproduce the relation of the positions of the two pyroxene bands, as described by Adams (1974), i.e. the

center positions of the pyroxene bands at 1 and 2 micrometer follow a linear trend when plotted against each other, with orthopyroxene absorptions present at shorter wavelength and clinopyroxene absorptions at longer wavelength. Since only two modified gaussian distributions were necessary to model each of the 1 and 2 micrometer absorptions in the complex reflectance spectrum of lunar samples suggests that two compositionally distinct pyroxenes can be sufficient to successfully model lunar reflectance spectra, even if this is a simplification of the compositional variety of lunar pyroxenes.

The types of lunar pyroxene classes were defined by Taylor et al. (2001) through an LSCC (Lunar Soil Characterization Consortium) analysis of lunar mare soils from Apollo 11, 12, 15 and 17 landing sites. Samples were analyzed on their content of several subsets of pyroxenes; orthopyroxenes, pigeonites, magnesium clinopyroxenes and iron clinopyroxenes. For mare soils, the majority of pyroxenes could be confined into the pigeonite and magnesium clinopyroxenes category. Highland soils also contain comparable amounts of orthopyroxenes, but for highland materials the overall pyroxene content is generally much lower. So even if the MGM-model cannot model the absolute abundances of the major minerals, the average grain size or space weathering degree, it is useful for a first approximation of the mafic endmembers of pyroxene and olivine. Furthermore the conclusion that two distinct pyroxenes are sufficient to model pyroxene composition of a site reduces the number of free parameters and thus strengthens the modeling results derived from bidirectional reflectance theory. Obvious candidates for those pyroxenes, would be the pigeonite and magnesian clinopyroxenes (augite) which account for most of the detected pyroxenes in the laboratory.

1.7   Contemporary missions to the Moon

In the mid-nineties lunar research received a new impetus from the Clementine and Lunar Prospector mission. Clementine reached the Moon in February 1994 and left lunar orbit three months later. During this time nearly the whole surface was imaged with several cameras and an extensive map of the whole Moon in different wavelengths was built from these data, including a topographic map. Furthermore, the Clementine Bistatic Radar Experiment found first evidence on possible water ice deposits at the permanently shadowed craters of the lunar poles. Data from the Clementine UV/VIS and NIR cameras are used throughout this thesis.

The Lunar Prospector mission arrived at the Moon four years later. It confirmed excess deposits of hydrogen at the lunar poles with its Neutron Spectrometer, which are thought to be water ice deposits mixed into the regolith. The Gamma Ray Spectrometer measured the abundance of thorium, potassium, uranium, iron, oxygen, silicon aluminium, calcium, magnesium and titanium at the lunar surface. Additionally, a gravity map of the Moon was produced using the Doppler Gravity Experiment and two instruments measured the magnetic field on the surface and around the Moon.

After the revival of lunar research in the 90's, many new lunar missions have already reached our satellite and several more are due to join in the near future.

SMART-1 (Small Missions for Advanced Research in Technology) a European mission for testing new technologies especially an ion thruster, took off in September 2003 and reached its final lunar orbit in February 2005. On board were several instruments; the AMIE camera (Advanced Moon micro-Imager Experiment) for imaging; D-CIXS, (Demonstration of a Compact X-ray Spectrometer), for detection of solar wind induced x-ray fluorescence to identify the amounts of magnesium, silicon and aluminium, as well as iron, calcium and titanium in case of stronger solar activity; XSM, a X-ray solar monitor to support D-CIXS; three other instruments (EPDP, SPEDE, KATE) monitored the propulsion system, the space probes environment and tested new communication frequencies. The SIR-group from the Max-Planck Institute for Solar System Research in which this work was conducted, constructed and built (in cooperation) the near infrared spectrometer SIR-1, which took reflectance spectra of the lunar surface between 0.93 and 2.4 micrometer. The analysis and modeling of those reflectance spectra are the topics of this thesis.

Space agencies based in Japan, China, and India have joined the space race, with several new missions targeting the Moon.

In September of 2007 Japan send its Kaguya mission to the Moon. Among the instruments on board, the spacecraft carried a Terrain Camera (TC), a Spectral profiler (SP), a Multi-band imager (MI), a Gamma Ray Spectrometer (GRS) and a X-Ray fluorescence spectrometer (XRS). Instruments targeted to the study of the minerals and elements on the lunar surface.

Just one month later, in October 2007, the Chinese Chang'e 1 mission was launched. Since then a Stereo Camera, an Imaging Spectrometer and a Gamma and X-Ray Spectrometer have investigated the lunar surface.

In October 2008 the first Indian Moon mission was launched. The SIR-group at the Max-Planck Institute for Solar System Research contributed with an upgraded and improved instrument SIR-2 (Spectrometer InfraRed 2) to map the lunar surface mineralogy from a lower orbit. Along with SIR-2, the Hyper Spectral Imager (HySI), the X-ray fluorescence spectrometer (CIXS), High Energy X-ray/gamma ray spectrometer (HEX) and the Moon Mineralogy Mapper (M^3) will address questions concerning the elements and minerals of the lunar surface.

Even if the Moon appears to be one of the most scientifically studied places in the solar system nowadays, we are far from reaching a routine in lunar science. A large amount of data is currently assembled, but reliable tools for analysis are still under development. The regolith reflectance model developed and tested in this work aims to become one of these new tools.

2 Comparison and combination of SIR-1 spectra and Clementine UVVIS and NIR camera data

When the Apollo era was over it became quiet around the Moon. For 14 years no man-made spacecraft disturbed the silence in lunar orbit while many other planets in the solar system were visited by messengers of human civilization. In the 1990's Hiten, Clementine and Lunar Prospector returned to the Moon, and interest in lunar science was renewed. The new millennium saw SMART-1, KAGUJA, Chang'e and Chandrayaan-1 make their way to the Moon and the future years will see an increasing amount of planned and hopefully realized lunar missions.

In this chapter, methods for comparing and combining SIR-1 and Clementine UVVIS/NIR

Table 2.1: Characteristics of SIR-1 spectrometer aboard SMART-1 and Clementine UVVIS and NIR cameras.

Instrument	Characteristics
SIR-1	**Type:** Point spectrometer **Wavelength range:** 256 pixel between 0.9-2.4 μm **Spectral sampling:** 6 nm **Spatial resolution:** 300 - 3000 m **Coverage:** 18 % **Access to data:** SIR team
Clementine UVVIS	**Type:** Imaging spectrometer camera with 5 photometric filters **Filter wavelength:** 0.415, 0.75, 0.9, 0.95, 1.0 μm **Spatial resolution:** 100 m **Coverage:** 99 % **Access to data:** http://pds-imaging.jpl.nasa.gov... /Admin/resources/cd_clementine.html#clmUVVIS
Clementine NIR	**Type:** Imaging spectrometer camera with 6 photometric filters **Filter wavelength:** 1.1, 1.25, 1.5, 2.0, 2.6, 2.78 μm **Spatial resolution:** 100 m **Coverage:** 99 % **Access to data:** ftp://pdsimage2.wr.usgs.gov... /cdroms/clementine/Clem_NIR_V0.1

datasets are introduced to exploit the strengths of both missions. The different steps and the sequence of analysis are shown in Figure 2.1. Details for the three instruments are summarized in Table 2.1. The SIR-1 point spectrometer took about 28 million infrared reflectance spectra during its two year mission. Light from 0.9 to 2.4 micrometer was dispersed onto a 256-pixel detector resulting in a spectral sampling of 6 nm per pixel. The SIR-1 field of view of 1.11 milliradian leads to a spacecraft-altitude-dependent footprint on the ground. The Clementine UVVIS/NIR pixel within a SIR-1 footprint are averaged for comparison of images and point spectra. The altitude dependent number of Clementine image pixels within one SIR-1 footprint are shown in Figure 2.2. For mean lower altitudes of 561 km reflectances of 122 UVVIS/NIR pixels are averaged. At upper mean altitudes of 2083 km , 1680 pixels are averaged. The lowest altitude reached for good observing conditions was 200 km and 16 UVVIS/NIR pixels were averaged there. Clementine UVVIS and NIR camera mosaics are processed to a spatial resolution of 100m/Pixel. However, this is not always the real physical resolution, but rather the pixel size of the two basemap mosaics (maps of the moon composed from the UVVIS and NIR camera images). UVVIS, the camera for ultraviolet, visible and near infrared images, took pictures at 0.415, 0.75, 0.9, 0.95 and 1.0 micrometer. The NIR camera took images at 1.1, 1.25, 1.5, 2.0, 2.6 and 2.78 micrometer. Using the Clementine image mosaics we can establish the geologic context for SIR-1 point spectra. Furthermore we can incorporate methods developed for UVVIS/NIR images, in which ratios between images at different wavelength are linked to properties like maturity (age) of the surface (Lucey et al. 2000b) or the FeO and TiO_2 content (Lucey et al. 1998, 2000a) of the sample region.

Due to the different character of the two missions, we need to find a way to combine the point-spectrometer data of SIR-1 with the images of the UVVIS and NIR cameras. The SIR-1 footprint had a circular shape when the instrument was in nadir-pointing mode (emergence angle of zero degree). This shape becomes more elliptic with increasing emergence angle. By averaging the reflectances from Clementine UVVIS/NIR pixels within a SIR-1 footprint ellipse the two datasets can be compared. At first, relative spectra of SIR-1 and Clementine UVVIS/NIR were compared. Due to changes of the spectral sensitivity of SIR-1 instrument during the mission, absolute calibrated spectra are not available for SIR-1. A temperature-dependent variation of the spectral sensitivity curve was observed. The spectral sensitivity curve provides the important connection between the digitalized signal measured by the detector and real physical quantities as reflected energy. During calibration of the instrument on Earth a spectral sensitivity curve was measured using a standard light source, an integrating sphere with well known energy spectrum. This laboratory absolute spectral sensitivity curve and a mean spectral sensitivity curve derived from cross-calibration between Clementine data and several SIR-1 point spectra taken at different orbits during early mission are displayed in Figure 2.3.

Obviously there are alterations, causing the laboratory spectral sensitivity curve to be not fully valid anymore for the instrument in orbit around the Moon. When using the laboratory curve, wavy structures appear in the absolute spectra. These structures also appear within relative spectra if sample and reference spectrum are chosen too far away from each other. The variation seems to be correlated to the temperature of the instrument. The temperatures of the different instrument parts depend on the spacecraft position and
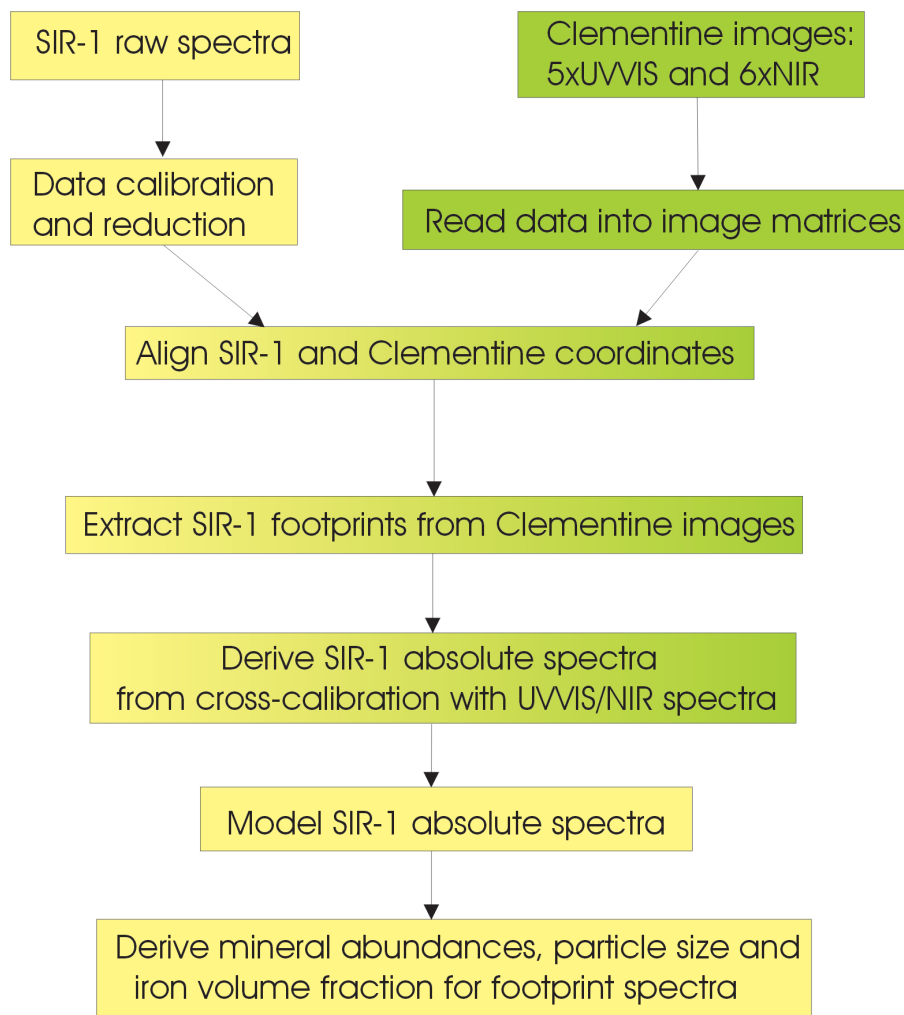
Figure 2.1: This flowchart illustrates the processes of data extraction and modeling.

orientation. The thermal load (input) changes while the spacecraft moves along an orbit. In addition to this, the spacecraft orientation changed randomly during manoeuvres for pointing observations of special lunar features and calibration measurements of standard stars. To overcome the spectral sensitivity problem we have two options. Either we work with relative spectra, where the sample and the reference area are close enough together within one orbit so that no change in spectral sensitivity occurs, or we use Clementine images to cross-calibrate the SIR-1 spectra. Both options are used.

2.1 Relative spectra

A relative spectrum is the ratio of two spectra. One spectrum is taken from a lunar sample area and one from a nearby reference area. By dividing two spectra taken with the same instrument, instrument effects that affect both spectra the same way, as for example the spectral sensitivity of the instrument, cancel out. This method is also used for Earth-based telescope observations to remove the disturbances of Earth's atmosphere. For we are in-
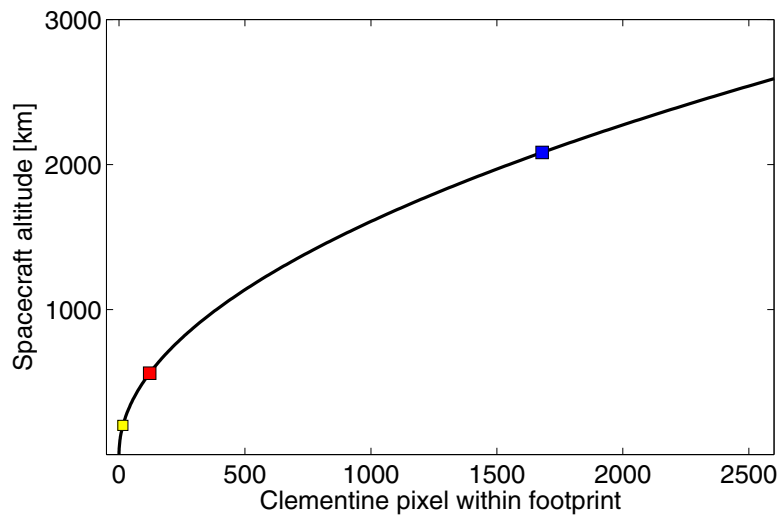
Figure 2.2: This graph gives the number of Clementine pixels within one SIR-1 footprint, depending on spacecraft altitude. For reasonable observing conditions (incident and phase angles smaller than 70 degree) the blue square represents the mean upper value of observation, the red square represents the mean lower value and the yellow square the minimum footprint size for these measurements, which was reached in orbit 2682 during late mission stage over South Pole Aitken basin.
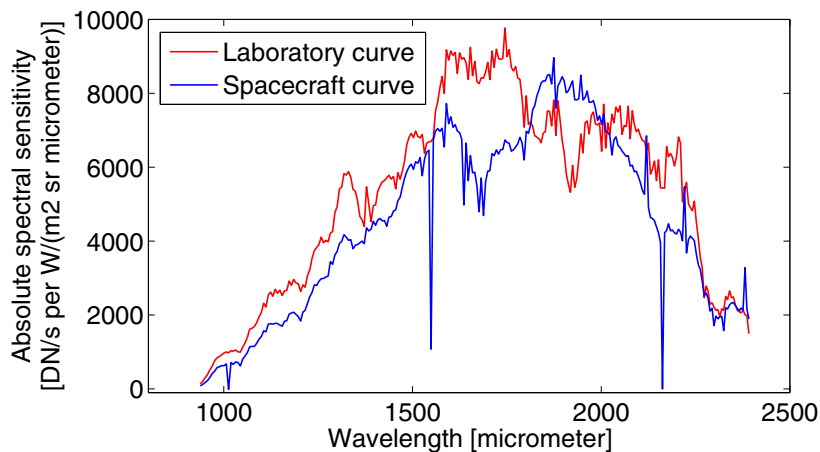
Figure 2.3: Original spectral sensitivity curve of SIR-1 measured during ground calibration (red line) together with a mean spectral sensitivity curve calculated from cross-calibration with Clementine camera mosaics.

terested in the mineral absorption features of the sample spectrum, the reference spectrum should ideally have no absorption features at all.

Because of the high average age of the lunar surface and the obliterating effect of space weathering on spectral features of regolith spectra, as well due to the general weakness of mineral features in spectra of the lunar highlands, a reliable reference site can be found nearby most sample areas. Highlands are highly anorthositic with only small amounts of mafic minerals, hence exhibit a high albedo but only weak to no absorption features. By using similar or the same reference area for different sample spectra the relative spectra become comparable because both were derived relative to the same reference. In this way we can generate a consistent set of data with relative spectra all over the Moon. At mare areas, proper references are less easily found. These mafic and ultramafic basalts exhibit usually stronger absorptions due to a higher content of iron bearing minerals with strong bands. Those absorptions are weakened but still visible within even very mature (old) soils.

Absorption features in the reference spectrum can be easily detected as apparent emissions in the relative spectrum. This fact provides us with an easy tool to exclude poor reference spectra. To demonstrate the effect of the reference spectrum on the relative spectrum, laboratory reflectance spectra of three lunar minerals are displayed in Figure 2.4 as absolute and relative spectra. There it can be seen that absorptions in the sample spectrum are well preserved in the relative spectrum and that absorptions in the reference spectrum result in apparent emissions in the relative spectrum.

Usually the reference spectrum is taken as the median of 50 spectra nearby the sample area. This reference spectrum should represent the featureless background of the surface feature of interest. For example, when observing a certain crater the reference should lie well outside the crater's ejecta blanket. By taking the median of 50 spectra as reference, outliers from small fresh craters in the reference area do not severely affect the reference spectrum, because the median is less influenced by extreme values than the mean. Nevertheless, if there are to many fresh surface features, a better reference has to be found or apparent emissions will be recognized in the relative spectra. But today only seldom fresh material is exposed at the lunar surface. Since the formation of the solar system the rate of impactors decreased dramatically after the first violent stage of planetary accretion. Now almost the whole surface is covered by a thick layer of mature regolith, well suited as reference for the rare, less mature surface features.

Through the comparison of the relative spectra of SIR-1 and Clementine UVVIS/NIR the consistency of both datasets has been proven. The relative spectra, if computed for both instruments from the same sample and reference area, agree for most areas. Nevertheless, if the observing conditions of the two instruments were too different, large scale surface roughness and shadows influence the spectra and cause discrepancies.

Observing conditions are described by three angles shown in Figure 2.5. The incident angle (i) of sunlight illuminating the surface, the emergence angle (e) of sunlight reflected towards the spacecraft and the phase angle (g) between sun and spacecraft direction.
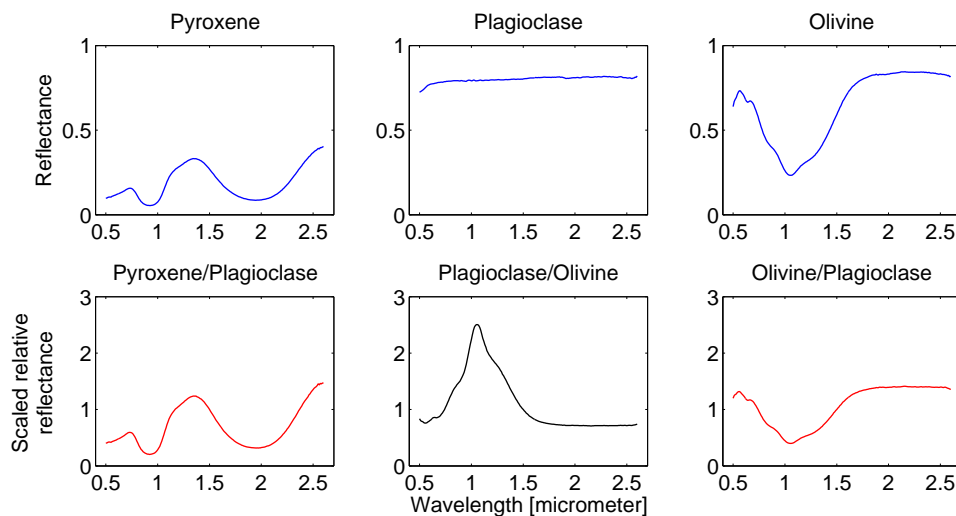
Figure 2.4: This image illustrates the influence of reference spectra onto relative spectra. The upper images show laboratory spectra of three common lunar minerals (plagioclase, pyroxene, olivine). If the featureless plagioclase spectrum is used as reference, absorption bands of the sample spectra (pyroxene and olivine) are clearly visible in the relative spectra (red curves). Choosing olivine as a reference and plagioclase as a sample spectrum leads to an emission-like feature in the relative spectrum (black curve).

Clementine observed mostly near local noon from nadir (e=0) in an orbit deviating +/- 30 degrees from sun synchronous. Observations of SIR-1 aboard SMART-1 were taken with two different orbit configurations. In noon/midnight modus and in dawn/dusk modus. During dawn/dusk modus SIR-1 observed at large phase angles. During the calibration of the data the effect of the differing observation geometries is accounted for and removed. All observations are first reduced to zero incident, emergence and phase angle and then translated to a standard geometry of 30 degree incident angle, zero degree emergence angle and 30 degree phase angle. Tests show, that for incident angles larger than 65 degree for SIR-1 spectra the cross calibration of SIR-1 and Clementine UVVIS/NIR data becomes unreliable due to shadows and deviant incident angles at crater walls. The effect of steep slopes at crater walls and central peaks on the assumed and real observing geometry is illustrated in Figure 2.6.

Light collected for one footprint originates from surface patches of variable local surface normal. Thus no common incident, emergence and phase angle can be defined. Usually the local surface is assumed to be that of a perfect sphere. This assumption is wrong for footprints at crater walls and peaks. The phase angle stays the same, but incident and emergence angle change. Inserting wrong angle values into the phase function we are not able to reduce the observations to standard geometry ($i = 30°, e = 0°, g = 30°$). Of course the same problem occurs within the Clementine calibration. So with both calibrations being incorrect in regions of large scale surface roughness we cannot expect full consistency
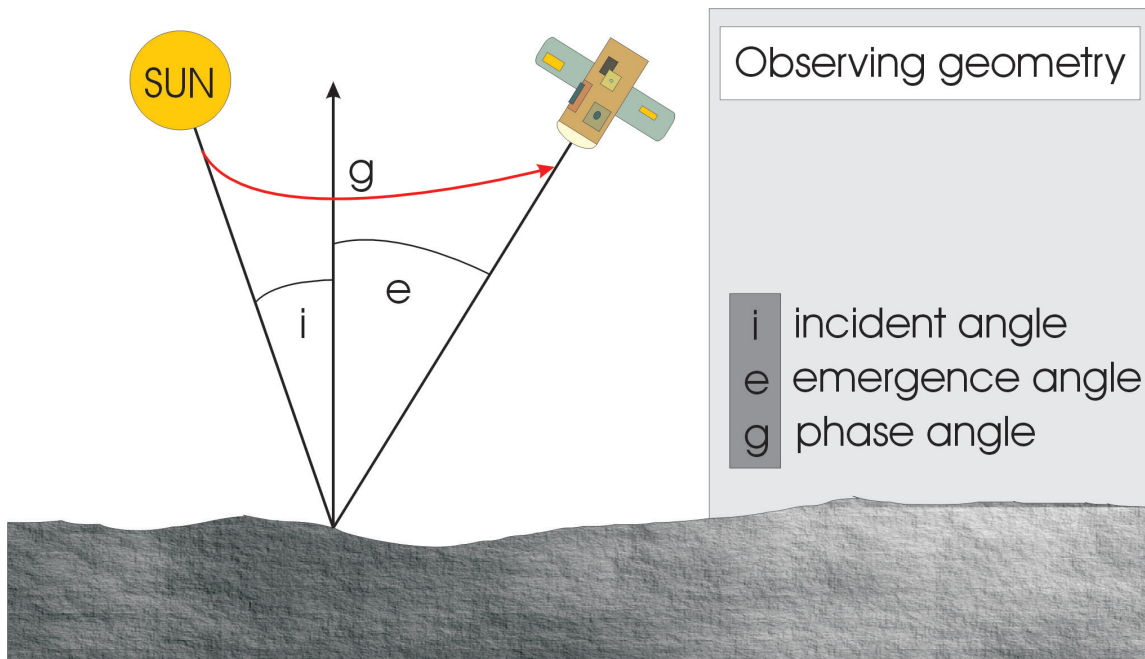
Figure 2.5: Observing geometry as defined by incident (i),emergence (e) and phase angle (g) for a bidirectional reflectance measurement of the lunar surface. The incident angle depends on the lunar latitude of the observed area and on the distance from the lunar terminator (day/night line).
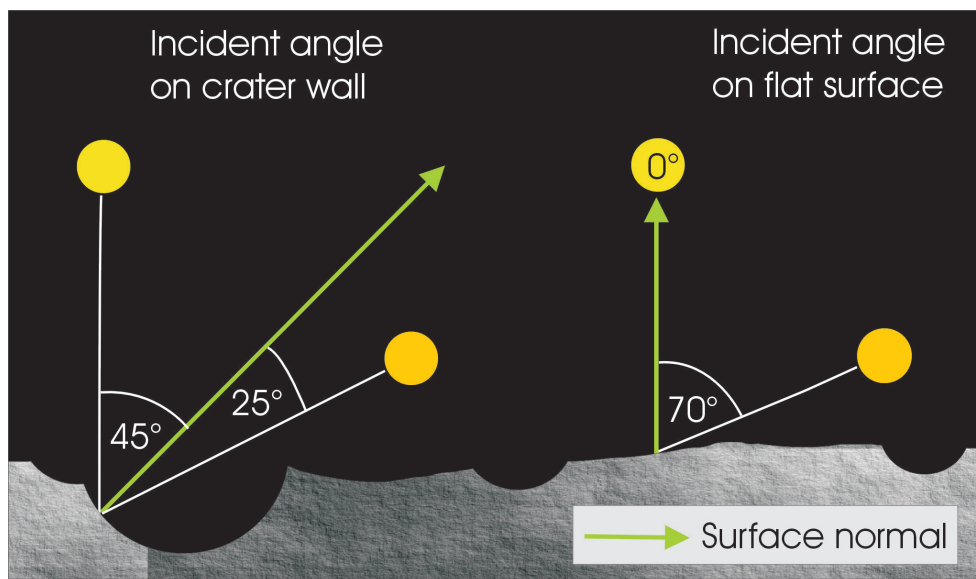
Figure 2.6: This figure illustrates the effect of steep slopes on the observing geometry. Crater walls and central peaks receive more sunlight when the sun is lower over the horizon and not in shadow. For the reduction of raw data to standard observing geometry, an incident angle relative to the local surface normal is assumed. The incident angle varies with lunar latitude and lunar phase. The local area is simplified as flat. This is true for most of the surface but becomes wrong at step crater walls and peaks. By using a simplified incident angle and neglecting the large scale surface topology, we introduce an additional error source to the data.

for both datasets at these locations. Nevertheless, this would mainly influence the overall albedo of the sample spectrum. Thus the relative spectra will be offset but still exhibiting the same shape.

2.2   Absolute spectra

If an absolute calibration is available, absolute spectra have more significance for the scientific analysis. An absolute spectrum directly gives the reflectance (or albedo) of a surface at several wavelength. To obtain absolute reflectances we need to convert the digital units usually measured with instrument detectors to real physical units of energy. For satellite missions either ground calibrations with a source of known intensity or calibrations with standard stars are applied. The availability of lunar samples gives the additional option of calibrating the remote observations of the Moon with laboratory measurements of samples from known locations on the Moon.

For UVVIS and NIR data an absolute calibration is available based on Apollo sample 62231, a mature soil assumed to be representative for the Apollo 16 site. In "The Moon as spectral calibration standard" by C.Pieters the method is described [1]. SIR-1 data has not yet been absolutely calibrated. The laboratory spectral sensitivity of the instrument measured during calibration of the instrument on ground changed during the mission. Part of the changes are related to the varying instrument temperatures caused by a change of thermal load in the lunar orbit. We can correct for this and derive indirect absolute spectra for SIR-1 data, when we cross-calibrate the SIR-1 spectra with Clementine UVVIS/NIR absolute calibrated images.

Cross-calibration is time consuming and not successful for all SIR-1 observations. Most interesting are spectra of relatively fresh surfaces where strong absorptions can be found. This happens at young fresh craters, at steeper slopes of crater rims, rills or central peaks, where avalanches might have uncovered surfaces less affected by space weathering. Spectra from such regions promise most reliable modeling results, for absorptions are still strong and less altered by the various processes of space weathering. A cross-calibration is valid only for a certain SIR-1 orbit section were the changes in the instrument are negligible.

This cross-calibration is done via matching a median of 50 SIR-1 reference spectra and a median of 50 corresponding Clementine UVVIS/NIR spectra to find the cross-calibration curve between both datasets. The Clementine UVVIS/NIR spectra are extracted from the 11 Clementine UVVIS and NIR image maps. Image pixels inside the SIR-1 reference footprints are extracted and averaged. Eleven averaged values constitute one Clementine UVVIS/NIR spectrum at the eleven Clementine UVVIS/NIR wavelengths. The absolute calibration for the UVVIS and NIR cameras is assumed to be correct for the 5 UVVIS images and the first 4 NIR images. The NIR images at 2600 and 2780 nanometer were not calibrated with the Apollo 16 standard and are thus excluded from cross-calibration.

---

[1]http://www.planetary.brown.edu/pds/AP62231.html

At these wavelength also a stronger thermal contribution from the lunar surface is to be expected (see Section 2.3). The Clementine reference spectrum is interpolated for the 256 SIR-1 wavelengths and a cross-calibration between the median Clementine and the median SIR-1 reference spectrum is calculated. This cross-calibration curve is used to transform the SIR-1 high-resolution digital number spectra to absolute calibrated spectra. How do we motivate this interpolation?

Mature lunar soils as present nearly everywhere on the lunar surface exhibit only weak to none absorption features. These spectra are overdetermined by the 256 pixel of SIR-1. In Figure 2.7, laboratory reflectance measurements of 17 soils from the Apollo 16 landing site and 25 soils from the Apollo 17 landing site as well as a mean soil spectrum for each site are displayed. This is the laboratory analogue to the derivation of a reference spectrum on the Moon. All spectra show a strong red slope but little absorption features. Using the median of 50 consecutive spectra to produce a reference spectrum additionally degrades peculiarities of individual spectra. So despite a very weak dip at 1 micrometer, which is present in nearly all lunar spectra, these spectra can be described by a continuum curve and can be represented by the 8 points of Clementine reflectance spectra between 715 and 2000 nanometer. In Figure 2.8, an example for the interpolation between the Clementine measurements is shown.

Relative spectra of SIR-1 and Clementine match if no strong differences in illumination conditions are present. Thus we can infer that the absolute spectra also match. In cases of deviance, those spectra are excluded from further analysis. A cross-calibration curve to adapt SIR-1 256-pixel spectra to Clementine UVVIS/NIR is generated. In this way we gain information about the absolute reflectance, but still keep the advantages of the high resolution of SIR-1 in more active regions where Clementine UVVIS/NIR has not the resolution to sample the complex shape of absorption features in detail, but SIR-1 has. The artificial spectral sensitivity curve is a replacement for the absolute spectral sensitivity curve measured in the laboratory for the SIR-1 instrument. The SIR-1 instrument sensitivity changed with temperature, which lead to wavy structures in relative spectra when reference and sample spectrum were too far apart, and in absolute spectra, when the laboratory spectral sensitivity curve is used for calibration. To avoid this effect, sample spectra and reference spectra are always taken from the same orbit, within a certain range, usually not more than 1000 spectra apart from each other. In this region illumination conditions, and thus heat input change only very little and the temperature effect does not affect the relative spectra and the absolute cross calibration through UVVIS/NIR highland spectra.

2.3   Lunar thermal radiation

Planetary surfaces start to emit thermal radiation in the near infrared according to their surface temperature. The mean temperature of the lunar surface is 380 K (107°C) for the dayside and 120 K (-153°C) for the nightside. The maximum temperature measured on the Moon was 396 K (123°C). During the Clementine mission the Long-Wavelength Infrared (LWIR) camera took images in a passband centered at 8.75 micrometer. These measurements can be converted to brightness temperature. This is the temperature a gray
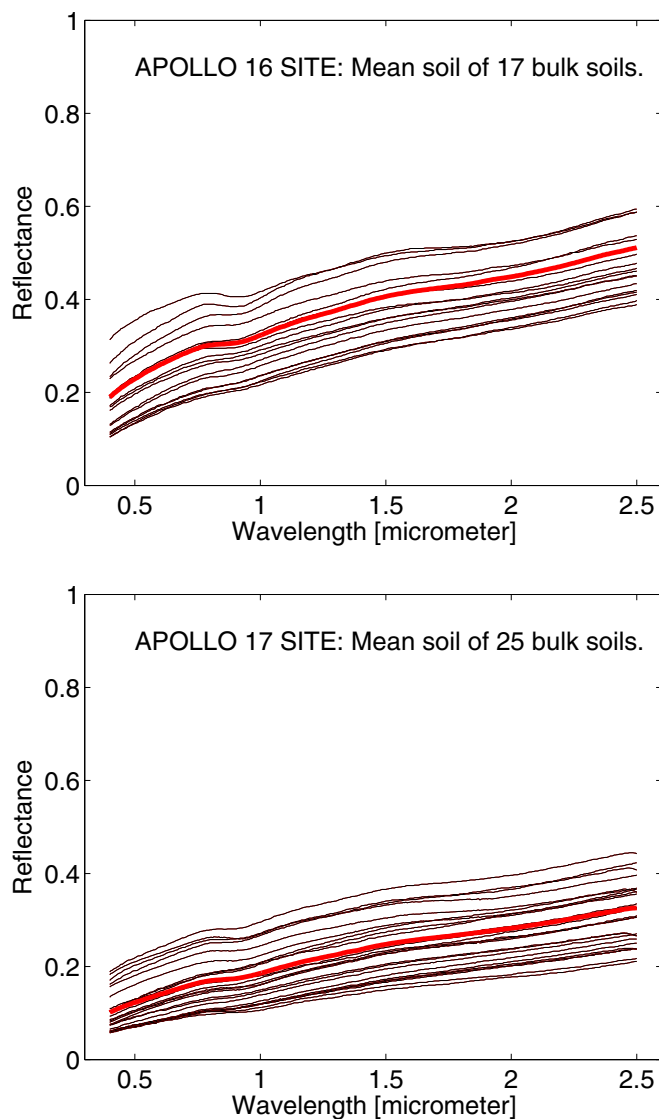
Figure 2.7: Soil reflectance spectra of 17 soils from Apollo 16 site and 25 soils from Apollo 17 site. These are bulk soils sieved to particle sizes smaller than 1 mm. The red line represents the mean of the displayed soils. Those spectra are representative of lunar surface material with strong red slopes and very weak absorptions.
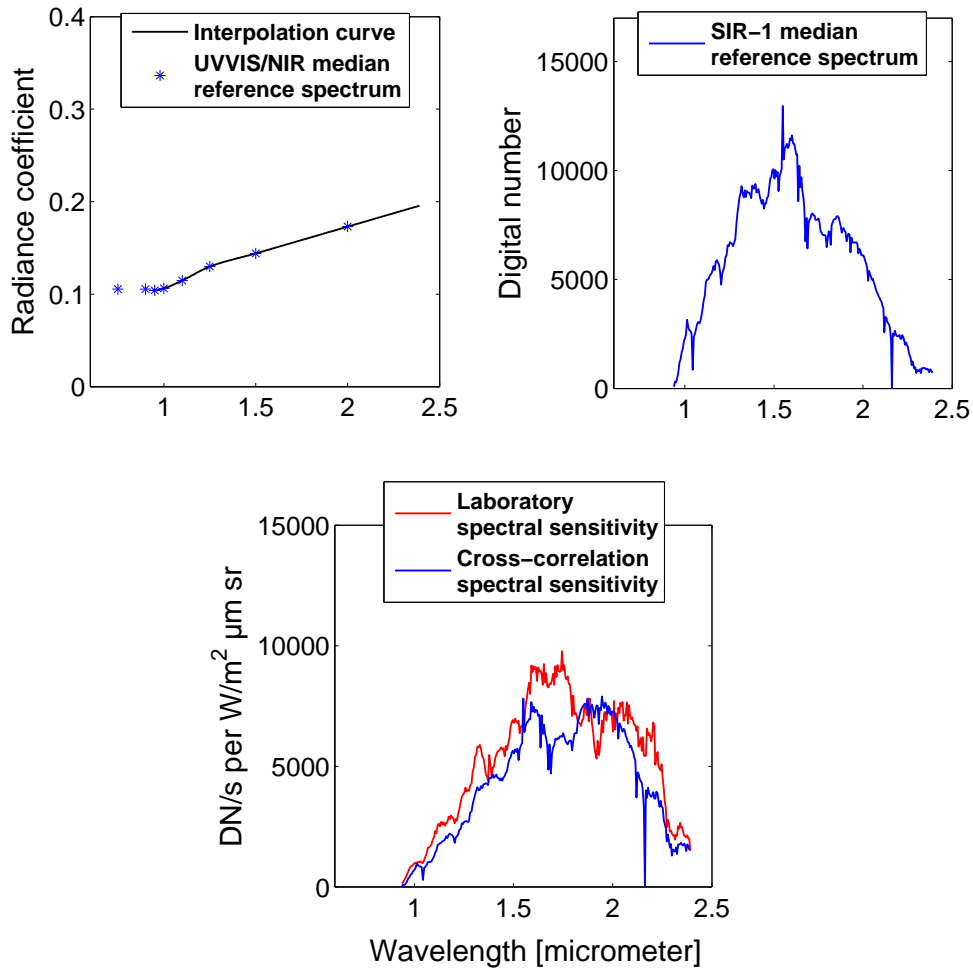
Figure 2.8: Example for a cross-correlation. **Upper left panel:** Median UVVIS/NIR reference points together with the interpolation for the SIR-1 wavelengths. **Upper right panel:** Median SIR-1 digital number reference curve for the same area. **Lower Panel:** Spectral sensitivity measured in the laboratory (red) and spectral sensitivity derived from cross-correlation.

body would need to reproduce the radiation of a real object at a certain wavelength. In case of a perfect blackbody, as simplified here, the brightness temperature and the effective temperature are the same. For gray bodies, where the emissivity ϵ is lower than 1 but independent of wavelength, the relation between those two temperatures is $T_B = \epsilon T_{eff}$. Lawson et al. (2000) found that the Lambertian temperature model is a good approximation for the lunar surface temperature when observations are done at local noon, where the incident angle of the sun equals the latitude of the observed area. This is the high temperature case, for observations outside local noon the temperatures will be lower. To calculate the temperature variation with latitude we first approximate the maximum temperature at the subsolar point from energy balance,

$$T_{SS} = \sqrt[4]{\frac{(1-A)S_0}{\epsilon\sigma}}, \tag{2.1}$$

where A is the albedo, S_0 is the solar constant at 1 AU, σ is the Stefan-Boltzmann constant and ϵ is the emissivity which we assume to be one as for a perfect black body. If we insert this temperature into the Lambertian temperature model,

$$T = T_{SS}\cos^{\frac{1}{4}}(i) \tag{2.2}$$

we get a latitude dependent temperature for observation at local noon. In Figure 2.9 two examples for the variation of temperature with latitude for two different subsolar temperatures are displayed. One subsolar temperature for an average albedo of 0.15 (blue line) typical for the lunar highlands, and one for an average lower mare albedo of 0.07 (black line). Due to the lower reflectance in mare areas, more solar irradiation is absorbed and hence the surface is hotter. The monochromatic radiance of a body with an effective temperature T_{eff} that is in thermal equilibrium with its surrounding can be described by the Planck function:

$$U(\lambda, T) = \frac{2\pi hc^2}{\lambda^5} \frac{1}{exp(\frac{hc}{\lambda k T_{eff}}) - 1}. \tag{2.3}$$

The Planck function describes the distribution of intensity at different wavelengths, the so called blackbody spectrum. To estimate the influence of thermal radiation on lunar reflectance spectra in the infrared, several examples for spectral energy distributions are given in Figure 2.10. The blackbody spectrum of the sun at 1 AU is shown together with the expected spectra of the reflected sunlight and the blackbody spectrum of the lunar surface at different temperatures. To estimate the influence thermal radiation has on the measurements, the percentage of thermal energy contributing to the measured "reflectance" signal for different temperatures in the near infrared is shown in Figure 2.11. No thermal contribution is visible in SIR-1 spectra and thus thermal radiation is neglected. Nevertheless the Clementine camera filters at 2.6 and 2.78 micrometer are already strongly influenced by thermal radiation and thus excluded from further analysis.
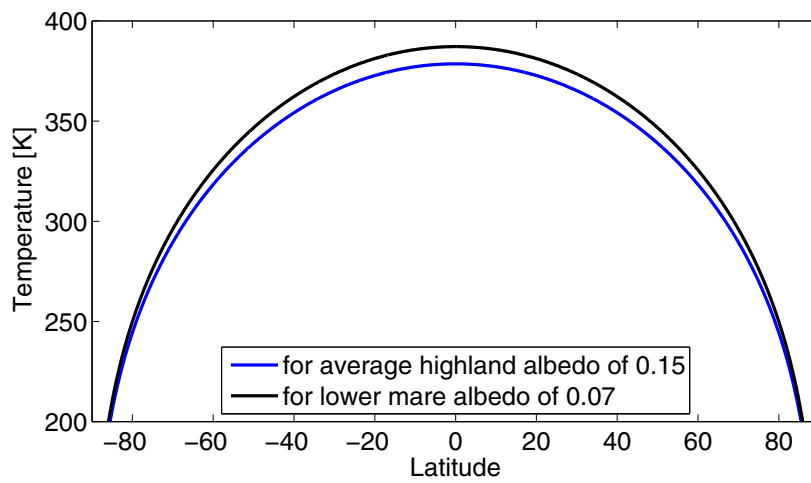
Figure 2.9: Variation of surface temperature with latitude in case of local noon. Curves were calculated using the Lambertian temperature model for two typical lunar albedos.
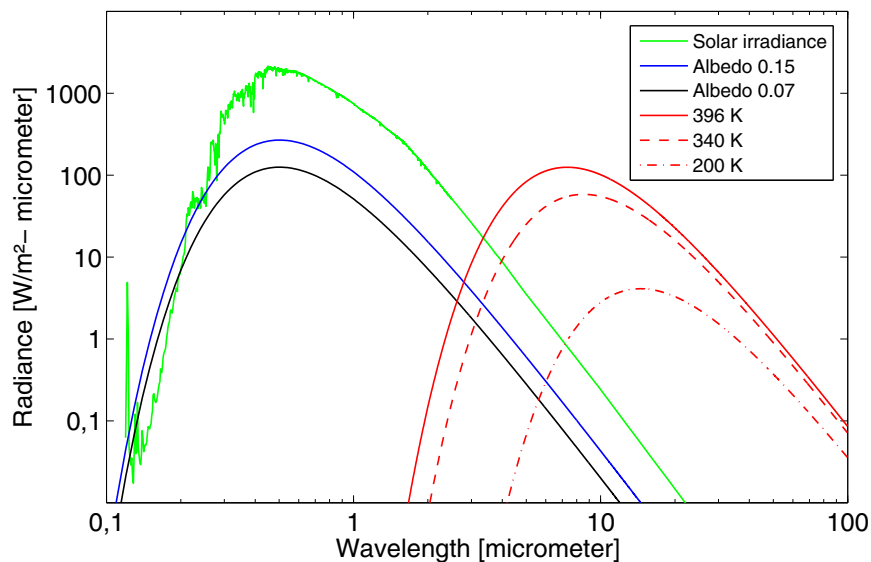
Figure 2.10: Planck functions for the sun (green), sunlight reflected from surfaces with albedos of 0.15 (blue) and 0.07 (black), and curves of the thermal radiation of the lunar surface at different temperatures (red). For higher lunar surface temperatures the thermal contribution starts to exceed the signal from reflected sunlight between 2 and 3 micrometer, at the intersections of the thermal radiance (red) and reflected radiance (black,blue) curves.
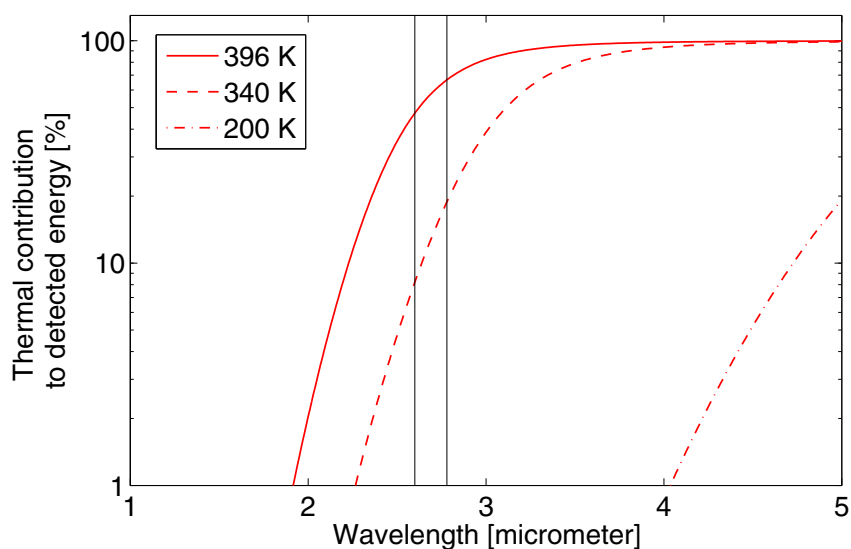
Figure 2.11: Thermal contribution to the total detected energy (emitted and reflected). For the highest measured lunar surface temperature of 396 Kelvin the thermal contribution to the largest wavelength of SIR-1 of 2.4 micrometer is 20 percent. This high temperature is only reached at zero latitude and local noon. Usually the thermal contribution for SIR-1 is much lower. At 2.4 micrometer for a surface temperature of 340 Kelvin (noon, 45 degree latitude) the contribution is only 3 percent. The two black lines indicate the Clementine NIR filter at 2.6 and 2.78 micrometer. Here the thermal contribution is larger even at lower surface temperatures.

2.4 Structure of Clementine UVVIS and NIR image mosaics
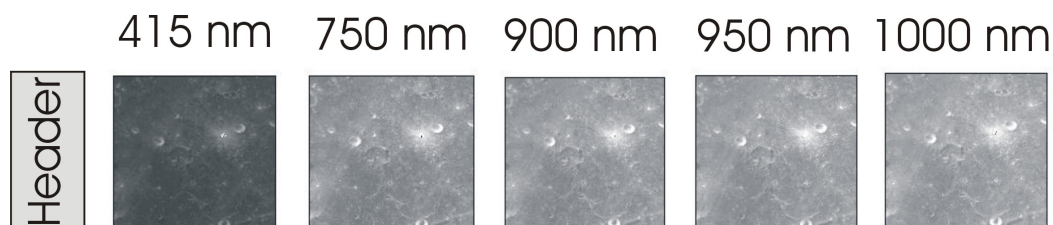
Figure 2.12: Files for the image mosaics contain a header, with keywords necessary for data extraction and the images for the different filters. This is the scheme for the UVVIS camera images. For the NIR images just one more image is stored in the file.

Clementine was the first extensive mission to the Moon after the Apollo program. This project was a cooperation between the Ballistic Missile Defense Organization and NASA to test lightweight imaging sensors and new component technology. During the two month of mapping in 1994, the complete lunar surface was covered. On board were several scientific instruments. Six cameras: the High-Resolution camera (HIRES), the Ultraviolet/Visible camera (UVVIS), the Near-Infrared camera (NIR), the Long-Wavelength Infrared camera (LWIR) and two star tracker cameras. Additionally two radar experiments: the Laser Image Detection and Ranging System (LIDAR) and the Bistatic Radar Experiment and a Charged Particle Telescope (CPT) for monitoring the highly energetic protons and electrons. In this study the images of the Ultraviolet/Visible camera (UVVIS) and the Near-Infrared camera (NIR) are used for comparison with our point spectrometer data. After calibration the UVVIS image mosaic was released in 1999 followed by the NIR image mosaic in 2007. Those image mosaics are used as a second data set in this study. More precisely the "Full Resolution Clementine UVVIS Digital Image Model" [2] a radiometrically, geometrically and photometrically modeled mosaic built from over 400000 images is used as source of the UVVIS camera images. This mosaic is accessible on Internet through the PDS imaging node, an archive which distributes the data from NASA missions. Data of the UVVIS Digital Image Model are separated into 78 data volumes (cl_4001-cl_4078), each covering a certain portion of the lunar surface. In every volume comprehensive description about the data product can be found. The subdirectory "data" contains the different images. All files are stored as ASCII stream-record files. NIR data are maintained from the "Clementine NIR Full-Resolution Lunar Mosaic (V. 0.1)" [3], which is also available on the Internet. This mosaic is split into 13 main directories (DCL_5001-DCL_5013). Each directory contains six subdirectories adding up to an overall of 78 data volumes alike the UVVIS mosaic. Image filenames are composed of three parts, the camera identification (ui,ni) and the latitude [s(outh)/n(orth)] and longitude of the image (e.g. ui73s247.img, ni73s247.img). Those images are read into Matlab matrices. Each image file consists of a header and a data section. The Images of the

---

[2]http://pds-imaging.jpl.nasa.gov/Admin/resources/cd_clementine.html#clmUVVIS
[3]ftp://pdsimage2.wr.usgs.gov/cdroms/clementine/Clem_NIR_V0.1

five UVVIS filters, respectively the six NIR filters, are stored consecutively in the data
sections of the image files (see Figure 2.4). The PDS keywords

- UVVIS_RECORD_BYTES

- UVVIS_LABEL_RECORDS

specify the size of the header and the keywords,

- UVVIS_LINES

- UVVIS_LINE_SAMPLES

specify the size of each image block. Once the images are transformed to matlab matrices,
the SIR-1 latitude and longitude coordinates can be converted to line and sample pixel
coordinates according to the Clementine UVVIS/NIR images.

$$
\begin{aligned}
\text{Line} \;=\; & \text{LINE\_PROJECTION\_OFFSET} - \\
& (\text{Latitude} \cdot \text{MAP\_RESOLUTION}) & (2.4) \\
\text{Sample} \;=\; & \text{SAMPLE\_PROJECTION\_OFFSET} + \\
& (\text{Longitude} - \text{CENTER\_LONGITUDE}) \times \\
& \text{MAP\_RESOLUTION} \cdot \cos(\text{Latitude(radian)}) & (2.5)
\end{aligned}
$$

Both Clementine mosaics are mapped in a sinusoidal equal-area projection. The keywords

- LINE_PROJECTION_OFFSET

- MAP_RESOLUTION

- SAMPLE_PROJECTION_OFFSET

- CENTER_LONGITUDE

determine the position and scale of an image within the overall coordinate system of the
lunar mosaics. Given the SIR-1 footprint coordinates and viewing geometry we calculate
the shape of the footprint of SIR-1 and find the corresponding Clementine UVVIS and
NIR pixels. The average of those pixels within one footprint measurement is the value
suited for comparison with the SIR-1 spectra. From the eleven filters of the UVVIS and
NIR camera we obtain spectra with eleven measurements between 0.451 and 2.78 mi-
crometer for comparison with the 256 measurements between 0.9 and 2.4 micrometer of
SIR-1. Hence for the first time we can compare spectral reflectance measurements of
large parts of the lunar surface which were directly taken from lunar orbit. The Clemen-
tine UVVIS/NIR images provide us with the radiance factor at the different filter wave-
lengths. This is the bidirectional reflectance compared to a Lambert surface, which emits
all incident irradiance isotropically into all direction and has a bidirectional reflectance of
$r = cos(i)/\pi$, where i is the solar incident angle.

2.5   Alignment of Clementine and SIR-1 coordinates

In an ideal case the latitude and longitude values of one lunar surface spot would match for both data sets. Those coordinates were calculated from the respective SPICE data of each mission and further processed with mission specific software tools. Uncertainties in spacecraft orientation and instrument angles lead to uncertainties of coordinates. Those coordinate shifts can be analyzed and corrected. All Clementine mosaics were tied to the geometry of the Clementine Basemap mosaic at 0.75 micrometer. This map was established by least-square analytical triangulation of about 265000 match points. The topography was neglected and a constant radius of 1737.4 km was assumed for the Moon.

Because the SIR-1 spectrometer does not provide us with images, we employ images taken by other instruments for the geologic background. Together with SIR-1, the Advanced Moon micro-Imager Experiment (AMIE) observed the lunar surface. Due to instrument and calibration problems no comprehensive compilation of AMIE pictures with controlled coordinates is available yet. Therefore the Clementine image mosaics are used in this study.

The correction of the offset between Clementine UVVIS/NIR image coordinates and SIR-1 target coordinates is calculated via the intensity variation of both data sets along a certain orbit. The offset is usually lower than +/- 0.5 degree in latitude and longitude direction. To find the right offset, the SIR-1 coordinates are systematically shifted within an interval of -1 to 1 degree independently for latitude and longitude direction around the original SIR-1 target coordinates with a variable precision. A precision between 0.05 and 0.005 degree is used. On ground a precision of 0.01 degree corresponds to approximately 300 meters, or 3 UVVIS/NIR pixel. At each coordinate iteration the corresponding footprint data from Clementine UVVIS/NIR images is extracted. For this routine a square footprint is assumed. This is sufficient to match the lightcurves. Later, the elliptical shape of the footprint is taken into account for the reflectance data extraction. The average intensity of the Clementine filters at 1, 1.1 , 1.25, 1.5 and 2 micrometer is compared with the average intensity of the 256 SIR-1 pixel along a SIR-1 orbit track. Both lightcurves are scaled through their minimum-maximum range into the same intensity scale for UVVIS/NIR data is available in radiance factor and SIR data in digital number values. The optimization is done via a minimization of the difference of both lightcurves. In Figure 2.13 this coordinate shift is demonstrated for a SIR-1 orbit over Mare Humorum. The change in absolute differences between both lightcurves with changing coordinate shift is shown in Figure 2.14. The minimum of the refined alignment procedure (Figure 2.14, left panel) indicates the optimal coordinate shift. On ground the coordinate shift can lead to offsets up to several kilometers. Keeping in mind that an average footprint of SIR-1 has 1 kilometer diameter, the alignment of both datasets before UVVIS/NIR data extraction is crucial. At incident angles larger than 60 to 70 degree the alignment of lightcurves becomes impossible cause shadows and large scale roughness lead to diversion of lightcurves as can be seen in Figure 2.15 for a section of SIR-1 orbit 878. The coordinate shift shows some systematics with latitude and longitude, which can be examined through the alignment of many orbit intervals all over the Moon. No simple relation between lunar latitude and longitude and the orbit shift that has to be applied was found. Hence each orbit has to be

aligned individually.
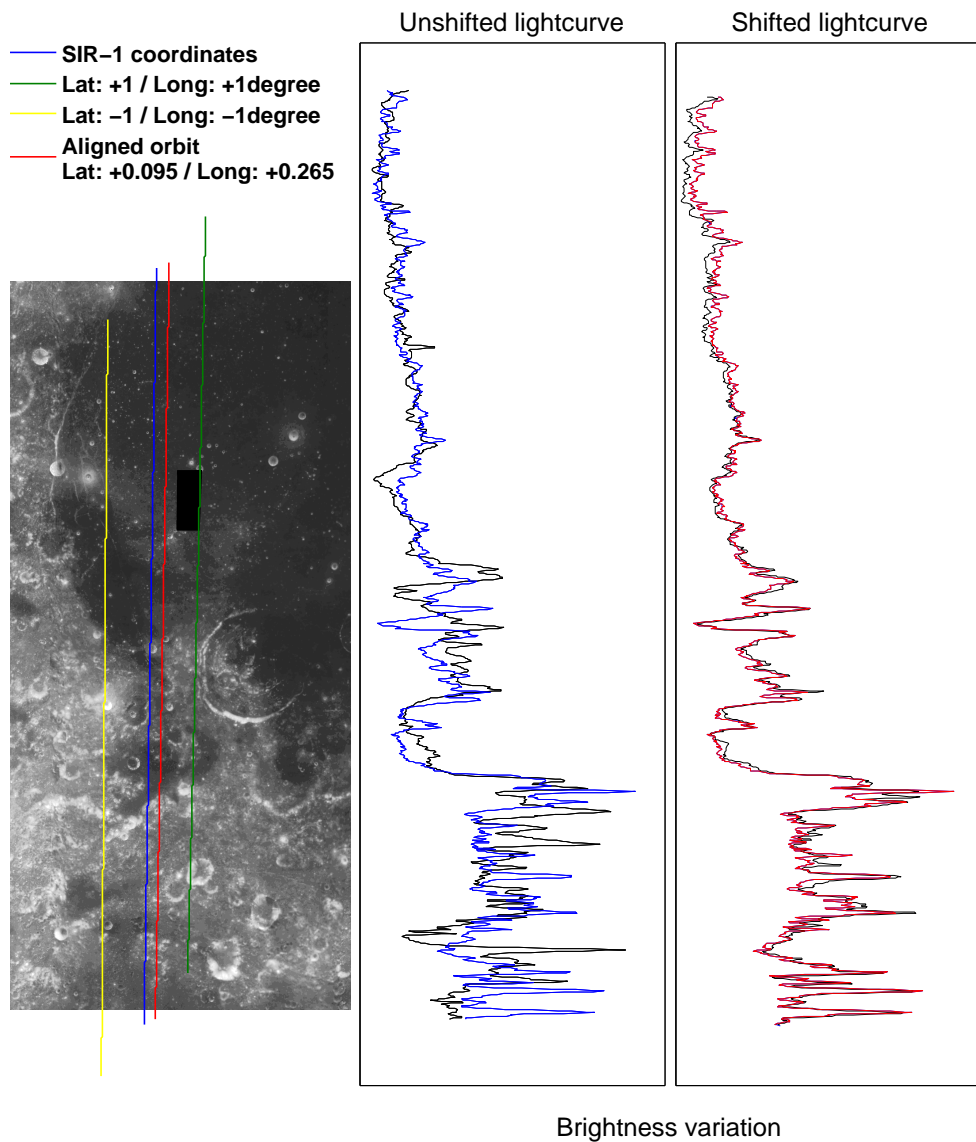
Figure 2.13: **Left panel:** SIR-1 orbit with original coordinates [blue] and optimized coordinates [red]. A shift of 0.095 degree in latitude and 0.265 degree in longitude is applied. **Center panel:** intensity variation without coordinate alignment (SIR-1 [blue], Clementine UVVIS/NIR [black]). **Right panel:** intensity variation with coordinate alignment. (SIR-1 [red], Clementine UVVIS/NIR [black]).
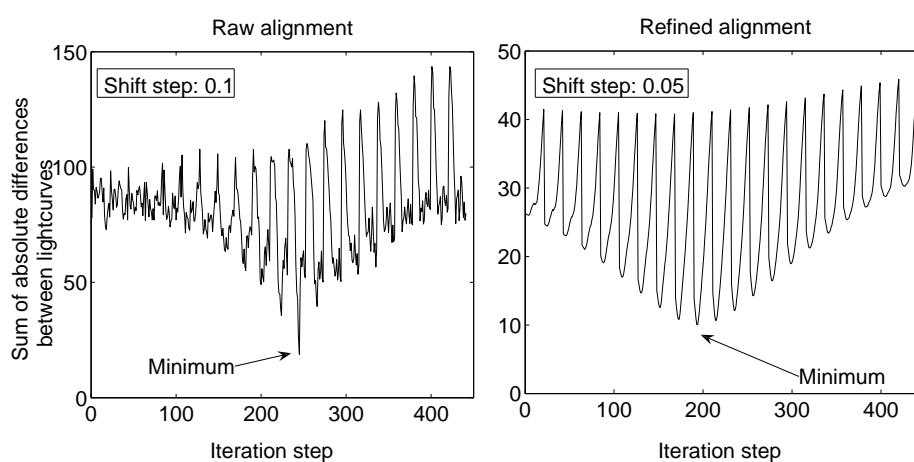
Figure 2.14: To find the optimal coordinate shift, the sum of the absolute differences of both lightcurves within the alignment interval is used. For a first raw alignment (left panel), the SIR-1 orbit is shifted between -1 to 1 degree in latitude and longitude, with shift steps of 0.1 degree, from the original SIR-1 coordinates. Around the minimum of light curve differences for this iteration, a second, refined analysis with a shift of +/- 0.1 degree in latitude and longitude direction, with a smaller stepsize is calculated (right panel). If the lightcurves match, the minimum of the second iteration gives the shift in latitude and longitude with which the SIR-1 coordinates can be transformed to the Clementine UVVIS/NIR coordinate system.
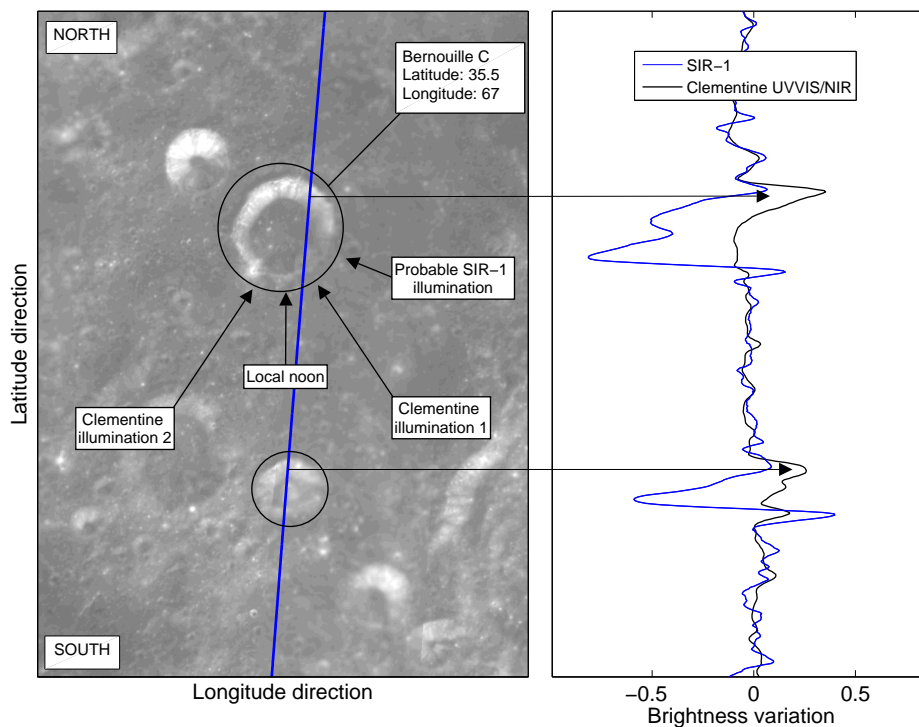
Figure 2.15: SIR-1 orbit 878 (blue) crossing the craters Bernouille C and F. Clementine images are mosaics of image strips taken during different times of the mission. Thus it happens, as in this image, that different image parts, have different illumination conditions. Our orbit crosses in the image part which is illuminated under Clementine illumination condition 2 (Arrows indicate illumination direction). The local noon arrow, indicates the direction of illumination at local noon, directly from the south. The aligned SIR-1 and Clementine UVVIS/NIR light curves indicate differences in illumination during both observations. SIR-1 observations where taken with an average incident angle of 60 degree well outside of the local noon. Clementine usually observed nearby local noon, which at latitudes of 35 degree relates to a minimum incident angle of about 35 degree.
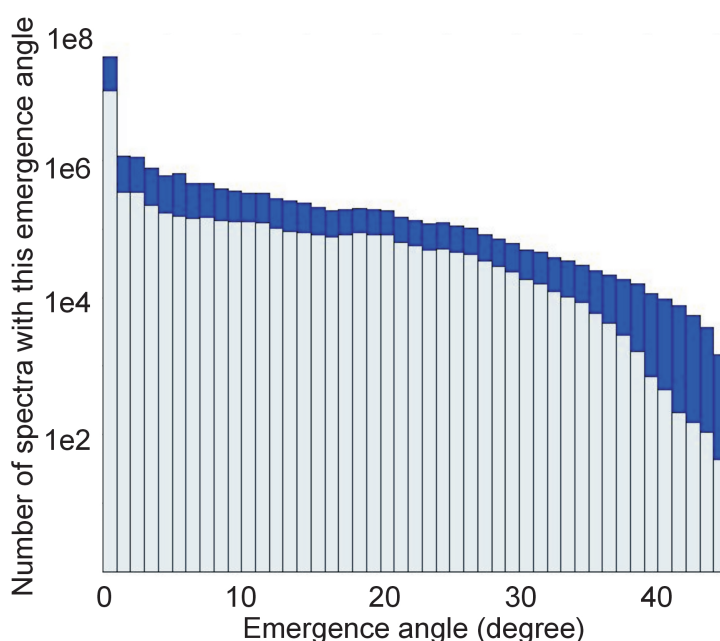
Figure 2.16: Histogram of the emergence angle distribution for all SIR-1 spectra in intervals of 2 degree. The blue bars show the distribution for all spectra, the light gray bars show the distribution for spectra with incident angles lower than 70 degrees.

2.6   Extract Clementine data - The shape of footprint

During the observations of SIR-1 the viewing geometry changed according to the evolution of the SMART-1 orbit. In Nadir observation, the emergence angle is zero and the shape of the footprint is circular. With increasing emergence angle the shape becomes more elliptic. Of the 28.6 million SIR-1 spectra 77 % were taken within two degree of Nadir position. Sufficient illumination with a solar incident angle of less than 70 degrees is reached for 13.9 million of all spectra, and 76 % of these have emergence angles lower than two degree. The distribution for emergence angle frequencies is displayed in Figure 2.16. Hence most of the SIR-1 footprints are circular. However, the accurate shape of the footprint ellipse is taken into account for comparison of SIR-1 and Clementine UVVIS/NIR data.

An example for an off-nadir observation of SIR-1 is shown in Figure 2.17. For this observation the subsurface coordinates of the spacecraft are about 30 degrees west of the observed footprint, the emergence angle is about 15 degree and hence the footprint is elongated into an elliptical shape.
In Figure 2.18 the geometry of observation and the projection of a footprint are displayed. Mathematically this problem is equivalent to a section between a cone with an opening angle equal to our viewing angle and an inclined plane, here the lunar surface. The lunar surface is assumed flat, surface roughness is not taken into account. For emergence angle
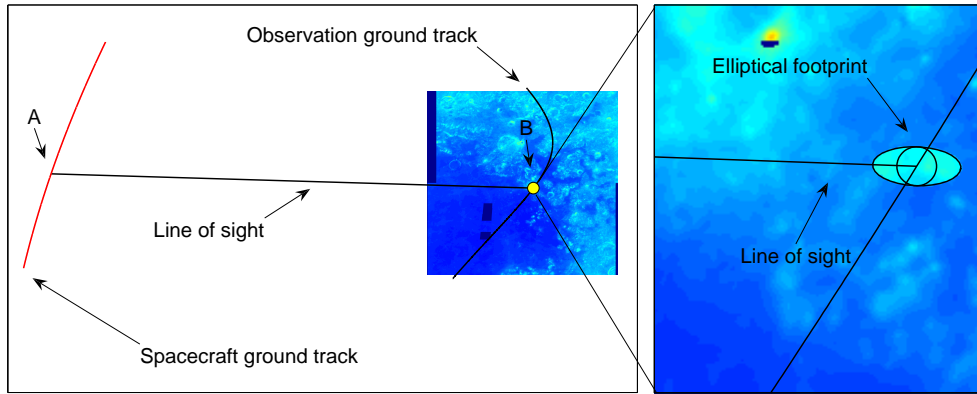
Figure 2.17: During orbit 2209, spectrum 11867 was observed under an emergence angle of about 15 degree. The subsurface coordinates of the spacecraft at point A (Latitude: 21.7 degree / Longitude: 33.8 degree) vary from the coordinates of the observed footprint at point B (Latitude: 20.6 degree / Longitude: 66.5 degree). Thus the footprint of this measurement is elongated in the line of sight between spacecraft position (A) and footprint center (B). In case of zero emergence angle the footprint would be circular and directly beneath the spacecraft.

zero, the viewing cone is perpendicular to the lunar surface, and the section as well as our footprint have circular shape. The intersection angle β between the viewing cone axis and the surface plane decreases as the emergence angle e increases ($e + \beta = 90°$). The cone section, and thus the SIR-1 footprint become more elliptic. For each measured spectrum we know the distance between the spacecraft and the observed footprint d_{so}, the coordinates of the footprint center, the coordinates straight below the spacecraft and the emergence angle. If the emergence angle is close to zero the coordinates of the observed footprint and of the sub-surface point of the spacecraft coincide. The distance between spacecraft and surface d_{ss}, and the distance between spacecraft and observed footprint d_{so} are similar. A footprint ellipse is determined by two axes a and b, were a is larger than b, and by the numeric eccentricity ϵ calculated from the axis of the ellipse.

$$\epsilon = \sqrt{1 - \left(\frac{b}{a}\right)^2} \tag{2.6}$$

When considering the footprint ellipse as a conic section between the SIR-1 viewing cone and the lunar surface plane, the numeric eccentricity can also be calculated as

$$\epsilon = \frac{cos(\frac{\phi}{2})}{cos(\beta)}, \tag{2.7}$$

where ϕ is the viewing angle of the spacecraft and β is the intersection angle between the central axis of the viewing cone and the surface plane, both known variables. To find the correct description of the footprint ellipse we have to determine the three unknown variables a, b, and ϵ from the known variables e, ϕ, d_{so}, and β. Given the distance from spacecraft to observed surface, d_{so}, and the known viewing angle ϕ we can calculate the
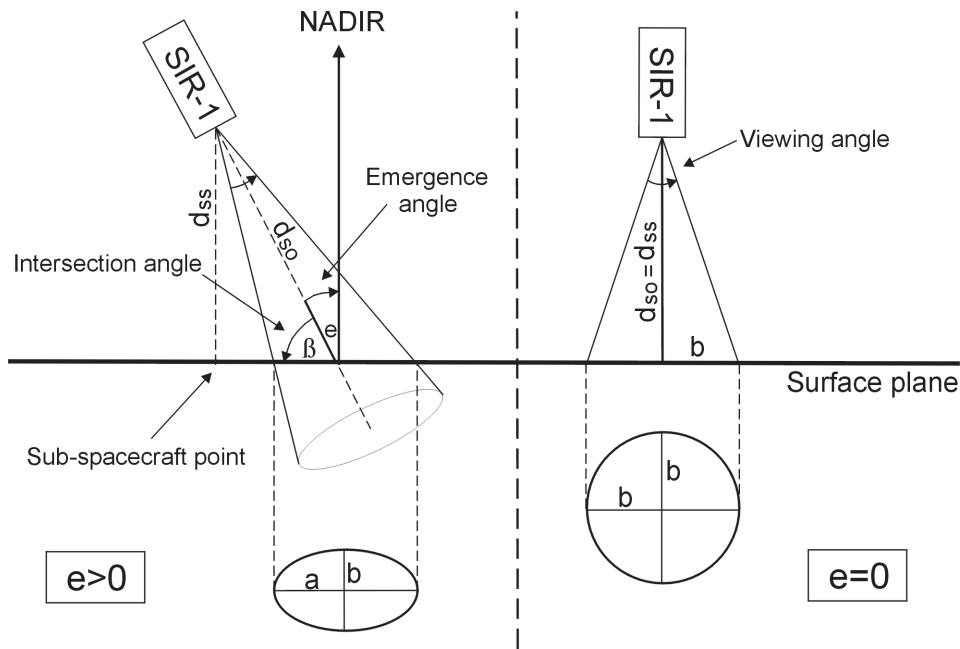
Figure 2.18: Illustration of footprint ellipse projection. In the left panel, the emergence angle is larger than zero. The line of sight and the surface plane intersect at an angle β. The short axis b of the footprint ellipse is independent of the emergence angle, and is calculated from half the viewing angle and the spacecraft surface distance d_{so}, as shown in the right panel for emergence angle zero.

shorter axis b (see Figure 2.18, left panel). Axis b is perpendicular to the line of sight and depends only on spacecraft altitude and viewing angle:

$$b = tan\left(\frac{\phi}{2}\right)d_{so}. \tag{2.8}$$

Knowing b (Eq. 2.8) and ϵ (Eq. 2.7) we can calculate axis a from rearranging equation 2.6 so that

$$a = \sqrt{\frac{b^2}{1 - e^2}}. \tag{2.9}$$

The axes a and b are in units of meter, and have to be converted to the Clementine image pixel coordinate system. The usual size of image pixel in Clementine images is 100 meter. Hence division of a and b by one hundred transforms the axis length to pixel values. Now we describe the ellipse in carthesian coordinates within the UVVIS/NIR image.

$$\frac{x^2}{a^2} + \frac{y^2}{b^2} = 1. \tag{2.10}$$

For extracting the elliptical footprint from Clementine images we have to define the shape and orientation of the footprint ellipse within the Clementine image coordinate system. In Figure 2.19 the steps of creating a footprint ellipse are illustrated. Clementine images are oriented with north upwards and south downwards. The origin of the image coordinate system is in the upper left corner of each image. The x-direction points to positive
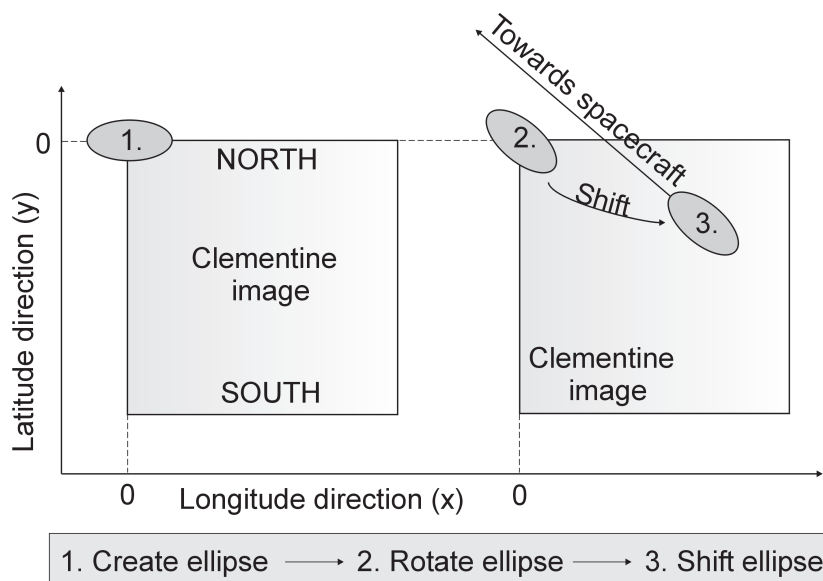
Figure 2.19: For the extraction of the SIR-1 footprint, first the shape of the ellipse is calculated, then the ellipse is rotated towards the line of sight and shifted to the actual footprint coordinates within a Clementine image.

longitude direction, the y-direction points to negative latitude direction. So the first pixel is usually the most northern, most western point of each image. With the known parameters (a,b,ϵ) of the footprint ellipse, we create an ellipse with the long axis a, along the x-direction at the origin (0,0). The orientation of the ellipse is defined by the line of sight projected onto the lunar surface. Therefore the vector between the footprint and the sub-spacecraft point is calculated and the ellipse is rotated, so that the long axis is parallel to the line of sight. In a last step the ellipse is shifted to the pixel coordinates of the actual footprint. For the extraction of Clementine pixel within a SIR-1 footprint, the ellipse is approximated by a polygon with 33 corners. The matlab routine "poly2mask" identifies the pixel coordinates of pixel within this polygon. The mean of the reflectances of those pixel is then compared to the SIR-1 point spectra.

2.7 SIR-1 data reduction

Before combining the two datasets, we have to calibrate the SIR-1 raw spectra. A set of routines written by Esa Vilenius is used for calibration. To understand the different steps of calibration, we first need to explain the basic principle of the SIR-1 infrared detector.

The detector consists of 256 pixels, each one a photodiode, in which incoming light produces electron-hole pairs that are collected on a condensator and converted into a voltage. This voltage is added to a basic voltage, the so called bias voltage which has to be subtracted again later to get the real signal. The analog voltage is translated into a digital signal via an Analog to Digital converter. This digital signal is the raw spectrum.

Electron-hole pairs can be produced by two processes: by photons from the light signal we want to detect and by thermal noise generating the so called dark current. The dark current is temperature-dependent and is already greatly reduced by operating the detector at deep temperatures (e.g. -50 °C). Laboratory calibrations of the instrument prior to launch as well as on-board calibrations using the lunar darkside result in a reliable subtraction of the bias and dark signal.

At this point the spectra only contain the reflected light signal measured. But still illumination conditions vary between measurements of different orbits. Due to laboratory standards for Apollo samples all SIR-1 spectra are reduced to an observing geometry of i=30 °,e=0 °,g=30 °. The same observing geometry was used for calibration of Clementine UVVIS/NIR spectra, which makes both datasets comparable.

For each spectrum, incident, emergence and phase angle are known. In a first step the observing geometry is reduced to zero incident, emergence and phase angle using a so called phase function, which relates the measured reflectances of the same surface spots at different phase angles. Thereupon measurements are transfered into standard-observation geometry.

For SIR-1 data calibration the phase function from Shkuratov et al. (1999b) is used.

3 MODELING OF SPECTRA

The previous chapters introduced a method to retrieve combined data from corresponding surface areas observed with the SIR-1 point spectrometer and the Clementine UVVIS/NIR cameras. Those absolute calibrated reflectance spectra need to be modeled to determine the surface mineralogy in the area of interest. Variations in lunar surface mineralogy are not arbitrary. From Apollo sample analysis we have ground truth knowledge about the abundance range of the four major lunar minerals (plagioclase, pyroxene, olivine, ilmenite) and their compositional range within the mineral groups. These mineral groups are described in detail in Section 1.4. The goal of the model is to determine the mass

Table 3.1: Steps for modeling an absolute reflectance spectrum. The modeled absolute reflectance spectrum is then compared with the measured absolute reflectance spectrum.

Step	Action	Input	Output
1.	Derive single scattering albedos using reflectance spectra of samples with controlled composition.	Laboratory reflectance spectra	Single scattering albedo w
2.	Derive absorption coefficient of small iron particles within a transparent medium to model space weathering	n and k of iron, volume fraction of iron	absorption coefficient of iron, α_{Fe}
3.	Calculate the space weathering effect on the mineral components	w of the unweathered components and α_{Fe}	w_{sw} of the space weathered components
4.	Compose an intimate mixture of the weathered pure components and calculate the radiance coefficient of the mixture	w of the weathered components	Radiance coefficient of a space weathered intimate mixture (absolute reflectance spectrum)
5.	Compare the modeled spectrum to the measured spectrum using a least square fitting algorithm	Modeled spectrum and measured spectrum	Mass fraction of the minerals in the sample spectrum, effective grain size, volume fraction of iron, porosity

fraction of plagioclase, pyroxene, olivine, ilmenite and agglutinates; the compositional abundances of four pyroxenes representing the possible lunar pyroxene variations; the degree of space weathering; the effective particle size of a location.

Four main resources of spectral information are available for analysis of lunar infrared reflectance spectra. First the **laboratory measurements**. In the seventies a first comprehensive study about visible and near-infrared spectra of natural samples of different minerals and rocks was published (Hunt and Salisbury (1970), Hunt et al. (1973, 1974)). Since then many detailed studies have been conducted: on the effects of mineral abundances in mixtures, on the elemental abundances in minerals of the same mineral group, on the effect of grain size, of observing geometry, of impact related shock pressures, and of different temperatures as present at planetary surfaces in the solar system.

The second important source of information, a subsource of the laboratory measurements, are the **Apollo samples**. Besides Earth, we have ground truth for samples with known sample location only for one other planetary body in the solar system, the Moon. Additionally, about 36 meteorites (Jolliff et al. 2006, p.12), of supposed lunar origin were found on Earth.

The third source is **ground observations**. Albeit limited in resolution and by the influence of Earth's atmosphere, those studies gave us first insides into the surface mineralogy of the lunar near side. This approach is still used to study the lunar surface and to calibrate and verify space based measurements.

Since reuptake of regular lunar exploration with satellites by the Clementine mission in 1994, a large amount of **lunar remote sensing data** was collected. This is the fourth data resource available for lunar studies. Instruments for visible, infrared, gamma-ray, X-ray, radar, laser altitude and magnetic field observations are the standard equipment of most lunar missions.

Clementine UVVIS and NIR camera data are predominantly analyzed using color index relations derived from laboratory analysis of Apollo samples or from cross correlations with element measurements from gamma-ray observations. These color indices establish a connection between the albedo of a surface at two or three different wavelengths and the abundance of certain elements, for example iron or titanium (Blewett et al. 1997, Lucey et al. 2000a). The interpretation of these color index images was very successful, yet problematic, because the variations in color indices used for analysis are small for the space weathered spectra of the Moon, and the laboratory calibrations turned out to be less sure when extended over a larger selection of Apollo samples, or compared to neutron spectrometer estimates. Especially the TiO_2 abundances have large errors about 50 % (Jolliff et al. 2006, p.188), when retrieved from color indices. Nevertheless it is an interesting approach we can employ to retrieve additional information about elemental abundances from average Clementine UVVIS/NIR spectra corresponding to SIR-1 point spectra.

The high-resolution spectra of SIR-1 and SIR-2 give us the opportunity to address the

mineralogy directly through the shape of the whole spectrum between 0.9 and 2.4 micrometer. Utilizing the bidirectional reflectance theory we retrieve mineral abundances of plagioclase, pyroxene, olivine, ilmenite and agglutinate; volume fraction of small microscopic iron particles, the main agent of space weathering; effective particle size of the soils covering the uppermost area of our footprint; and porosity.

For modeling, absolute reflectance spectra derived from cross-correlation with Clementine UVVIS/NIR data are employed. The absolute calibration through cross-correlation cannot be established for all SIR-1 spectra with prominent absorption bands, which are part of this study. When the observation conditions of SIR-1 and Clementine UVVIS/NIR measurements are to deviant, when the noise of the SIR-1 instrument is to high at low albedo surfaces for short exposure times, when no strong intensity variations for an orbit alignment are available in an area, the adjustment of lightcurves between SIR-1 and Clementine as described in section 2.5 is sometimes impossible.

To test the results of the model we have in principle two possibilities. The comprehensive database on composition and reflectance spectra of Apollo sample soils provide a complete dataset of reflectance spectra from samples with known composition. Hence we can use the Apollo sample suit to test our program by modeling Apollo soil reflectance spectra and comparing the results with the detailed laboratory analysis available for some of the samples. Apollo soil spectra represent lunar surface materials and show us on centimeter scale what we can expect from kilometer scale spectral reflectance measurements. After tests with Apollo soil spectra, one could see that these strongly space weathered materials offered to weak features to retrieve unique solutions, comparable to the laboratory analysis. Most soil spectra exhibit only a very weak absorption at 1 micrometer and a strong slope, and many combinations of model parameters produce the same spectral shape. In our analysis we concentrate on spectra that exhibit stronger absorption features, from sample areas relatively recently exposed at the lunar surface and thus less space weathered.

A second option is to model artificial lunar analog spectra, composed from known endmembers. Several of those studies have been conducted (Mustard and Pieters 1989, Hiroi and Pieters 1994), and these reflectance spectra are in parts available from the RELAB database, so that they can be used to test the model routine with known endmembers for mixtures of controlled composition. After presenting the input to the modeling routine and identifying control options, now the approach is explained in detail.

This model is based on the theory of bidirectional reflectance from Bruce Hapke. Since 1981, Hapke published a series of papers (Hapke 1981, Hapke and Wells 1981, Hapke 1984, 1986, 1993, 2002, 2008) for a theory of an approximate solution for the radiative transfer equation for reflectance measurements. Other theories for modeling light scattered from planetary surfaces are available (Shkuratov et al. 1999a). However, Hapke's theory is widely applied for analysis of planetary and asteroid surfaces, is easy adoptable to new situations and a way of introducing space weathering is available (Hapke 2001), which is crucial for modeling lunar reflectance spectra. The bidirectional reflectance is calculated as follows:
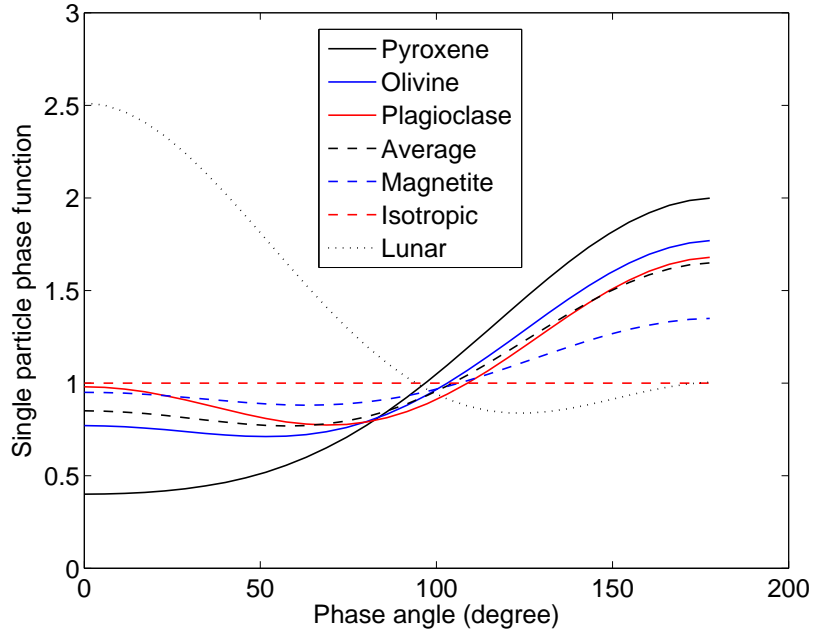
Figure 3.1: Single-particle phase functions for different minerals (Mustard and Pieters 1989). Pyroxene (b=-0.8,c=0.2), Olivine (b=-0.5,c=0.27), Plagioclase (b=-0.35,c=0.33), Average (b=-0.4,c=0.25), Magnetite (b=-0.2,c=0.15) , Isotropic (b=0,c=0) and an average single-particle phase function for the lunar surface (Hapke 1963). The phase functions for the different minerals are calculated following equation 3.8.

$$r_B = K \frac{w}{4\pi} \frac{\mu_0}{\mu_0 + \mu} ([1 + B(g)]P(g) + H(\mu_0)H(\mu) - 1). \tag{3.1}$$

The single scattering albedo w, is the ratio between the scattering efficiency Q_S and the extinction efficiency Q_E which includes both absorption and scattering ($Q_E = Q_S + Q_A$). Thus w gives the probability that an interacting photon is rather scattered than absorbed, when light passes through a particle. This value changes with wavelength and is distinctive for each mineral. Unlike the absorption coefficient, the single scattering albedo depends on particle size, and increases with decreasing particle size, because for small particles scattering is stronger than absorption due to their larger surface/volume ratio.

The observation geometry is represented by μ_0, the cosine of the incident angle, by μ, the cosine of the emergence angle and by g, the phase angle between incident and emergent light as shown in Figure 2.5, where the observing geometry is illustrated.

The angular scattering pattern for nonisotropic scattering particles is described by the single-particle phase function $p(g)$. Several example phase function are displayed in Figure 3.1; for isotropic scatterers, for the lunar surface regolith (Hapke 1963), and single-particle phase functions for different minerals adopted from Mustard and Pieters (Mustard and Pieters 1989).

At small phase angles, an unusual surface brightening known as opposition effect is present for particulate surfaces. This comes from shadow-hiding when less shadows from upper grains on lower grains are visible, when shadows are directly behind the grains that cast them. The effect is described by the coherent backscatter function $B(g)$, and termed opposition effect:

$$B(g) = \frac{B_0}{1 + (1/h)tan(g/2)}.$$ (3.2)

The parameter h is the angular width of the opposition effect, which depends strongly on the material and varies slightly with wavelength. For the Moon h is about 0.05 (Hapke 1986). B_0 is the magnitude of the opposition effect and can be assumed 1 for the Moon (Hapke 1981).

For SIR-1 and Clementine measurements the spectra are reduced to a standard geometry of incident angle 30 degree and emergence angle zero degree. This standard configuration is also applied for most measurements of lunar samples in laboratory. At a phase angle larger than 15 degree the opposition effect becomes neglectable (Mustard and Pieters 1989), and therefore we do not consider it for further modeling ($B(g) = 0$). The Chandrasekhar H-function accounts for the multiple scattered part of the light. The approximation for isotropic particles is

$$H(x) = \frac{1 + 2x/K}{1 + 2\gamma x/K} \quad \text{with} \quad \gamma = \sqrt{1 - w} \quad \text{and} \quad x = [\mu_0, \mu].$$ (3.3)

For anisotropic particles another approximation is available (Hapke 2002), with the main difference of reducing the value of the H-function for large single scattering albedos w. Nevertheless, the recently introduced porosity parameter K (Hapke 2008) is only defined for the isotropic approximation. Furthermore, the inversion of laboratory reflectance coefficients to single scattering albedos w, has proven impossible within the allowed physical range of w between 0 and 1 for high-albedo powders, when the anisotropic approximation was used. Hence, for retrieval of w as well as for modeling of lunar spectra, the isotropic approximation is used.

The parameter K which approximately resides between 1 and 6 accounts for sample porosity by varying the filling factor ϕ, which is the fraction of sample volume occupied by particles:

$$K = \frac{-\ln(1 - 1.209\phi^{1/3})}{1.209\phi^{2/3}}.$$ (3.4)

The porosity is connected to the filling factor ϕ through $P = 1 - \phi$. Thus with increasing filling factor the porosity decreases. For $\phi \ll 1$, K becomes approximately one and the radiance coefficient converges towards the old equation without porosity. Hence, before porosity was included, the particulate medium was treated as if close to 100 percent porosity, which would translate into widely separated particles. The bidirectional reflectance with porosity is determined for filling factors ϕ between close to zero and 0.75, which

is able to account for porosities of common particulate samples having values between 45 and 93 percent porosity (Shepard and Helfenstein 2007). Of two sample reflectance spectra which agree in all parameters except porosity, the high porosity (looser) sample will exhibit lower reflectance.

Usually in laboratory the radiance coefficient, which is the bidirectional reflectance relative to a lambert sphere, is measured. A Lambert sphere reflects isotropically in all directions. All of the incident light is reflected, so that the reflectance of a Lambert sphere is

$$r_L = \frac{\mu_0}{\pi}. \tag{3.5}$$

If the bidirectional reflectance is divided by the reflectance of a lambert sphere identically illuminated (μ_0 equal), we obtain the radiance coefficient:

$$r_c = \frac{r_B}{r_L} = K\frac{w}{4}\frac{1}{\mu_0 + \mu}([1 + B(g)]P(g) + H(\mu_0)H(\mu) - 1). \tag{3.6}$$

Clementine UVVIS/NIR images were absolutely calibrated with a laboratory reflectance spectrum of Apollo sample 62231. Through cross-calibration our measurements become radiance coefficient reflectances as for laboratory spectra. In this work we solely use the radiance coefficient, hence all reflectance spectra are radiance coefficient spectra. The different coefficients of the equation describe the aspects of reflection on a particulate medium.

To model a reflectance spectrum, we pass through five successive steps (see also Table 3.1), which will be explained in detail in the following sections.

1. First the single scattering albedos w from reflectance spectra of pure mineral samples with controlled composition are derived. These spectra are available in the RELAB[1] database. Only samples with controlled lower and upper particle size limits are suitable. Measurement angles must satisfy standard observation conditions of 30 degree incident and phase angle and zero degree emergence angle. Measured wavelength range must suit the desired model wavelengths.

2. Application of space weathering is prepared by deriving the absorption coefficient of small iron particles within a transparent host medium. Host media are the major minerals of the lunar surface. Technically this is a simplification, because small iron particles are predominantly found at the rims of grains, and only for agglutinates entered the matrix of a grain through melting and welding together of several grains and their iron containing rims.

3. Then the space weathering effect on each major mineral component is calculated for a given volume fraction of iron that defines the degree of space weathering.

4. Subsequently an intimate mixture using the space weathered single scattering albedos w_{sw} of the major mineral components is composed.

---

[1]http://www.planetary.brown.edu/relabdata/

5. In the end an artificial reflectance spectrum is computed and compared to the measured reflectance spectrum employing a least-square fitting algorithm. Parameters used for computing the best-fit artificial spectrum such as mineral endmembers, mineral mass fractions, effective grain size, iron volume fraction, porosity and single particle phase function, are assumed to represent also the real values of the measured surface sample.

3.1   Single scattering albedos from inversion of laboratory reflectance spectra

In the radiance coefficient equation (Eq. 3.6), the characteristic behavior of each mineral is represented through the single scattering albedo w. This wavelength-dependent parameter is the ratio between the light scattered by a particle at a certain wavelength to the total amount of light scattered and absorbed. The single scattering albedo resembles in shape the original reflectance spectra and varies between 0 and 1. The single scattering albedo can be derived either directly from the wavelength dependent complex index of refraction $n+ik$, where n is the refractive index and k is the extinction coefficient. First the absorption coefficient α is calculated from the dispersion relation $\alpha = 4\pi nk/\lambda$. For closely spaced particles the extinction efficiency becomes one ($Q_E = 1$), and $w = Q_S/Q_E$, the single scattering albedo, becomes equal to Q_S, the scattering efficiency. A simplified relation exists between Q_S and the volume absorption coefficient α (Hapke 1981, eq. 33) which can be employed to derive w from α through

$$Q_S = w = (1 + \alpha D_e)^{-1} \quad \text{with} \quad D_e = \frac{2}{3}\frac{1 - S_E}{1 - S_I}D. \tag{3.7}$$

The effective particle diameter D_e is explained in more detail in section 3.3.

Another option is the inversion of reflectance spectra measured in laboratory of compositionally controlled powders using equation 3.6 for the radiance coefficient. In laboratory, powdered samples are often measured relative to a pressed halon standard, which behaves approximately like a lambert surface (Weidner and Hsia 1981). Deviations from lambertian behavior of the halon standard are corrected. Hence reflectance spectra measured in laboratory can be described by the radiance coefficient which gives the reflectance of a medium relative to a lambert surface.

Direct measurements of the wavelength-dependent complex index of refraction for mineral samples with controlled composition, within the varieties interesting for modeling of lunar regolith, are more limited than available reflectance spectra from mineral powders with controlled composition, particle size and observation geometry. To increase our options for mineral endmembers, the single scattering albedos for the model are derived from laboratory reflectance spectra. Nevertheless, available mineral extinction coefficient (k) spectra offer the opportunity to double check the derived single scattering albedos. Uncertainties in single particle phase function $p(g)$, in porosity, in mean particle size and multiple scattering H-function, lead to uncertainties for the derived single scattering albedos from laboratory reflectance measurements.

The radiance coefficient is not only depending on the single scattering behavior of particles described by w, but also on the single particle phase function and the porosity of the observed sample, both usually unmeasured parameters. The influence of those parameters on the inverted single scattering albedo is shown in Figure 3.2. Single scattering albedos, derived from inversion of reflectance measurements of the eight mineral endmembers, are displayed for three different phase functions and three different porosities (P=90%, 60%, 40%). The reflectance spectra, used as standard input for the model, from which single scattering albedos are derived are shown in Figure 3.3. To derive the wavelength-dependent single scattering albedo w from radiance coefficient measurements, w is varied between 1 and 0 for the wavelength λ measured in laboratory to find the single scattering albedo for which the calculated radiance coefficient best fits the measured laboratory radiance coefficient.

Grains that scatter light into non-uniform angular patterns are called non-isotropic scatterers. This is relevant for all mineral grains we consider and thus their single particle phase functions, which describe this angular pattern, differ from an isotropic phase function. Mustard and Pieters (1989) derived indirect single particle phase functions for several mineral species, assuming that those functions can be modeled as two-term Legendre polynomials

$$P(g) = 1 + b\cos(g) + c(1.5\cos^2(g) - 0.5) \qquad (3.8)$$

with the constant b describing forward and backward scattering and c describing scattering to the sides. Several single particle phase functions are displayed in Figure 3.1 for pyroxene, plagioclase, olivine and magnetite, with b and c being an average for the different minerals of each species measured in this study. In contrast to isotropic scatterers all mineral samples show strong forward scattering. The phase function of magnetite is used for ilmenite and agglutinates, for they exhibit similar low-albedo spectra. For the final calculation of single scattering albedos for model input, the average phase function for forward scattering particles ($b = -0.4, c = 0.25$) and a porosity of 60 % is assumed. The porosity of a sample can be calculated by subtracting the ratio of the bulk density of a sample and its specific gravity from one (Heiken et al. 1991, p. 492):

$$P = 1 - \frac{\rho}{SG}. \qquad (3.9)$$

With a typical specific lunar gravity of about 3 (ratio to water density) and an average lower bulk density of 1.2 g/cm^3 (Heiken et al. 1991, p. 497),representative of the uppermost regolith surface, we derive a porosity of about 60 % for the Moon. The porosity of lunar soils decreases fast with depth, but in the uppermost millimeters of the lunar surface observed with remote sensing in the near-infrared, we must consider the maximum known porosity of lunar regolith. For the inversion of laboratory reflectance spectra we also assume a porosity of 60 %. This is based on measurements published by Shepard and Helfenstein (2007). For testing the reliability of Hapke's model they prepared controlled samples, measured reflectance spectra of these samples, and provided them to researchers for retrieval of the parameters of Hapke's model. Bulk porosities were calculated for all
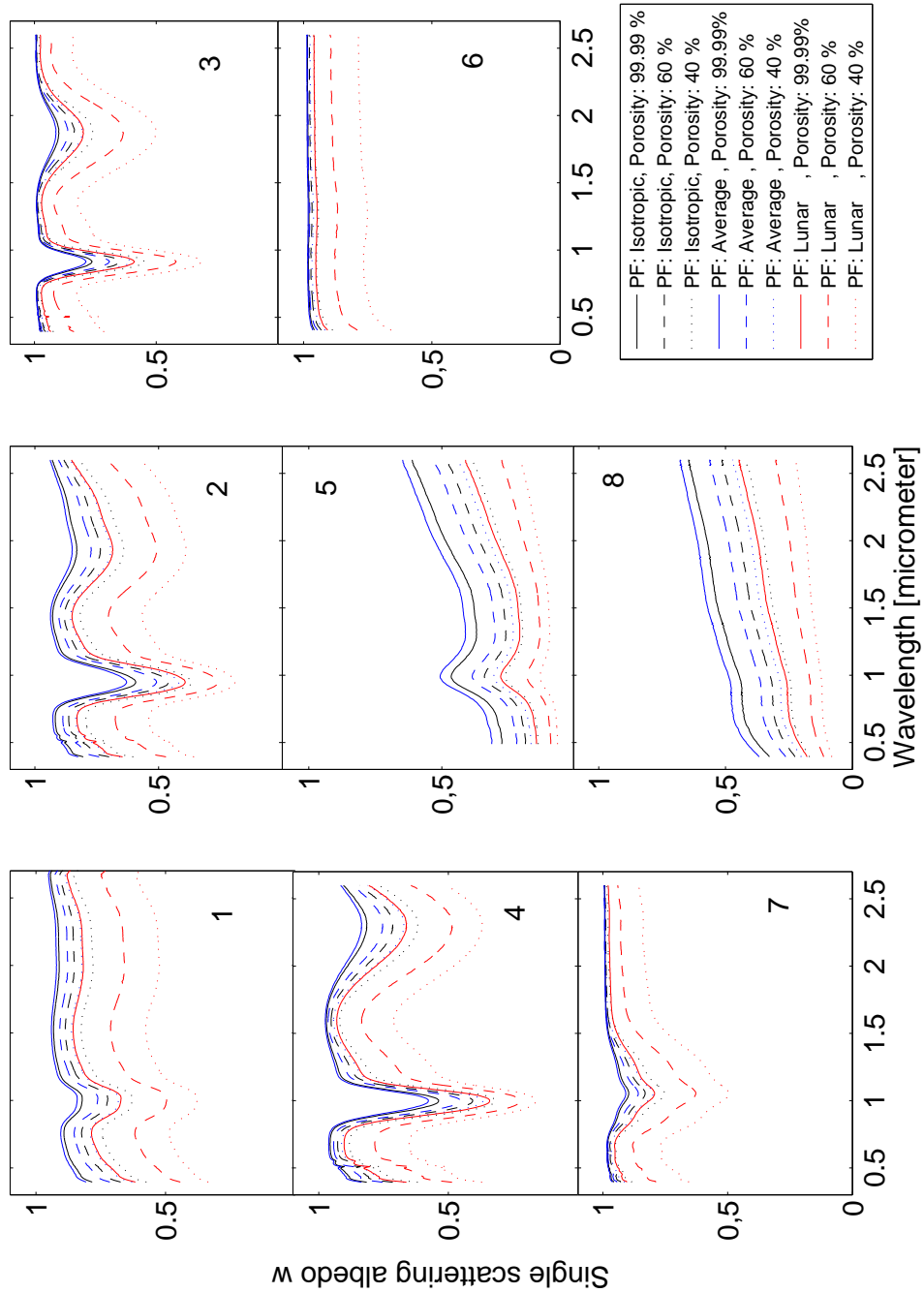
Figure 3.2: Single scattering albedos derived for eight endmember spectra. The influence of different porosities and single particle phase functions on the derived single scattering albedos is displayed. The single scattering albedos for an average forward scattering single particle phase function and 60 % porosity are used as input endmembers for the model. All observations were conducted under standart observing conditions.
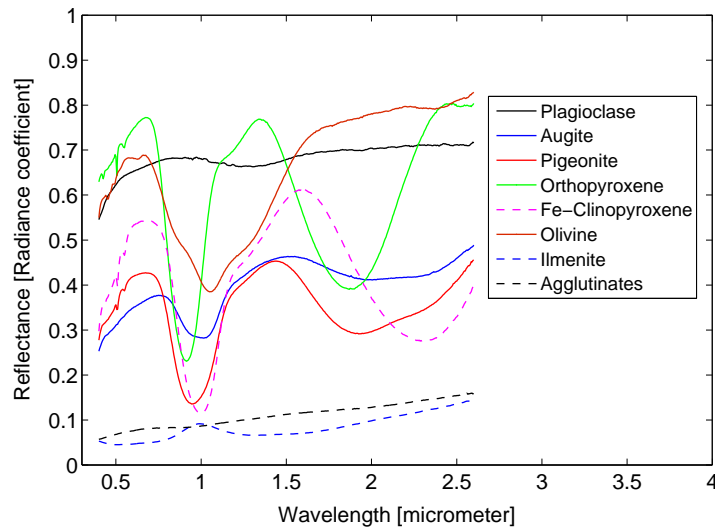
Figure 3.3: Selected endmember spectra for modeling of SIR-1 absolute spectra. A plagioclase close to anorthite, four pyroxene spectra representing the variation of pyroxene observed in lunar samples (Heiken et al. 1991, Taylor et al. 2001), an olivine spectrum, an ilmenite spectrum, and a spectrum of agglutinates separated from a soil from the Luna 20 unmanned sample return mission.

samples. The sample porosities ranged from 45 % to 93 %. The bulk porosity average of samples with particle sizes larger than 20 micrometer is about 60 %. The sample preparation procedure of filling a sample dish and tapping it so the grains settle (Mustard and Pieters 1989, Shepard and Helfenstein 2007), probably leads to similar average porosities. The effect of sample porosity was only recently included into Hapke's theory (Hapke 2008) and was not regularly measured together with the available reflectance spectra. Nevertheless, the application of porosity is necessary, because for high albedo reflectance spectra of olivine and plagioclase, no single scattering albedos within the allowed range between zero and one could be retrieved.

Laboratory spectra are taken with known viewing geometry and only samples with given lower and upper limits for the grain sizes are considered as possible endmembers. The breaking of rock or mineral samples does produce a powder with a grain size distribution. This physical truth is simplified by assuming a mean or an effective grain size to represent the whole sample. The derived single scattering albedos are particle size dependent. With equation 3.7 we can convert the single scattering albedo to the absorption coefficient. The absorption coefficient is size-independent. However, to determine the effective particle diameter D_e, we have to make an assumption about the mean particle size of the sample. Usually the center of the grain size interval of the sample is taken. After retrieving the single scattering albedo w for our selected spectral endmembers, we come now to the representation of space weathering within our model.
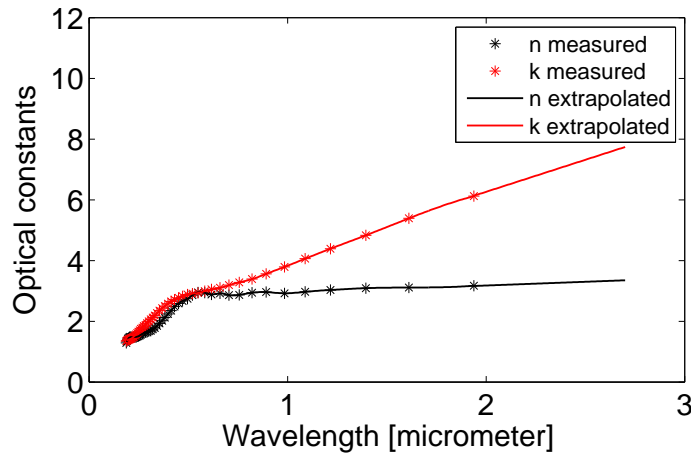
Figure 3.4: Measured refractive index *n* and extinction coefficient *k* for iron (Johnson and Cristy 1974). The measurements are linear extrapolated up to 2.7 micrometer.

3.2   The absorption coefficient of small iron particles within a transparent host medium

Small iron particles are accepted as the main agent of space weathering (see section 1.3.2). In Hapke's paper "Space weathering from Mercury to the asteroid belt" (Hapke 2001) an approach to calculate the absorption coefficient of a transparent particle with small iron inclusions is presented. Following the Hapke paper we can calculate the absorption coefficient of iron particles within a host medium from the optical constants of iron and the optical constants of the host medium. Optical constants for iron, *n* and *k* are published by Johnson and Cristy (1974). These measurements are linearly extrapolated up to 2.7 micrometer (Figure 3.4) to cover the whole wavelength range used within our model. The volume fraction ϕ of iron within the host medium is used to vary the amount of space weathering. This factor is usually much smaller than 1 (e.g. 0.001). Different starting values for this parameter were tested with the model to evaluate its influence on the model results. At first, the contribution of the small iron particles to the absorption coefficient of the whole grain is calculated through

$$\alpha_{Fe} = \frac{36\pi}{\lambda}\phi z. \tag{3.10}$$

The parameter z depends on the refractive index n_h of the host medium and on the optical constants n_{Fe} and k_{Fe} of the iron particles:

$$z = \frac{n_h^3 n_{Fe} k_{Fe}}{(n_{Fe}^2 - k_{Fe}^2 + 2n_h^2)^2 + (2n_{Fe}k_{Fe})^2}. \tag{3.11}$$

The refractory index for plagioclase, pyroxene, and olivine is taken from Hiroi and Pieters (1994). For ilmenite a value of 2.7 from the book "Optical Mineralogy-The nonopaque minerals" (Phillips and Griffen 1980) is assumed to be constant over the wavelength
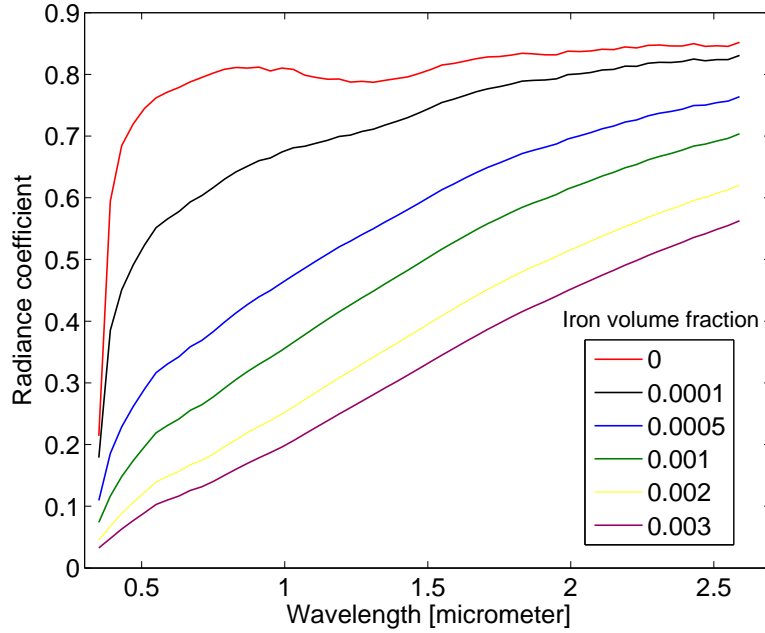
Figure 3.5: These reflectance spectra demonstrate the effect of space weathering on a pure pla-
gioclase spectrum for standard observing geometry and 60 micrometer particle size. The degree
of space weathering is controlled through the "Iron volume fraction", the amount of small iron
particles known to be the agent of space weathering.

regime modeled. For agglutinates a typical refractive index for glass (1.6) is employed
and also assumed constant over the modeled wavelength regime, because agglutinates
contain mainly glasses.

3.3   Space weathering of pure mineral components

The effect of adding small iron particles to a plagioclase spectrum is demonstrated in Fig-
ure 3.5. Increasing the value of the "Iron volume fraction" decreases the overall albedo
and introduces a strong red slope.

To simulate the space weathering effect, we apply the absorption contribution of the small
iron particles to the host medium. First we have to calculate the absorption coefficient of
the pure mineral from the single scattering albedo derived from inversion of a laboratory
reflectance spectrum as described in section 3.1. For this calculation we need

$$S_E = \frac{(n-1)^2}{(n+1)^2} + 0.05 \tag{3.12}$$

for the Fresnel reflection coefficient of light coming from outside and being reflected at
the surface of the particle and

$$S_I = 1 - \frac{4}{n(n+1)^2} \tag{3.13}$$

for the Fresnel reflection coefficient of internally scattered light. The absorption coefficient is then calculated from the single scattering albedo through

$$\alpha = \frac{1}{D} ln\left[S_I + \frac{(1 - S_E)(1 - S_I)}{w - S_E} \right], \tag{3.14}$$

where D is the mean photon path length. Another way to calculate the absorption coefficient α from single scattering albedo w is

$$Q_S = (1 + \alpha D_e)^{-1} \quad \text{with} \quad D_e = \frac{2}{3} \frac{1 - S_E}{1 - S_I} D, \tag{3.15}$$

where "D_e is an effective particle diameter of the order of twice the mean particle size" (Hapke 1981). Q_S is the scattering efficiency and the single scattering albedo is the ratio of Q_S and Q_E, the extinction efficiency. For closely spaced particles Q_E becomes 1 so that $w = Q_S$.

Now we simulate the space weathering effect by adding the absorption coefficient of small iron particles within the host medium α_{Fe} to the absorption coefficient of the host medium α_{hm}:

$$\alpha_{sw} = \alpha_{hm} + \alpha_{Fe}. \tag{3.16}$$

The amount of iron and therefore the magnitude of the space weathering effect can be controlled by the volume fraction of iron which is represented by the parameter ϕ. From the space weathered absorption coefficient we now calculate the single scattering albedo of the space weathered material which is used to compose the intimate mixture using equation 3.15:

$$w_{sw} = (1 + \alpha_{sw} D_e)^{-1}. \tag{3.17}$$

3.4 Composing an intimate mixture

After we derived the single scattering albedos of the space weathered minerals we calculate the space weathered single scattering albedo of the intimate mixture. Each of the n mineral components is entering the mixture according to mass fraction M, specific gravity ρ, particle size d and space weathered single scattering albedo w_{sw}.

$$w_{im} = \sum_{i=1}^{n} \frac{M(i)}{\rho(i)d(i)} w_{sw}(i) \tag{3.18}$$

The specific gravity values used for the current model are displayed in Table 3.2.
The single scattering albedo of the intimate mixture is inserted into the radiance coefficient equation 3.6 for calculation of the model spectrum.

Table 3.2: Specific gravities for the current model endmembers

Component	Specific gravity	Source
Plagioclase	2.729	Hiroi and Pieters (1994)
Pyroxene	3.425	Hiroi and Pieters (1994)
Olivine	3.461	Hiroi and Pieters (1994)
Ilmenite	4.79	Phillips and Griffen (1980)
Agglutinate	2.4	common value for glasses

3.5   Modeling of spectra

The parameters for plagioclase, pyroxene, olivine, ilmenite and agglutinate content as well as particle size, volume fraction of iron, single particle phase function and porosity are varied and the resulting radiance coefficient spectrum is modeled to fit the measured radiance coefficient spectrum with the least-square IDL routines "mpfit.pro" and "mp-fitfun.pro" written by Craig B. Markwardt. The fitting is performed with a Levenberg-Marquardt least-square fit. The input to the routine is provided by the program "MODEL_-SIR_SPECTRA.pro" and the function modeled is "MODEL_INTIMATE_MIXTURE.pro", which composes the intimate mixture and calculates the radiance coefficient, providing the model for the fit. Twelf free parameters enter into the model. Together with the start values of these parameters, upper and lower limits are given which increases the reliability of the fit. The twelfe free parameters for an absolute spectrum of a eight component mixture are:

1. Effective particle size of the sample

2. Plagioclase mass fraction (1st component)

3. Mg-Clinopyroxene (Augite) mass fraction (2nd component)

4. Pigeonite mass fraction (3rd component)

5. Orthopyroxene mass fraction (4th component)

6. Fe-Clinopyroxene mass fraction (5thcomponent)

7. Olivine mass fraction (6th component)

8. Ilmenite mass fraction (7th component)

9. Agglutinate mass fraction (8. component)

10. Volume fraction of small iron particles: ϕ

11. Porosity of the sample: P

12. Value of the single particle phase function at standard geometry $p(g)$ with $g = 30°$

The model starts with an educated guess for the relative abundances of the mixture components in common lunar materials as known from the Apollo sample suit. A common grain size for all components of the sampling site is assumed. This is a simplification because there are known differences in the comminution of the main lunar minerals (Cintala and Hoerz 1992). Basically plagioclase is more easily broken and thus enriched in the smaller size fractions of the regolith. Hence even if the minerals were exposed to the same impact flux at a certain site the grain size distribution must not necessarily agree. This effect is very small and is neglected considering the anyway large uncertainties in grain size. So the same effective grain size is assumed for all the components. From the mineral mass fractions we get the major information about the mineralogical composition of the site. The output is influenced by the particle size, the volume fraction of iron the porosity and the value of the single particle phase function. Furthermore start parameters for the mass fractions can influence the results of the modeling, and an influence of the step size with which the parameters are varied during the fitting procedure was observed. Hence, entering different sets of start parameters, lower and upper limits, and step sizes leads to different results, with still the model perfectly fitting the available data. There are two possible reasons. Only a local minimum is found with the least square method or several sets of parameters satisfy the measurement. This could be either due to noise resulting in large measurement errors which give larger tolerance for possible solutions, or due to the fact that the most prominent absorption feature at 1 micrometer is not completely within the measured wavelength interval and thus the problem might not be sufficiently determined.

Non-unique solution are observed. Especially the olivine and ilmenite content exhibits large variations with the input start parameters, indicating that the resulting mass fractions may have large uncertainties. The broad absorption of olivine at 1 micrometer is not completely within our wavelength range. Unlike the pyroxenes, which exhibit another absorption at 2 micrometer which gives additional constraints for the modeling, olivine has no second absorption at two micrometer. Hence, with only half of the broad absorption band considered (SIR-1 measurements reach from 0.9 to 2.4 micrometer) the model makes use of olivine to model a part of the red slope produced by space weathering. To understand the problem, we can dissect the influence a change in parameters can have on a modeled spectrum. To increase the overall albedo of a hypothetical spectrum we can: add more of a high albedo mineral like plagioclase, decrease the grain size, decrease the porosity, or increase the phase function value. All these variations will have the same effect, a brightening of the modeled spectrum. For decreasing the overall albedo we can: add a low albedo mineral such as ilmenite or increase the amount of agglutinates which also exhibit a low albedo. Furthermore we can increase the porosity, the particle size, or lower the phase function value. Absorption bands which contain mostly the compositional information of the pyroxene and olivine content give stronger constraints to the model because they are distinctive for a certain mineral and can thus be identified. Through the space weathering the absorption bands get distorted because the effect increases with wavelength between 1 and 2 micrometer according to the absorbing characteristics of small iron particles. By making educated guesses, backed by findings from Apollo samples, on the start values and the upper and lower limits we can decrease the number of possible solutions. Systematic analysis of the influence of porosity, phase

73

function and grain size, have shown that changes in these three parameters can counter-balance each other, thereby leaving the mineral fractions relative unaffected. Also it has shown that olivine tends to mimic the influence of space weathering. By using the short wavelength Clementine filters we can put additional constraints on the short wavelength side of the olivine band. But with the low spectral resolution of Clementine UVVIS this is not sufficient to completely overcome the problems of non-unique solutions.

3.6   Constraints on endmember spectra

An endmember is a pure mineral of a certain composition that represents a certain mineral group within a mixture. As described in section 1.4, the four major lunar minerals plagioclase, pyroxene, olivine and ilmenite can occur in a large variety of compositions that can influence their general albedo, position, strength and form of the absorption bands. Minerals of the pyroxene group show by far the strongest variability of absorption bands with composition and have the largest impact on the absorption bands of lunar reflectance spectra, because they represent the second-most abundant mineral phase in lunar soils after plagioclases which usually have no strong absorption features. In laboratory analysis of lunar soils Taylor et al. (2001) subdivided the pyroxenes into four subgroups to dissolve the influence of different pyroxene species. Pyroxenes found in the samples where sorted into orthopyroxenes, pigeonites, Mg-clinopyroxens and Fe-clinopyroxenes which represent different positions in the quadrilateral diagram of pyroxenes. Denevi et al. (2008) tested this hypothesis for an Apollo 12 soil sample. They compared an average single scattering albedo from 127 pyroxene compositions observed in a "grain mount" of grains with sizes between 90 and 150 micrometer of that sample, with the average single scattering albedo of the four Taylor subgroups, weighted with the model percentages derived in Taylor's analysis of the same sample 12001 and found them to be consistent. On this kind of classification our choice of pyroxene endmembers is based. Spectra of the choosen mineral endmembers for the current model were displayed in Figure 3.3. Details for those endmembers are given in Table 3.3.

Table 3.3: In this table details for the current endmember spectra are displayed. Mineral name, specific gravity, refractive index and the names of the RELAB directories in which the files with the measured reflectance spectra can be found are given. Where known the composition is given. All files are derived from the RELAB data base (http://www.planetary.brown.edu/relabdata/data/)and where selected so that they represent the major minerals on the lunar surface as seen within Apollo samples. References for the specific gravity values are given in Table 3.2. The refractive index values are taken from the same sources.

Endmember	Name	Composition	Specific gravity	Refractive index	File source for spectra
Plagioclase	Bytownite	SiO_2 53.67 %, Al_2O_3 29.11 %, CaO 12.04 %, Na_2O 4.64 %	2.729	$1.4657 + \frac{0.056290}{\lambda}$	RELAB: eac/pl/capl43.txt
Pyroxene 1	Augit	SiO_2 51.82 %, FeO 10.46 %, MgO 16.04 %, CaO 18 %	3.425	$1.5493 + \frac{0.066398}{\lambda}$	RELAB: eac/pp/c1pp50.txt
Pyroxene 2	Pigeonit	Wo10 En63 Fs27	3.425	#	RELAB: cmp/dl/c1dl10a.txt
Pyroxene 3	Orthopyroxene	En80 Fs20	3.425	#	RELAB: cmp/dl/c1dl27a2.txt
Pyroxene 4	Fe-Clinopyroxene	Wo20 En40 Fs40	3.425	#	RELAB: cmp/dl/c1dl51a.txt
Olivine	Fosterite	Fo80	3.461	#	RELAB: mdd/dd/c1dd38.txt
Ilmenite	Ilmenite	–	4.79	2.7	RELAB: msr/mr/camr05.txt
Agglutinates	–	–	2.4	1.6	RELAB: cmp/lu/c1lu07.txt

3.7 Constraints on iron volume fraction

A reddened slope, attenuated absorption bands, and general darkening are the aspects of space weathering most obvious in infrared reflectance spectra. At first, agglutinates were believed to cause these effects, but it is now accepted that small iron particles cause the majority of the spectral effects related to space weathering. Due to micrometeorite bombardment and solar wind irradiation, surface material is vaporized and sputtered. The small iron particles originate from fracturation during redisposition. They occur as inclusions in thin amorphous rims of 60 to 200 nm thickness (Keller and McKay 1997) around soil particles and as distributed inclusions within agglutinates where they originate from the rims of molten grains. Two terms are used when referring to the iron deposited by space weathering processes: submicroscopic metallic iron (SMFe) and nanophase metallic iron ($npFe^0$). Nanophase iron refers to the "nanometer-scale particles of metallic iron distributed in amorphous silicate" (Noble et al. 2007). Hapke (2001) emphasizes that "the optical effects of space weathering are caused by all of the Fe particles that are smaller than the wavelength, and not just by the nanometer-sized particles involved in the FMR" (Ferromagnetic Resonance). Following Mie theory, the absorption efficiency of a sphere with a metal-like refractive index decreases with $\frac{D}{\lambda}$ (Hapke 2001, eq.8), slower than the scattering efficiency which decreases with $(\frac{D}{\lambda})^4$, when the particle size D becomes smaller than $\frac{\lambda}{4}$ (Hapke 2001, Eq.9). When D is much smaller than λ, particles become almost perfect absorbers for their absorption efficiency is much higher than their scattering efficiency. In large particles the light does not reach the inner particle and thus they absorb less effectively than small particles where the whole particle is involved. Keller and Clemett (2001) found that the average size of nanophase iron in amorphous rims is 3 nanometers ranging from 2 to 10 nanometers and the average size of nanophase iron in agglutinates is 7 nanometers ranging from 2 to 25 nanometers. Morris (1980) investigated the amount of metallic iron for 79 lunar samples. Three sources were identified. Metallic iron can originate directly from meteorites (Fe_{MM}), from reduction of ferrous iron by fractionation during redisposition of impact vapors (Fe_{RM}) or being present already as a component in the source material (Fe_{SM}) from which the regolith formed. The amount of metallic iron produced by redisposition of impact vapors depends on the overall iron content FeO. Morris (1980) also noted that the particles of the Fe_{RM} metallic iron fraction are smaller than 33 nanometer, while those of the two other groups (Fe_{MM}, Fe_{SM}) are larger than 33 nanometer.

There are several suggestions how to incorporate the effect of small iron particles into models for lunar regolith (Hapke 2001, Nimura et al. 2008). Hapke suggested to quantify this effect using the volume fraction of iron within a sample. This iron is assumed to be distributed within transparent host grains comparable with the iron in agglutinates. Experiments with amorphous silica gel powders to produce lunar analogs with nanophase iron in four size fractions suggest that the different size fractions of nanophase iron have different effects on the spectra (Noble et al. 2007). Spectra of the artificially altered silica gel powders suggest that nanophase iron smaller than 10 nm mainly reddens the spectra in the visible, while particles larger than 40 nm lower the overall albedo without large effect on the continuum shape. Intermediate particles are also intermediate in the influence on the reflectance spectra. After comparing the shape of the four prepared size fractions with

sample spectra from Apollo 14,15 and 16, Noble et al. (2007) suggested an average size for lunar nanophase iron between 15 and 25 nm. This lies within the outer tail of the size distribution measured for some lunar agglutinates.

Reconsidering the assumed sizes for the three metallic iron sources (Fe_{RM}, Fe_{MM}, Fe_{SM}) in lunar soils proposed by Morris, we note that the iron reduced during recondensation of impact vapor probably is responsible for the red slope, and the remaining metallic iron is just reducing the overall albedo. In Figure 3.5 the effect of different iron volume fractions on plagioclase spectra was shown. For the less weathered spectra, that exhibit strong absorptions, and that are considered for modeling the iron volume fractions resides usually between 0 and 0.0005.

3.8   Constraints on mineral mass fractions

The major output of our model are the mass fractions of the five major lunar minerals derived from remotely sensed reflectance spectra. From Apollo samples we know the ranking of modal abundances valid for most of the analyzed lunar soil samples. Both mare and highland soils contain a large amount of glasses from impact and volcanic origin with clear majority of impact produced glasses. In the study of Taylor et al. (2001), impact glasses were combined under the label "agglutinitic glasses", because agglutinates make up over 90 percent of those glasses. Under the assumption that the Apollo soil samples represent the lunar surface, Table 3.4 gives an impression about the general variances that can be expected within the modeling results. Certainly, local extreme compositions are to be expected as can be seen in the volcanic glass beds found at the Apollo 17 site. Nevertheless, on large scales our compositions should reside between the composition of mare samples originating from deep strata and that of highland soils representing the composition of the upper crust.

Another obvious constraint on the mass fractions is based on the fact that model results of different spectra of the same active region, e.g., a small fresh crater, should exhibit approximately the same mineral composition. Little variations are to be expected from material ejected from a smaller and thus more uniform target. This does not apply to lava filled craters like Tsiolkovsky or Aitken, where two completely different mineralogies are present originating from different strata of the lunar crust and mantle. Also, the peaks of large craters exhibit material from deeper strata some kilometers below the surface and may thus vary in composition from the surrounding.

3.9   Influence of glasses

Two types of glasses are found in lunar soil samples. One of volcanic and one of impact origin. Glasses from impact origin are subdivided into impact glasses and agglutinates. The volcanic glasses originate from pyroclastic deposits and are thus localized in areas where pyroclastic events took place. During impacts, a part of the target is molten. Fast cooling can prohibit recrystallization and thus glass is formed.

Table 3.4: Modal abundance range of the main components of lunar soils for nine mare soils from Apollo 11, 12, 15 and 17 , and ten highland soils from Apollo 14 and 16. This table displays the range in which the abundances vary. The fraction of the different components vary substantial between the different samples. (Taylor et al. 2001, 2003)

Component	Mare soils	Highland soils
Agglutinitic glasses	30-70 %	30-70 %
Plagioclase	13-20 %	15-60 %
Pyroxene	4-33 %	1-20 %
Olivine	1-4 %	2-4 %
Ilmenite	1-12 %	0.1-2 %
Volcanic glasses	1-20 %	-
K-Phases	-	0-10 %

Agglutinates form when the Moon is permanently exposed to very small impacts due to its lack of an atmosphere. During micrometeorite bombardment, the projectile is vaporized and small amounts of the target are vaporized and molten due to high shock pressures. Small melt volumes rapidly quench and form agglutinates, glassy objects that contain small rock and mineral fragments, vesicles from the impact vapor and small iron particles. Technically agglutinates, are no pure glasses but a mixture of all soil components. Due to the relative domination of the agglutinate formation process, compared to pyroclastic eruptions and large impact glass bodies, the agglutinates dominate the glassy component of a soil. During soil evolution agglutinates accumulate until they make up a large portion of the soil. The modal abundances of minerals and glasses in several mare and highland soils were investigated through the Lunar Soil Characterization Consortium LSCC. The abundances of agglutinitic glasses range from 30 to 70 percent for both sample sets (Taylor et al. 2001, 2003). Agglutinates are homogeneous only in very small volumes of less than 10 μm (Basu et al. 2002). On large scales they are heterogeneous assemblages of small melt volumes that probably cooled too fast for large scale homogenization by mixing. To include an agglutinitic glass component into the model a reflectance spectrum of agglutinates separated from a Luna 20 soil is employed. Agglutinates exhibit no prominent absorption features in the reflectance spectra , thus their main influence is a general darkening and weak reddening of lunar soil spectra. However, glasses sometimes exhibit a broad absorption band at 1 micrometer.

3.10 Testing the model-Controlled intimate mixtures of known endmembers

Since the Apollo program, many laboratory studies were conducted to understand the systematics behind the spectral variation of reflectance spectra from planetary surfaces. Those spectra measured from pure minerals, mixtures, and altered mixtures provide an excellent test case to check the reliability of the model for controlled samples of known composition. The RELAB database is the largest source for this kind of data available

in public. Our test set comes from measurements conducted by E.A. Cloutis. No publications covering this mixture study could be found. Mixtures of four common major lunar minerals, plagioclase, pyroxene (augite and orthopyroxene), olivine and ilminite were prepared in various mass fractions as three and four component mixtures. This is unweathered material, thus the iron volume fraction was set zero for this modeling test. The reflectance spectra of the pure minerals, and of the mixtures are shown in Figure 3.6 and the source files and mixing ratios are given in Table 3.5. In Figure 3.7 and Figure 3.8 model results for the 6 mixtures, compared to the actual composition, are illustrated. Model results for the mineral fractions are displayed as bar diagrams. The first bar, labeled "L" represents the actual fractions in which the mixtures were prepared. Six model runs were conducted for each mixture to explore the effect of grain size, porosity and phase function value while keeping the mass fraction start values for the five possible minerals 20 percent each. Results are displayed in Figure 3.7.

- 1st run: grain size, porosity and phase function fixed

- 2nd run: grain size and porosity fixed

- 3rd run: grain size fixed

- 4th run: porosity and phase function fixed

- 5th run: phase function fixed

- 6th run: all parameters free

Another six model runs explore the effect of different mass fraction start values for the different minerals, while grain size, porosity and phase function vary free. The results of these six runs are displayed in Figure 3.8.

- Mass fraction start values for run a: 20 % for each of the five minerals

- Mass fraction start values for run b: 50 % olivine and 50% ilmenite

- Mass fraction start values for run c: 40 % plagioclase, 40 % augite, 10 % hyperstene, 10 % olivine

- Mass fraction start values for run d: 100 % plagioclase

- Mass fraction start values for run e: 100 % ilmenite

- Mass fraction start values for run f: 50 % augite and 50 % hypersthene

For most of the mixtures and runs the resulting mass fractions are within 5 % of the prepared mixtures. For ilmenite and plagioclase the deviation are within 10 % of the prepared mixtures. Both minerals exhibit a featureless straight spectrum between 1 and 2 micrometer, so that they can compensate for each others influence on the overall albedo. Hence the program was able to identify the right endmembers for each mixture, and reproduce the overall mass fraction trend. This gives confidence that we can apply this model for analysis of lunar spectra. Nevertheless, there are important differences between reflectance

Table 3.5: Test set for modeling with known endmembers. Endmembers and mixtures were originally prepared and measured by E.A. Cloutis. Spectra were retrieved from RELAB database from directory http://www.planetary.brown.edu/relabdata/data/eac/sc.

	Mineral endmembers	File
	PLG108 Plagioclase-Bytownite (45-90 micrometer)	c1sc37.txt
	PYX036 Clinopyroxene-Augite (45-90 micrometer)	c1sc35.txt
	PYX032 Orthopyroxene-Hypersthene (45-90 micrometer)	c1sc36.txt
	OLV003 Olivine-Forsterite (45-90 micrometer)	casc02.txt
	ILM101 Ilmenite (45-90 micrometer)	c1sc34.txt
Mixture Number	Mixtures of Minerals	File
1	**Standard lunar mix** 66.7 % PYX032, 26.7 % PLG108, 6.7 % ILM101	c1sc33.txt
2	**High ilmenite mix** 53.3 % PYX032, 21.3 % PLG108, 25.3 % ILM101	c1sc42.txt
3	**High olivine mix** 28.6 % PYX032, 57.1 OLV003, 11.4 % PLG108, 2.9 % ILM101	c1sc45.txt
4	**High orthopyroxene mix** 87.5 % PYX032, 11.4 % PLG108, 2.9 % ILM101	c1sc48.txt
5	**High plagioclase mix** 37 % PYX032, 59.3 % PLG108, 3.7 % ILM101	c1sc51.txt
6	**Standard lunar mix with clinopyroxene** 66.7 % PYX036, 26.7 % PLG108, 6.7 % ILM101	c1sc54.txt

spectra from unweathered mixtures of known endmembers, and lunar reflectance spectra. Space weathering, and the fact that there is no such thing as one pure endmember on an extended surface patch of about a kilometer complicate the analysis. Here, 8 free parameters were necessary, for lunar reflectance modeling additional 4 parameters (two additional pyroxenes, an agglutinate component and the iron volume fraction) will be introduced.
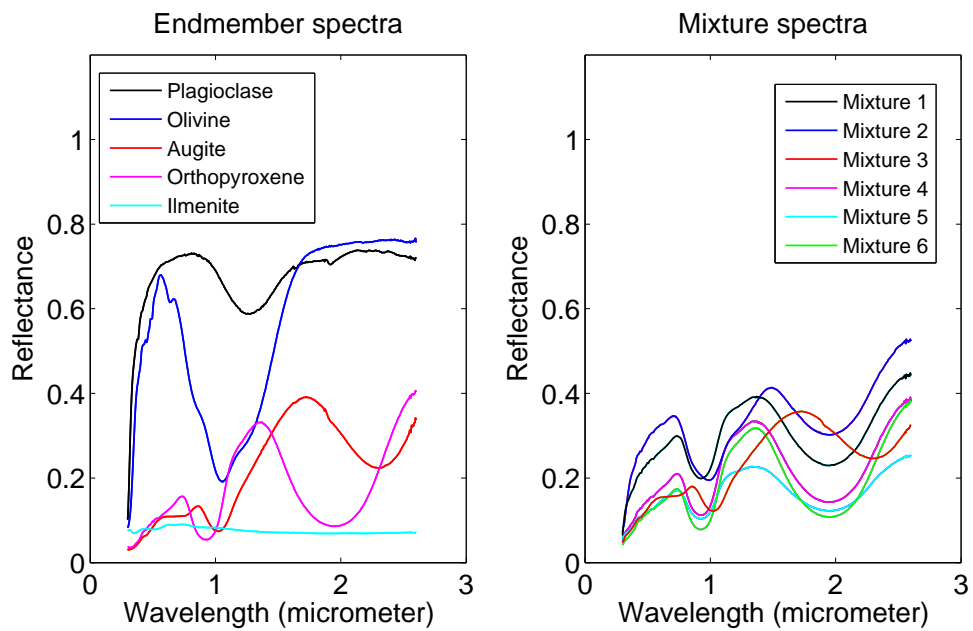
Figure 3.6: Reflectance spectra of endmembers (left panel) and mixtures (right panel) for the modeling test set.
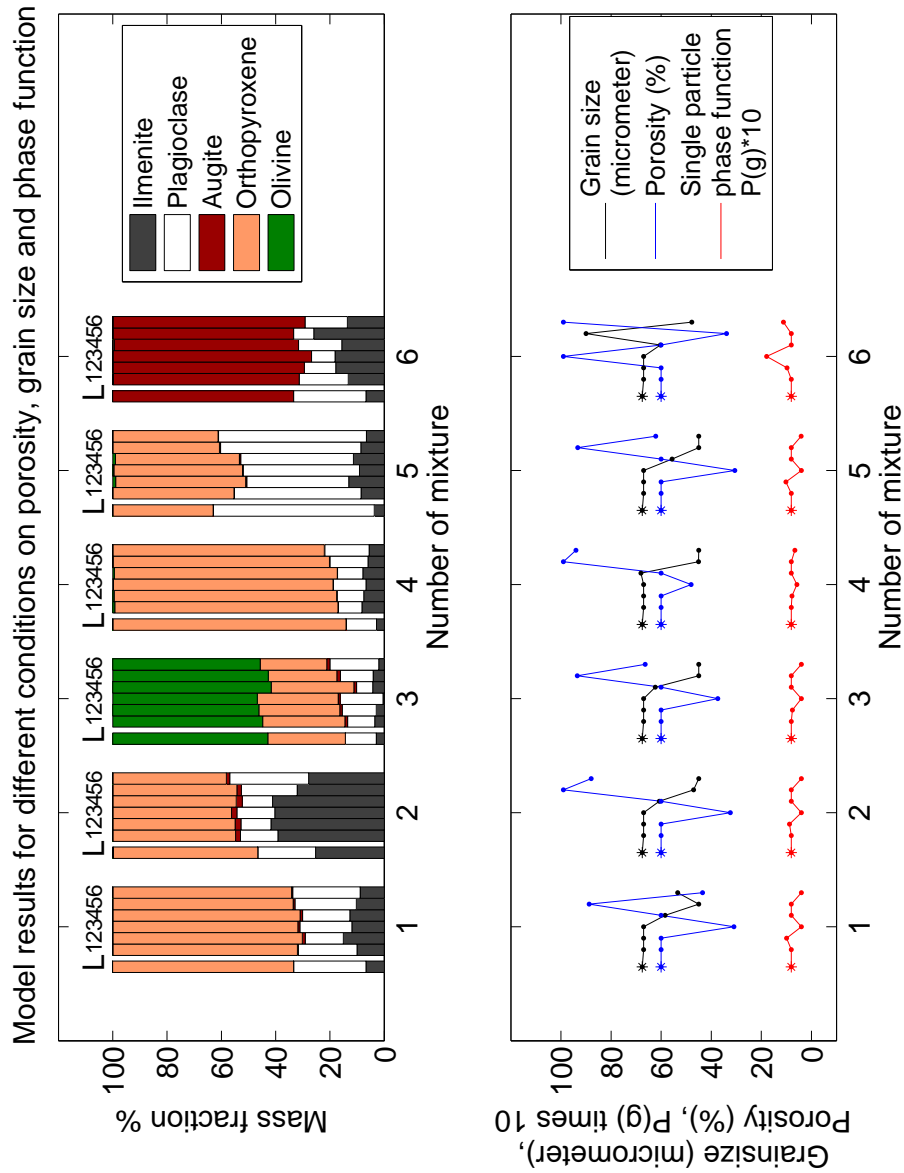
Figure 3.7: Upper panel: Results for the modeling of mixtures with known endmembers. The effects of grain size, porosity and single particle phase function are studied by fixing some parameters while the others vary. Each model run starts with 20 % for the mass fraction of each mineral. The different minerals are color coded. Six mixtures were modeled. For each mixture the results of six modeling runs of different constraints (labeled 1 to 6, see text) are shown next to the bar with the fractions in which the mixtures were prepared (first bar, labeled L). Lower panel: Grain size, porosity, and phase function value are displayed. Asterisks represent the real sample values, points represent the values of each modeling run. Circles indicate values that were hold during a run.
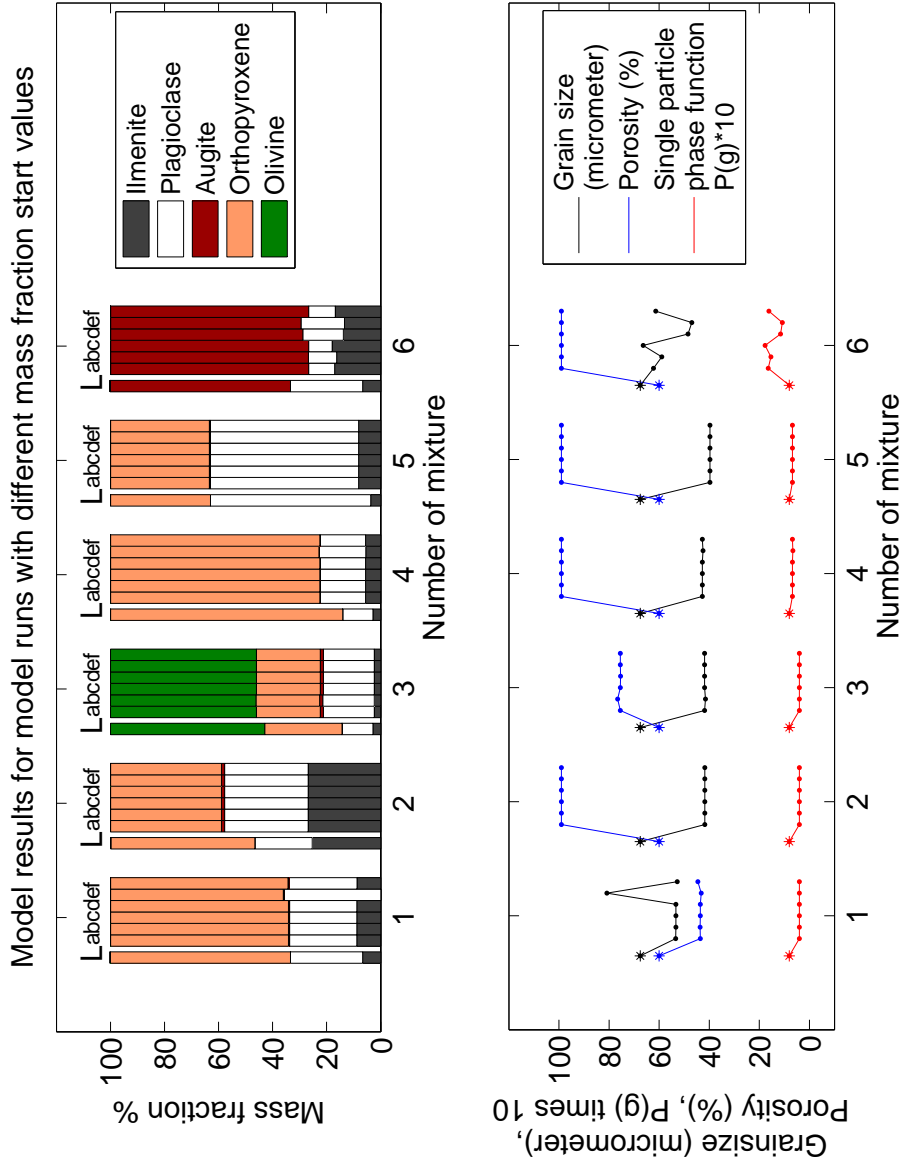
Figure 3.8: Upper panel: Results for the modeling of mixtures with known endmembers. The effect of different start values for the mineral mass fractions is demonstrated, and can be seen to have only minor influence. The different minerals are color coded. Six mixtures were modeled. For each mixture the results of six modeling runs of different constraints (labeled a to f, see text) are shown next to the bar with the fractions in which the mixtures were prepared (first bar, labeled L). Lower panel: Grain size, porosity, and phase function value are displayed. Asterisks represent the real sample values, points represent the values of each modeling run. The parameters grain size, porosity and phase function are mostly unaffected by the different mass fraction start values.

4 A Graphical User Interface for the regolith reflectance model

To make the modeling routines easily accessible, I developed a graphical user interface (GUI), for the regolith reflectance model that has been described in chapter 3. This widget program is based on the IDL programming language. A screen shot in Figure 4.1 gives an overview about the input an output options included in the graphical user interface. In the "Input" section the file with spectra that shall be modeled, as well as the errors of these spectra and the measured wavelengths have to be specified. In section "Mineral Endmembers" wavelength dependent single scattering albedos used as endmember input can be chosen. Those single scattering albedos are derived from laboratory reflectance spectra following the method described in Section 3.1. A "Standard start conditions" button offers the possibility to set reasonable start conditions. With "Display spectra for current values", spectra of hypothetical samples for chosen input parameters can be displayed, and the influence of the different components on the spectral shape can be explored. Measured spectra are modeled with the "Model spectrum" button. For each of the maximum 12 parameters a start value, upper and lower limits can be set. Each parameter can be fixed individually, either to an assumed value, or to zero, to exclude this parameter from the modeling. The "Output" table displays input and output values and the figure below displays the measured spectrum, the modeled spectrum and in this special case, also nine filter measurements of Clementine corresponding to the SIR-1 measurement modeled. In principle this modeling routine can be adopted for surfaces, with mineralogy different from the Moon, as for example asteroids or terrestrial planets as Mercury with simple surface mineralogy, by introducing new endmember single scattering albedos. A single grain size is employed for all components, thus if adopting this model for new tasks, the surface components should not exhibit large grain size variations among each other, as is usually the case for processes like impact comminuation that only act according to the physical properties of a surface, and are independent of the subtle chemical variations in the surface material.
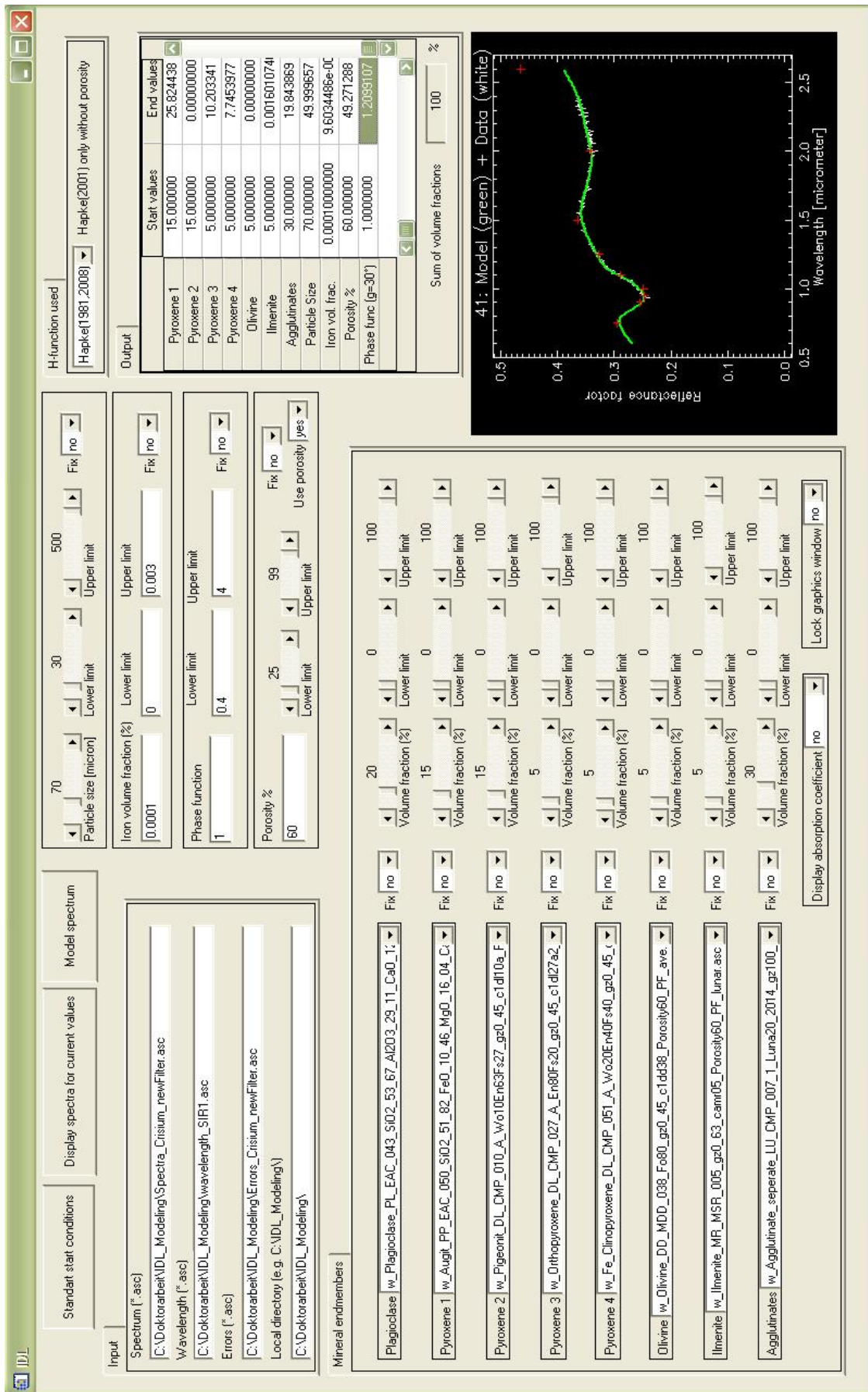
Figure 4.1: This graphical user interface provides easy access to the regolith reflectance model. With multiple options the influence of start parameters as well as upper and lower limits on the modeling results can be explored.

5 Systematic data analysis

In this chapter a routine, developed to extract spectra with strong mineral absorption features from the large database of reflectance spectra taken during the SIR-1 mission is introduced. During the SIR-1 mission a large set of about 28.6 million reflectance spectra was collected. Many of those spectra exhibit only weak to none mineral absorption bands. This suggests either a low mafic mineral content or a long exposure to space environment and thus strong space weathering. Spectra of younger sample areas with strong mineral features are most suitable for modeling. The influence of space weathering and agglutinate content which is increasing with surface exposure time is difficult to model, and not yet fully understood. In geologic younger (fresh) regions the mineralogy of the pristine material is more clearly detectable. Spectra from young regions that exhibit no absorption features have probably highly anorthositic compositions: for example the far-side lunar highlands and are not ideal for compositional modeling, since anorthosite rocks exhibit no strong absorption features and thus influence usually only the overall intensity in the near infrared, an effect also produced by decreasing grain size and porosity. On the other hand this less spectrally active areas with less complex composition, offers us the opportunity to study the effect of space weathering without the distraction of broad absorption features.

Due to large impacts and volcanic activities in the early history of the Moon we have many windows to other not primary anorthositic but more mafic compositions, providing evidence from greater depths below the lunar surface. Absorption bands at 1 and 2 micrometer due to pyroxene and olivine give good constrains for the modeling of composition in our wavelength region between 0.9 and 2.4 micrometer. Active spectra, spectra with strong absorption bands, mainly appear within young craters or at steep slopes where gravitationally slumping can expose unweathered surface materials. We can exploit these fresh craters and exposed slopes as probes into the mineralogy of the surrounding areas, where strong space weathering already complicates the identification of surface minerals. Most young craters found on the Moon are small in size due to the larger number of smaller projectiles. Because of the gaps between SIR-1 orbits not all small fresh craters were observed. A visual inspection of all spectra to find the orbit sections crossing fresh surfaces is too time consuming. Hence the necessity to develop an algorithm for automatic detection of significant spectra furthermore called "active" spectra. Spectral features are clearly highlighted in relative spectra, where a sample spectrum is divided by a nearby reference spectrum. As a result the visibility of the overall continuum and albedo is reduced and the absorption bands emphasized. Examples for relative spectra of an active spectral region are shown in Figure 5.3 in red and blue.

Spectra were selected by extensive automatic analysis of SIR-1 data with incident and phase angles lower than 70 degree and available and constant exposure times over one orbit. Furthermore sample spectra with mean digital number values of all 256 pixel lower than 5000 for 150 milliseconds exposure time and spectra with mean digital number values of all 256 pixel lower than 10000 for 251 milliseconds exposure time were excluded from further analysis due to larger instrumental noise. For each orbit, from all spectra fulfilling these conditions, one percent of the spectra were selected, according to their Active Spectra Indicator (ASI) value, a parameter invented to detect spectra with strong absorptions. Those spectra were integrated into small movies for each orbit. From the 1153 orbits for which spectral data was acquired, 1028 orbits had available files for exposure time. A further 182 orbits of those 1028 orbits had no measurements within the chosen incident and phase angle criterion and where thus also excluded. Other 25 orbits were excluded from automatic analysis due to a change of exposure time within the chosen orbit interval. Movies for 818 orbits with overall 100000 spectra fulfilling the criteria of the automatic selection procedure were produced. From those movies active spectra were selected manually. Approximately 10 percent of the automatically selected spectra, exhibited strong defined mineral absorptions bands, which resulted in the final selection of 9362 active spectra. The positions of those spectra are plotted in Figure 5.1 on top of a Clementine image of the lunar surface between 60 and minus 60 degree latitude. Thus by automatic and manual routines 0.000334 percent of all 28.6 million reflectance spectra were selected. These spectra will serve as a database for systematic modeling attempts. For those spectra the corresponding Clementine UVVIS/NIR data will be extracted were possible, to build an extensive data set of SIR-1 cross-calibrated absolute reflectance spectra with high spectral resolution.
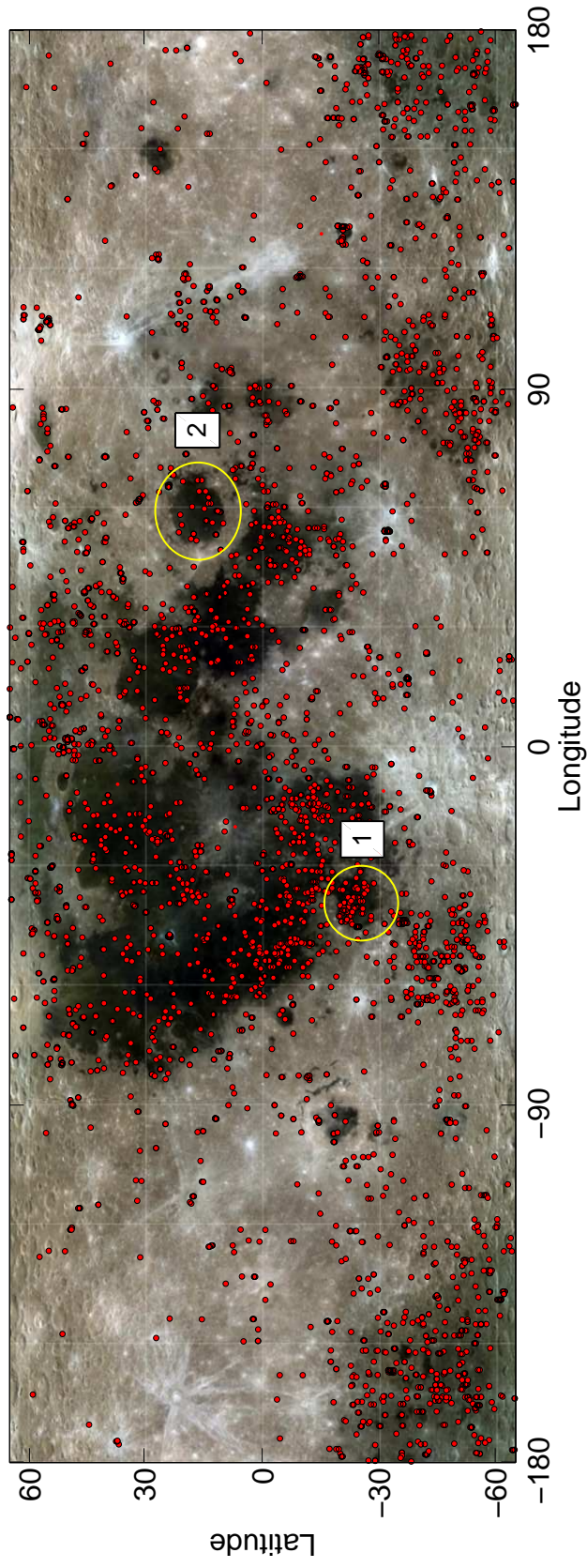
Figure 5.1: Each point in this Clementine image represents one of 9362 active spectra selected from SIR-1 measurements. The mafic pyroxene minerals, are the main cause for strong absorption features. Regions enriched in these minerals as the nearside mare, the farside South Pole Aitken basin (SPA), and Cryptomare are strongly represented in this selection. Mare Humorum (1) and Mare Crisium (2) are framed in yellow. Results from detailed analysis of these areas are presented in section 6.1.

Figure 5.2: Example for an active spectral region. Left panel: UVVIS image of small fresh crater (Lat: 24.1°, Long: 65.5°) with 7 km diameter at the wall of Eimmart crater (not in this image) together with one SIR-1 footprint. Right panel: Reflectance spectrum of this footprint in blue (Orbit 746 / Spectrum 13711) together with the corresponding spectrum extracted from Clementine UVVIS/NIR between 700 and 2600 nanometer in red.
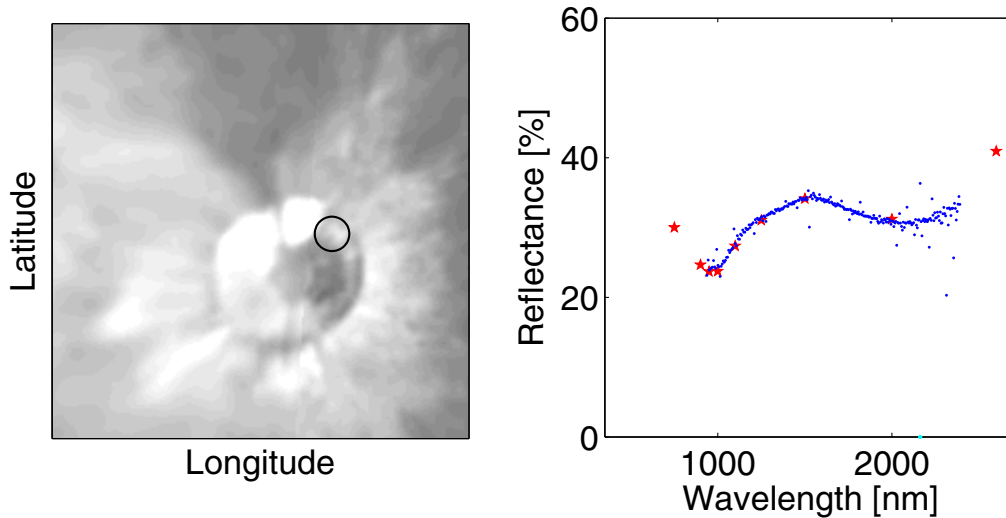
5.1   Identification of active spectra via automatic selection

In order to geologically identify significant "active" spectra, all spectra with an incident and phase angle lower than 70 degrees, and available complete SIR-1 data, were analyzed for systematic variation within their relative spectra. These relative spectra were scaled to unity at 1.5 micrometer to exclude intensity effects from the analysis. The scaling point at 1.5 micrometer is chosen because it represents the lunar continuum outside of strong absorptions, furthermore a Clementine NIR filter is available at that wavelength.

Two reference areas were chosen for calculation of two relative spectra for each sample spectrum. An example for those reference areas, are the red and blue orbit sections of orbit 746 in Figure 5.3. This method gives us the possibility to distinguish spectral features in the sample spectrum from features occurring within the reference spectra. Two reference spectra are calculated for each sample spectrum, each the median of fifty spectra. The first reference spectrum is a median of 50 spectra starting 250 spectra before the spacecraft observed the sample spectrum and the second reference is a median of 50 spectra starting from an area 200 spectra ahead of the sample spectrum. Due to different spacecraft altitudes, exposure times and ground track geometries, the real physical distance between reference area and sample area varies. For small surface features the reference areas are well outside the sampling area. Nevertheless, with this automatic detection procedure we
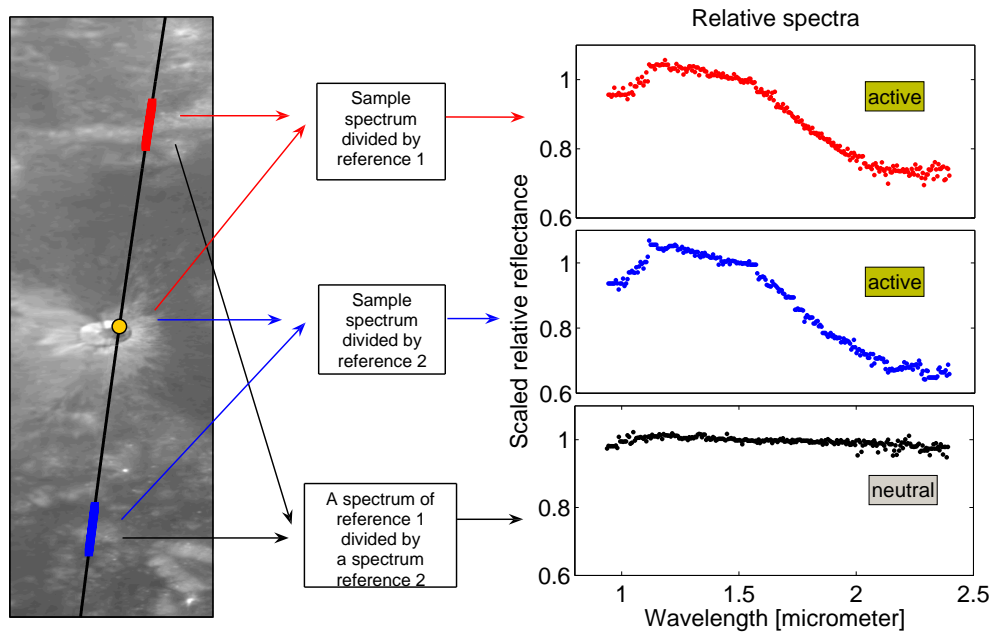
Figure 5.3: This image shows SIR-1 orbit 746 crossing the small bright crater of image 5.2. The displayed footprint (yellow circle) was selected with the automatic selection algorithm using relative spectra derived by dividing a sample spectrum by median spectra of two reference areas (Left panel: red,blue). The two active relative spectra exhibit strong absorptions (Right panel: red,blue). For comparison, a neutral relative spectrum (Right panel: black) derived by dividing two spectra from the different reference areas is shown. No strong absorptions are observed in this case.

might encounter problems in extended active spectral regions, when the two reference areas are not well outside the region anymore. This happens at large fresh craters, large fresh ejecta blankets and extended mare regions. While large fresh craters and ejecta blankets are rare, all mare regions exhibit absorption bands due to their mafic composition. In these regions reference areas close enough to the sampling area to exclude the temperature dependent variation in the instrument spectral sensitivity, but having none or only weak absorption features, are often unavailable. This makes this procedure less successful in those areas. Nevertheless, the strong spectral features of fresh craters are still easily recognizable in relative spectra with a highly weathered reference of the same composition. Only at mare/highland boundaries were the two references come from extremely differing surfaces this routine may miss some active spectral regions. From the identified spectra, those which show just a strong slope within our wavelength range (0.9-2.4 micrometer), but no prominent absorption features are excluded from further modeling. Differences in slope may relate to differences in age, but taken alone they do not offer compositional information. Absorption features masked by space weathering, become more evident in fresh materials. When only a strong slope, but no absorption bands are observed in a relative spectrum we can conclude that the respective sample region has no strong absorption features in the near infrared and might be rich in anorthosites, the major mineral component of the lunar crust.
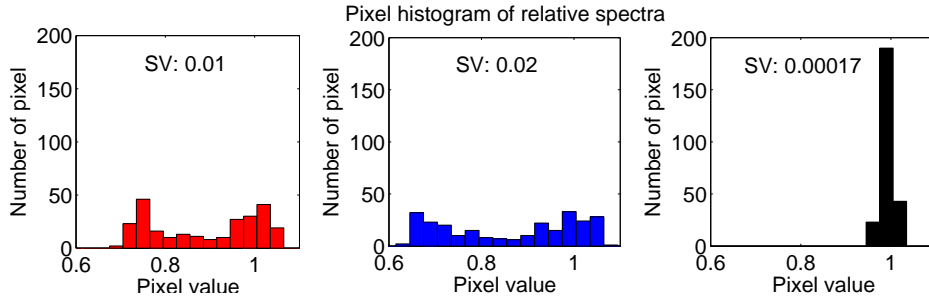
Figure 5.4: These graphs illustrate the sample variance (eq:5.1 of relative spectra. For each of the three scaled relative spectra in Figure 5.3 a distribution of the 256 pixel values is displayed. For a scaled relative spectrum without absorptions all pixel values are close to one and the distribution is narrow as in the lower panel. If, due to absorptions, the scaled relative spectrum deviates from a flat line, distribution becomes broader (upper and middle panel). The sample variance characterizes the statistical dispersion of sample values around the sample mean. For this example the sample variance of the relative spectra with absorptions is about two orders larger than that of the flat relative spectra. Thus it can be easily used to distinguish between the two cases.

For each sample spectrum S, we calculate two relative spectra R_1 and R_2, with two different references and scale them to unity at 1.5 micrometer as demonstrated in Figure 5.3. If the sample and the reference spectrum exhibit the same shape, the scaled relative spectrum shows a horizontal profile at 1. This indicates that sample area and reference area have usually the same large surface age and exhibit no different absorption features. Deviations from the horizontal profile are quantified by the sample variance, illustrated in Figure 5.4. To identify the interesting spectra we calculate the sample variances S_{V1} and S_{V2} for each of the two scaled relative spectra for all sample spectra along one orbit. The sample variance

$$S_V = \frac{1}{255} \sum_{i=1}^{256} (x_i - \overline{x})^2 \qquad (5.1)$$

where x_i is the scaled reflectance value of pixel i, and $\overline{x}$ is the mean of all pixel. The 256 measurements of one spectrum between 0.9 and 2.4 micrometer are thus treated as one measurement sample. The sample variance increases as the shape of the relative spectra deviates more and more from a straight line. This deviation can have several reasons for a single relative spectrum.

- Absorption features in the sample spectrum lead to absorption features in the relative spectra.

- Absorption features in the reference spectra lead to emission-like features in the relative spectra.

- Noise induced sample variance due to large detector temperature or detector saturation leads to many outliers that increase the sample variance even if no absorption bands or strong slopes are present.
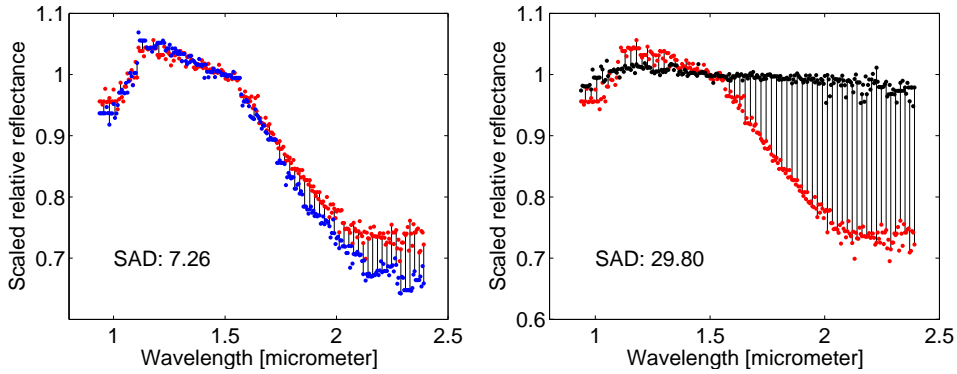
Figure 5.5: Illustration of the "Sum of the Absolute Differences" SAD (eq: 5.2) for pairs of relative spectra displayed in Figure 5.3. The larger the deviation of the two relative spectra, the larger the SAD parameter. After using the sample variance to find relative spectra deviating from a flat line, the SAD parameter helps to distinguish between deviation caused by absorption bands in the sample spectrum, and deviation caused by absorption bands in the reference spectrum.

- A combination of the above effects.

If the deviation is causes by the sample spectrum the sample variance should be the same for both scaled relative spectra, independent of the chosen reference area as can be seen in the middle peak of the upper panel of Figure 5.6. Small differences can be caused by measurement noise and minor spectral differences between the reference areas. Is the deviation caused by one reference spectrum the sample variances of the relative spectra differ strongly. For our selection we are only interested in variations of relative spectra caused by absorption features in the sample spectrum. To exclude the other effects we introduce also the Sum of the Absolute Differences (SAD) between the two relative spectra for each sample spectrum along an orbit. The SAD is illustrated in Figure 5.5 and calculated as

$$SAD = \sum_{i=1}^{256} |(R_1(i) - R_2(i))| \qquad (5.2)$$

where $R_1(i)$ and $R_2(i)$ are the pixel values of the two scaled relative spectra. Usually an absorption feature within a reference spectrum caused by fresh material in the reference area, will only be present in one of the two reference spectra. This will lead to a large Sum of the Absolute Differences of the two relative spectra, as they deviate strongly from each other. Using the sample variances of the two relative spectra, and the Sum of the Absolute Differences (SAD) we create an Active Spectra Indicator (ASI) for each sample spectrum along an orbit. First we scale the maximum/minimum distance of the sum of the absolute differences of the sample spectra along one orbit to the maximum/minimum distance of the sample variances of the second relative spectrum along the same orbit. Then we shift the whole SAD curve to the minimum of the sample variances curve of the second relative spectrum, thus making both parameters comparable by allowing them to vary within the same value range. After scaling, the Active Spectra Indicator (ASI) of a
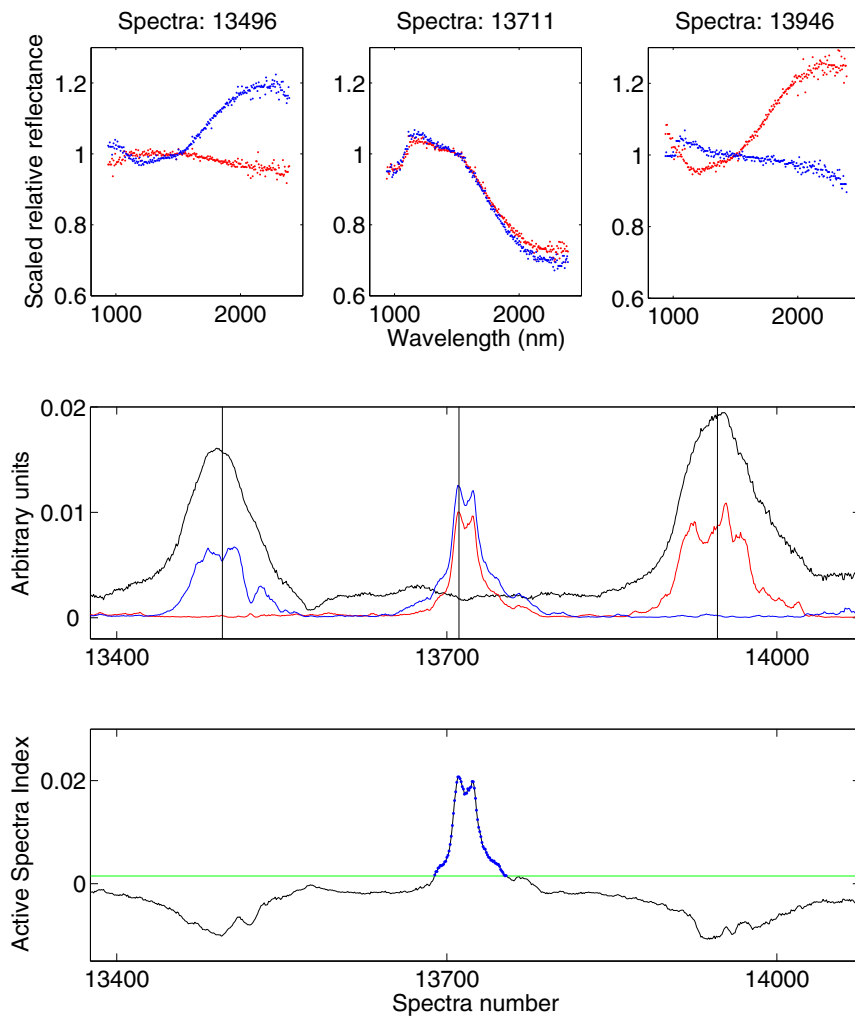
Figure 5.6: **Upper panel:** Example of scaled relative spectra at three locations around the small crater in Figure 5.3. The left and right panel show the scaled relative spectra for spectrum 13496 and 13946, north and south of the crater in the two reference areas. In the middle panel the scaled relative spectra of the selected footprint 13711 are displayed. If the spectral active region is in one of the reference areas (left and right panel), emission-like features appear in one of the relative spectra. Only in the middle panel both references did not exhibit absorption features and the active spectral region which caused the absorptions is clearly detected within the scaled relative spectra. **Middle panel:** The sample variances of scaled relative spectra (red and blue line) along this orbit interval as well as the scaled Sum of the Absolute Differences (SAD) of those spectra is displayed. Thin black vertical lines indicate the positions of those footprints for which scaled relative spectra are displayed in the upper panel. **Lower panel:** Active Spectra Index (ASI). The maximum in the ASI index clearly identifies the active spectral region. One percent of the footprints exhibit an ASI index above the horizontal green line. Those footprints (blue points) are enclosed in the movies for manual selection.

sample spectrum is the sum of the two sample variances curves subtracted by the Sum of the Absolute Differences (SAD) curve along one orbit.

$$ASI = (S_{V1} + S_{V2}) - SAD_{scaled} \tag{5.3}$$

Our research has shown that the ASI-parameter derived from the sum of the two sample variances and the scaled sum of the absolute differences is most sensitive to sample spectra exhibiting strong absorption features and slopes. In Figure 5.6 (lower panel) we display the ASI value for an orbit section around the active spectral region in Figure 5.3, a fresh crater at the rim of the older Eimmart crater. The peak in the ASI-curve clearly identifies the "active" spectra, which are used for further analysis and systematic modeling attempts.

6 Application of regolith reflectance model

6.1 Case study of Mare Humorum

Mare Humorum (Figure 6.1) is a basaltic lava deposit within the third inner ring (diameter 425 km) of the Humorum basin. The mare stretches 390 km in east/west and north/south direction and flooded over the first (210 km) and second (340 km) inner ring, which can be recognized by wrinkle ridges that formed in this area. In Clementine multispectral-imaging studies (Bussey and Spudis 2000), an FeO content of 16 to 20 wt% is inferred for the central mare deposits. The titanium amount was found to reside between 1 to 8 wt%, with higher TiO_2 content in the south-eastern part of the mare deposit. Nevertheless, these titanium values may have uncertainties of about 5 wt% (Jolliff et al. 2006, p.188). In a later paper Hackwill et al. (2006) identified 109 different mare units. Probably these are distinct lave flows defined by variing FeO and TiO_2 content and different crater densities. Thus we might expect some variations for SIR-1 spectra from different regions.

By automated search, 149 active spectra of SIR-1 footprints were identified within Mare Humorum. Of these spectra 125 could be successfully aligned with the Clementine images through matching of lightcurves. On average a shift of 0.25 degrees in longitude direction was necessary to align both datasets. The necessary shifts in latitude range from -0.2 to 0.2 degrees (see Figure 6.2, left lower panel). Five Clementine filters are well inside the SIR-1 wavelength range. Only SIR-1 cross-calibrated spectra for which the sum of the differences between the Clementine and the SIR-1 spectral points at the Clementine wavelengths 1, 1.1, 1.23, 1.5 and 2.0 micrometer is lower than 0.03, for radiance coefficient spectra with a range from 0 to 1, are modeled. This is necessary, because the Clementine filter measurements at 0.75, 0.9 and 0.95 micrometer will be combined with SIR-1 spectra to extend the wavelength range available for modeling. Originally the AMIE camera images should have been employed for this purpose, but due to a lack of calibrated AMIE images with controlled coordinates, the Clementine measurements give additional information at shorter wavelengths. Of the 125 aligned spectra, 30 meet the selection criterion. Setting the selection threshold for the sum of the differences between Clementine UVVIS/NIR and SIR-1 to 0.15 results in 114 spectra beeing selected. If no Clementine UVVIS/NEAR measurements are used all 125 spectra can be considered for modeling. The occasional differences between Clementine and SIR-1 spectra probably arise from differences in observing geometry. For now, we concentrate on the most reliable dataset: the combined spectra, with summed differences lower than 0.03 to enforce

a smooth transition between Clementine UVVIS and Sir-1 data at 0.95 micrometer.

A Clementine image of Mare Humorum with 30 spectra fulfilling the selection criteria is shown in Figure 6.1. The points represent the position but not the size of each footprint. The colors are coded according to the 2 micrometer value in relative spectra scaled to unity at 1.5 micrometer as seen in Figure 6.2 (left upper panel). This value gives a first indication of the strength of absorption bands for these spectra, but is also influenced by the overall slope of these relative spectra. Blue points represent spectra that exhibit stronger absorption at 2 micrometer and yellow points spectra with weaker but yet prominent absorption at this wavelength. The same color coding is used to display cross-calibrated SIR-1 spectra and Clementine measurements in Figure 6.2 (right upper and lower panel). Apparently the depth is not correlated with albedo, for there is no similar trend across scaled relative spectra. The cross-calibrated spectra in Figure 6.2 (right upper panel) were modeled together with three Clementine measurements at 0.75, 0.9 and 0.95 micrometer.

For each spectrum, best fit curves for three different iron volume fraction start parameter (0 ,0.0001 ,0.0002) were calculated. Experience has shown that the program itself is not able to reliably model the iron volume fraction. Because of that, a grid-search with different start values for iron volume fractions is preferred. All parameters were free within reasonable upper and lower borders, and standard start values of

- 20 % Plagioclase,

- 10 % Augite,

- 10 % Pigeonite,

- 5 % Orthopyroxene,

- 5 % Fe-Clinopyroxene,

- 5 % Olivine,

- 5 % Ilmenite

- 30 % Agglutinate

were used in each run. The reduced χ^2 parameter,

$$\chi^2 = \frac{1}{(N - F - 1)} \sum_{i=1}^{N} \frac{(r_S(i) - r_{mod}(i))^2}{err(i)^2}, \tag{6.1}$$

where r_S, are the measured reflectance values, r_{mod}, are the modeled values, err, are the errors, N is the number of measurements and F, the number of free parameters, is employed to estimate the quality of each fit. Model results with $\chi^2 > 1$ are excluded from further analysis. In Figure 6.3 and 6.4 the model results for the selected spectra of Mare Humorum are displayed. Each "accepted" model run is represented with a bar for the mineral mass fractions in the upper panel, where different colors indicate different minerals. In the lower panel the other free parameters, grain size, porosity, single particle phase
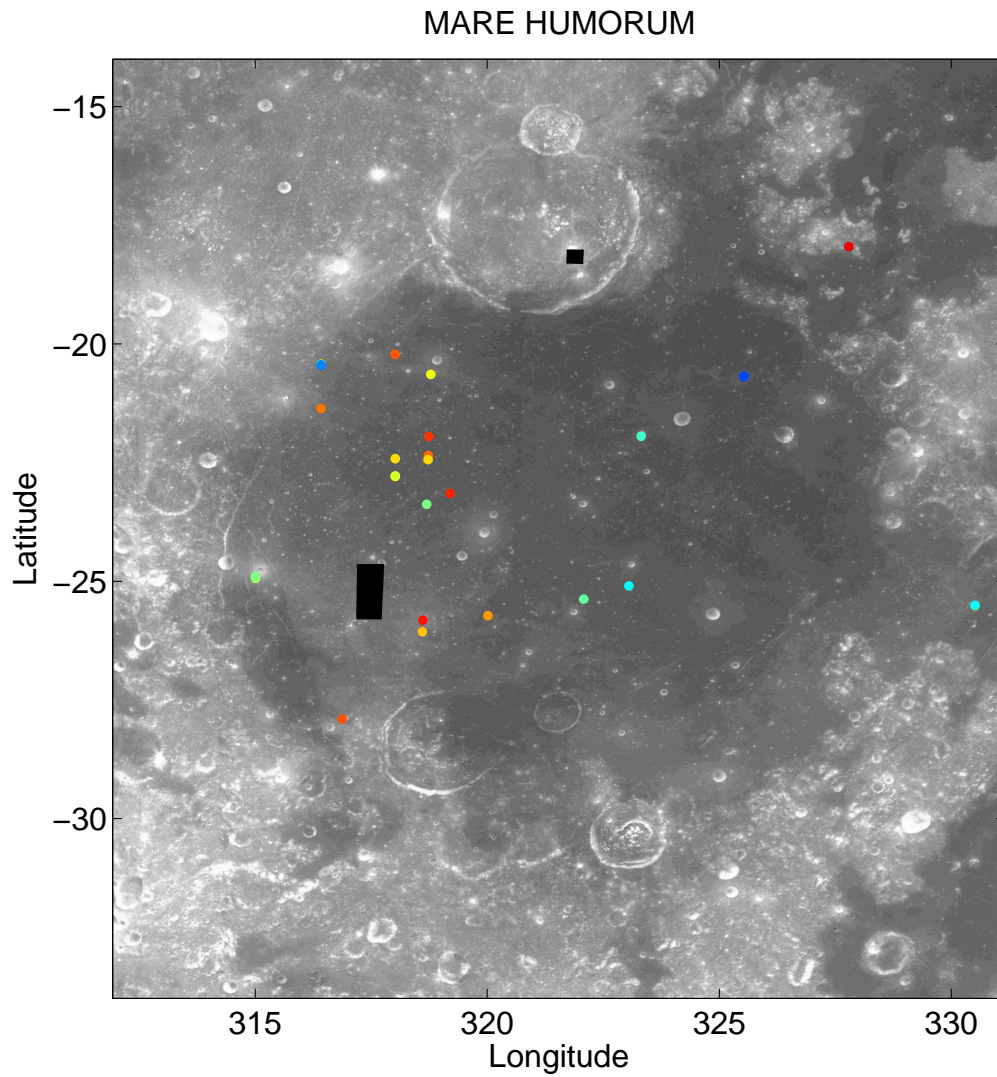
Figure 6.1: Clementine image of Mare Humorum. The colored dots represent the positions of the 30 selected footprints with strong absorption features. The colors are coded according to the 2 micrometer value in scaled relative spectra as seen in Figure 6.2.

function value, and iron volume fraction, are displayed for each model run. Two case spectra are shown in Figure 6.5 and 6.6. For modeling the first spectrum (Number 14), all start values produce fits with low χ^2 values and with only slightly varying composition. Instead, for the other spectrum (Number 13) a sufficient fit could only be derived for a starting value for the iron volume fraction of zero.

Derived modal abundances in Figure 6.5 and 6.5 reside mostly within the range known from Apollo samples. Nevertheless, for some runs the ilmenite (e.g. 4_1, 5_3, $7_{1,2}$, 11_2, 12_1, $15_{2,3}$, 16_1, $17_{1,2}$, 18_2, 26_2, 28_1, 29_2, $30_{2,3}$)[1] content seems clearly overestimated. Because of similar shape and albedo of the ilmenite end agglutinate endmember spectrum (see Figure 3.3), the routine is sometimes not able to disentangle the two influences and replaces agglutinates with ilmenite. A very good example is seen in spectrum 30, where the mineral composition of pyroxenes and plagioclases are relatively stable but the ilmenite content varies between 10 and 40 %. Thus, for now it is not possible to reliably model the ilmenite content. Rather for interpretation the ilmenite and agglutinates should be considered as a combined "dark" component.

Also grain size and iron volume fraction appear anticorrelated. The grain size decreases with increasing start values of iron volume fraction, probably balancing an albedo variation. With increasing iron volume fraction the albedo decreases, while with decreasing grain size the albedo increases. Here, it is clearly visible how the least-square routine uses the different parameters to adjust for different start values, so that still modeled spectra with an acceptable χ^2 values are produced. In principle the run exhibiting the lowest χ^2 should represent the best model fit.

The color-coding of spectra is done, so that the least weathered spectra with the strongest absorptions are coded as blue points in the model results (Figure 6.3, 6.4). For these spectra the iron volume fraction should be close to zero. Indeed, the model runs with 0.0001 and 0.0002 iron volume fraction had large χ^2 values indicating bad local minimum and were thus excluded for spectrum 12, 13, 27, and 28.

Another constraint on the model results is the fact that spectra of footprints observing the same object should yield comparable model results, as long as the object (e.g. small crater) is small enough to exclude large scale inhomogeneities. Most unweathered active spectra are found at small craters, simply because the crater frequency is larger for small sizes, i.e. more small impacts occur. Often the SIR-1 footprints are overlapping and thus measure a portion of the same surface. Major differences in footprint albedo occur for one object at inhomogeneities of the ejecta blanket, at crater walls due to local gravitational slumpings, or because of different effective observing geometries. During a hypothetical fly-over of a small crater we observe first the crater wall facing away from us, with a surface normal deviating 10 to 30 degrees from local flat surface normal, then the crater floor with a surface normal comparable to local flat surface normal and then the crater wall facing towards us, again with a surface normal deviating 10 to 30 degrees from local flat surface, but in opposite direction. Hence, footprint spectra observed during the same orbit

---

[1]Large numbers represent the spectrum number in Figure 6.3 and 6.4, while small numbers represent the model runs with different iron volume fraction start values (ϕ : 1=0, 2=0.0001, 3=0.0002)

over the same object can represent quite different illumination conditions. This effect is clearly visible in images with non-zero incident angle, where the crater walls facing the sun appear much brighter. Usually the exact local topography is unknown and often the effective observing geometry in small fresh craters varies strongly even within one footprint.

For several objects we have more than one footprint spectrum. In Table 6.1, where the coordinates of each footprint are displayed, spectra belonging to one object are grouped and marked with small consecutive numbers. Five objects were observed with more than one footprint within this selection. Usually less weathered spectra with strong absorptions (color-coding: blue) are found within the crater cavities, while the spectra appear more and more space weathered when crossing the ejecta blanket away from the crater (e.g. object 2, spectra 12, 13, 14).

The modeled pyroxene composition is richer in augite, and pigeonite, as expected from the relations found for lunar mare soil samples (Taylor et al. 2001). Agglutinates are on average 40 % or lower as for immature soils, which is not surprising for we intentionally selected fresh immature surfaces for our analysis. The fact that we are able to model almost all spectra with this low iron volume fraction start values (compare Figure 3.5) confirms again that the selected spectra originate from immature surface material. The large variations in ilmenite content between spectra of the same object and between model runs of one spectra indicate that the model is not able to reliably determine the ilmenite content of footprint spectra. The flat, low-albedo ilmenite spectrum provides a less informative basis for discrimination between ilminite content and other albedo lowering influences as agglutinate content, increase of grain size, increase of iron volume fraction, decrease of single particle phase function value, and increase of porosity. Therefore the problem is ill-posed. Furthermore, an unusually high olivine content is modeled for some spectra. Soil spectra as measured by Taylor et al. (2001) exhibit maximum olivine contents below 5 %, while some rock fragments, so called dunite, contain up to 93 % olivine (Ryder 1992). The developed model routine was able to determine correctly the presence and amount of olivine in the artificial mixture (see Figure 3.7), which gives confidence that this is also possible for lunar reflectance spectra. Although, many different mare units were identified within Mare Humorum (Hackwill et al. 2006), which would explain the variations between the different footprint spectra, the variability between model runs with different start condition for the same object, still leading to acceptable fitting of the spectrum (see Figure 6.5), the variability among footprint spectra derived from the same object indicates possible limitations for the modeling.
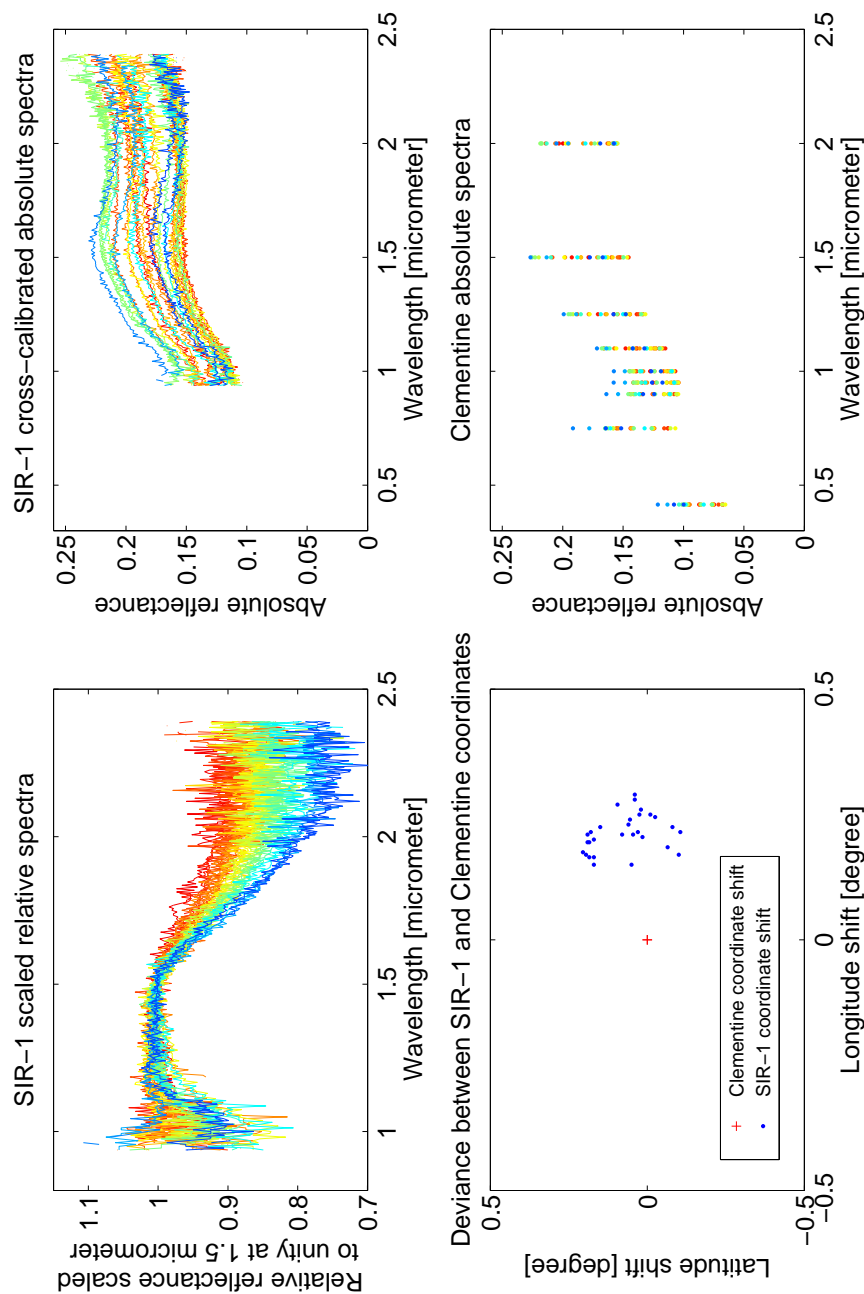
Figure 6.2: Active spectra selected for Mare Humorum. Spectra are color-coded according to the 2 micrometer value of scaled relative spectra. **Left upper panel:** relative spectra scaled to unity at 1.5 micrometer. **Right upper panel:** cross-calibrated absolute SIR–1 spectra (color-coding as in left upper panel). **Left lower panel:** Coordinate shifts necessary to align SIR–1 and Clementine UVVIS/NIR lighcurves. The red cross represents the Clementine coordinates. **Right lower panel:** Clementine measurements at the selected footprints. Note that this color-coding is applied in all plots concerning one object (see also Figure 6.3 and 6.4).

Table 6.1: Mare Humorum: Table with spectrum numbers and corresponding coordinates for identification of model results in Figures 6.3 and 6.4 with positions within Mare Humorum in Figure 6.1. The numbers in parentheses represents the indices of these spectra in the original selection of 125 active spectra, and indicate how many spectra were omitted because the agreement between SIR-1 and Clementine measurements was not sufficient for combined modeling. Small numbers indicate objects of which more than one footprint spectrum is available.

| Spec.	Lat	Long	Spec.	Lat	Long	Spec.	Lat	Long
1(1)	-27.9017	316.736	$12(35)_2$	-20.4475	316.238	$22(57)_4$	-24.8981	315.0062
			$13(36)_2$	-20.4338	316.2379			
$2(5)_1$	-25.5072	329.076	$14(37)_2$	-20.4209	316.2378	23(71)	-17.9496	326.0116
$3(6)_1$	-25.5177	329.076				24(97)	-21.9448	322.3409
			$15(42)_3$	-22.7973	317.6797	25(104)	-25.0974	322.2835
4(7)	-20.6378	318.3111	$16(43)_3$	-22.7882	317.6796	26(109)	-25.7241	319.559
5(8)	-21.9515	318.3043	$17(44)_3$	-22.7791	317.6795			
6(9)	-22.3497	318.3022				$27(111)_5$	-20.6762	324.2167
7(11)	-22.4336	318.3018	18(45)	-22.4173	317.6754	$28(112)_5$	-20.6891	324.2165
8(13)	-23.3764	318.297	19(48)	-20.222	317.6355			
9(14)	-25.819	318.2844				29(115)	-25.3765	321.4151
10(15)	-26.0627	318.2831	$20(55)_4$	-24.9353	315.0066	30(119)	-23.1505	318.743
11(32)	-21.3591	316.2457	$21(56)_4$	-24.9166	315.0064			
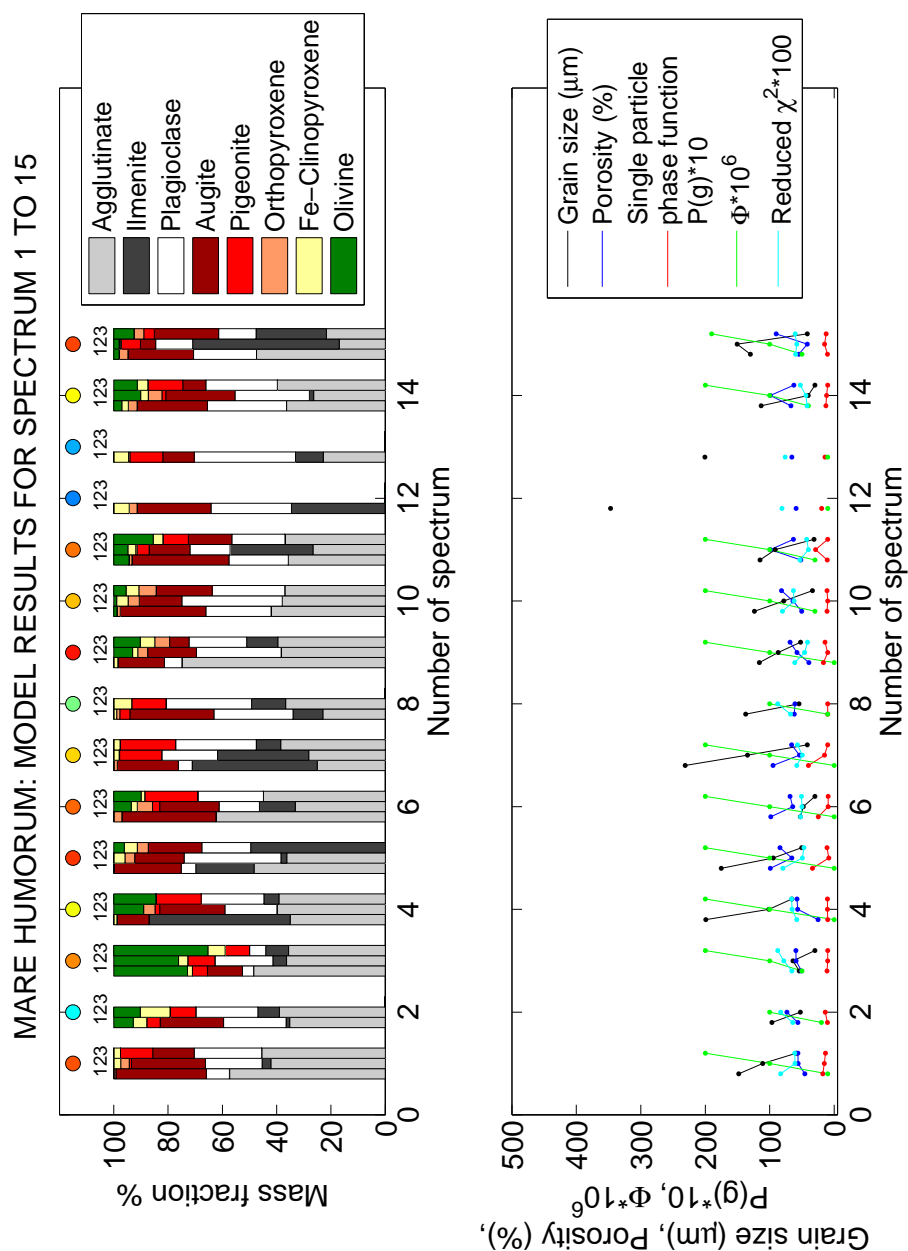
Figure 6.3: Model results for selected spectra 1 to 15. **Upper panel:** Bar diagrams with mineral mass fractions. Grouped bars represent different model attempts for the same spectrum. The 3 different runs were started with variable iron volume fraction values: (1) 0, (2) 0.0001, (3) 0.0002. In principle, the run exhibiting the lowest χ^2 should represent the best model fit. Model runs with $\chi^2 > 1$ are excluded. **Lower panel:** Further model parameters as grain size, porosity, single particle phase function and iron volume fraction are displayed. Additionally the χ^2 value of each run is plotted. Single particle phase function, iron volume fraction, and χ^2 are scaled for representation in one image.
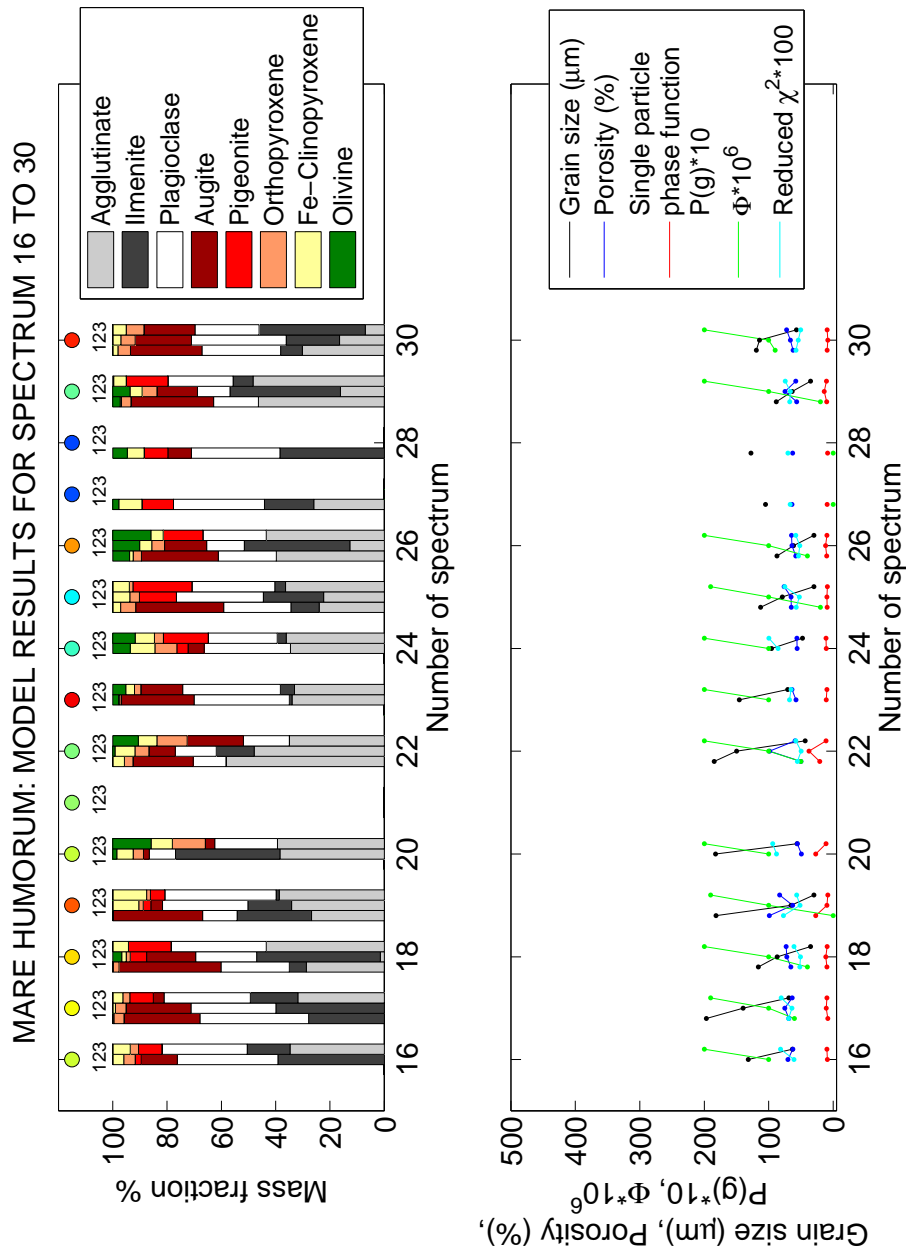
Figure 6.4: Model results for selected spectra 16 to 30. **Upper panel:** Bar diagrams with mineral mass fractions. Grouped bars represent different model attempts for the same spectrum. The 3 different runs were started with variable iron volume fraction values: (1) 0, (2) 0.0001, (3) 0.0002. In principle, the run exhibiting the lowest χ^2 should represent the best model fit. Model runs with $\chi^2 > 1$ are excluded. **Lower panel:** Further model parameters as grain size, porosity, single particle phase function and iron volume fraction are displayed. Additionally the χ^2 value of each run is plotted. Single particle phase function and iron volume fraction, and χ^2 are scaled for representation in one image. No sufficient fit could be derived for spectrum 21.
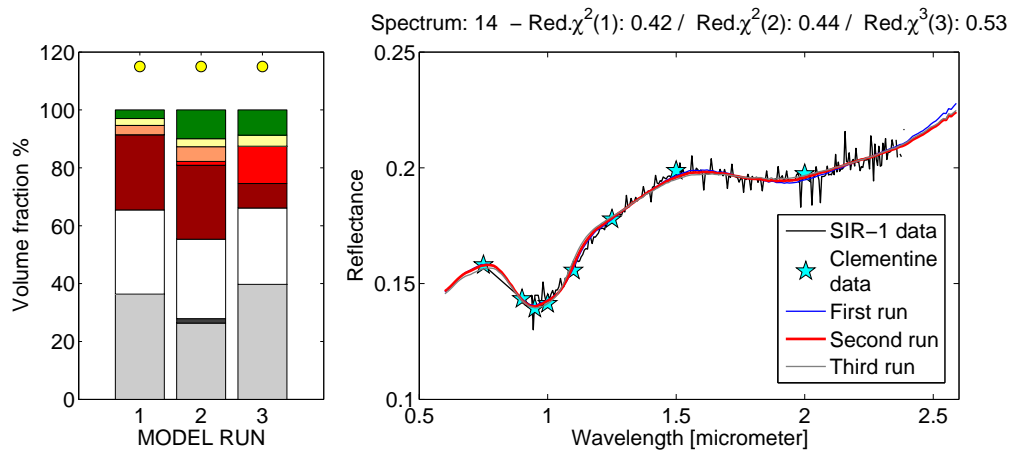
Figure 6.5: 1st Example spectrum for Mare Humorum: Spectrum number 14 (see Figure 6.3), is fitted with three different start values for the iron volume fraction parameter, which defines the degree of space weathering. All three cases produce good model fits with the low space weathering case showing the lowest reduced χ^2. All model runs produce comparable results, but show variations in pyroxene composition and olivine content.
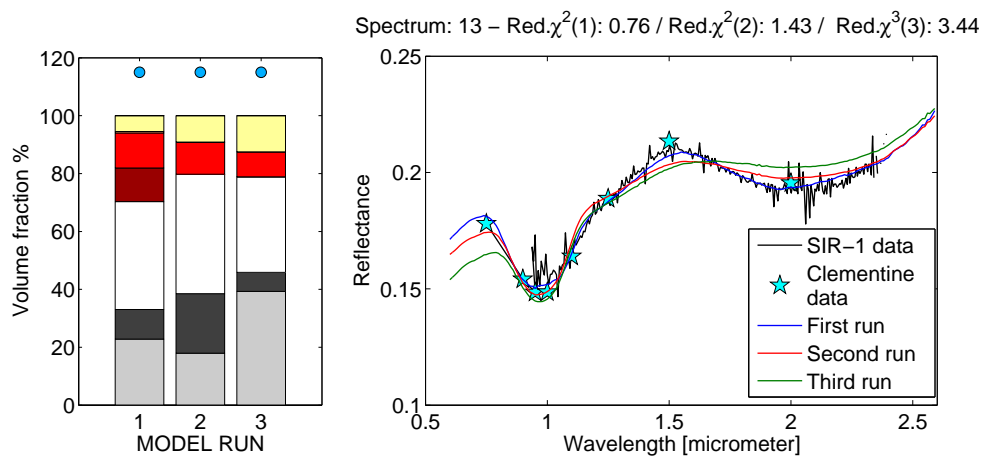

Figure 6.6: 2nd Example spectrum for Mare Humorum. Spectrum number 13 (see Figure 6.3), is fitted with three different start values for the iron volume fraction parameter. Only one set of start parameters produces an acceptable fit with a reduced χ^2 of 0.76, the other fits have $\chi^2 > 1$ and are thus excluded in Figure 6.3.

6.2   Case study of Mare Crisium

The basalts of Mare Crisium (Figure 6.7) have flooded the floor of the multiring Crisium basin. The lava deposit extents about 550 km in east/west direction and about 430 km in north/south direction. Unlike the Mare Humorum, Mare Crisium was sampled by the unmanned Luna 24 mission (Landing site / Lat: 12.7° Long: 62.4°). The probe returned 170 g of fine-grained regolith, the basalt fragments of the drill core were about 3.4-3.6 Gyr old. The mare basalts contained between 4 and 10 % olivine, between 34 to 39 % plagioclase, 48 to 60 % pyroxene and less than 2 % opaques (Papike and Vaniman 1978). Multispectral image studies (Bussey and Spudis 2000) suggest a FeO content between 14 and 18 %, and a TiO_2 content between 1 and 8 %. Again the uncertainties concerning element abundances from color ratios must be taken into account. With active-spectra analysis 161 SIR-1 footprint spectra with strong absorptions were found. Of these spectra, 148 could be aligned with Clementine data. On average, a longitude shift of -0.2 degrees was necessary to match both datasets. The shift in latitude resides between 0.25 and -0.1 degrees (see Figure 6.12, left lower panel). As for Humorum the spectra are color-coded according to the 2 micrometer value of relative spectra scaled to unity at 1.5 micrometer. Scaled relative spectra, cross-calibrated SIR-1 spectra and Clementine measurements are shown in Figure 6.12. To include Clementine measurements at 0.75, 0.9 and 0.95 micrometer in the analysis, only spectra for which the summed deviances between the five Clementine filters within SIR-1 wavelength range and the corresponding SIR-1 values are smaller than 0.03. After this selection 63 spectra remain. The SIR-1 spectra were supplemented by three Clementine filter measuremts to put additional constrains on the short wavelength wing of the 1 micrometer absorption band. Spectra were modeled for three different iron volume fractions (0, 0.0001, 0.0002) representing three stages of low space weathering. Model results for those spectra exhibiting $\chi^2 < 1$ are displayed in Figures 6.8–6.11. In Figure 6.7 Mare Crisium is shown together with the selected footprints.

Two surface features dominate the selection of active spectra of Mare Crisium. Strictly speaking they are not part of the main basalt body of Mare Crisium but located in the north-east of it. The small crater Eimmart A, a fresh impact crater at the rim of older Eimmart crater exhibits strong absorptions, especially in its central cavity, and a complete data series of spectra crossing the ejecta blanket and the central cavity is available. After removing spectra for which the sum of the differences to the Clementine filter measurements within SIR-1 wavelength range are larger then 0.03. In Figure 6.13 the remaining nineteen spectra together with an image and the footprint positions are displayed.

The crater spectra split up into two groups if sorted for 2 micrometer band depth. Spectra of the crater floor and inner wall seem to exhibit less strong space weathering as apparent in the weaker slope (Figure 6.13, right panel). The dark blue spectra appear unweathered and exhibit very strong absorptions. Points in the crater image (Figure 6.13, left panel) represent only footprint positions, but not the size of a footprint. In this special case the footprint has half the diameter of the dark crater floor. The size of the footprint is also shown in Figure 5.2, where the same crater is displayed. Due to the gradual propagation over ground, different proportions of the bright crater wall enter into the footprint ellipse. Thus the observed surface is probably uniform in composition, but not in albedo, due to
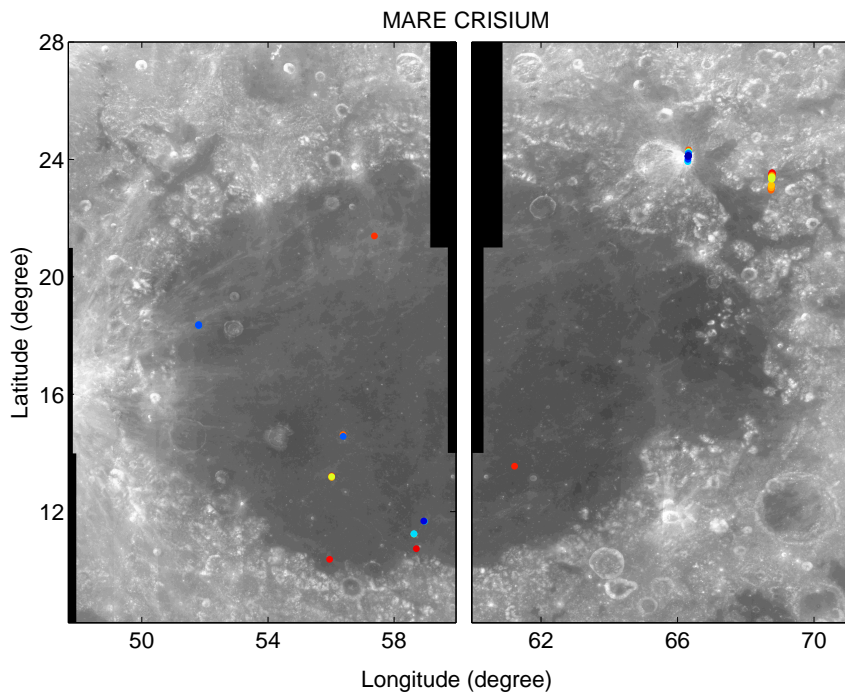
Figure 6.7: Clementine images showing Mare Crisium. Two images were necessary, because the different projection parameters hinder connection of images due to image distortions. The colored dots represent the positions of 63 footprints with strong absorption features. The colors are coded according to the 2 micrometer value in scaled relative spectra as seen in Figure 6.12.

different solar incident angles onto the flat crater floor and the inclined crater wall. This situation can be regarded as an "areal" mixture of two different surfaces, with differing albedo but analog composition. Hence these spectra represent an excellent test case for checking the influence of albedo onto the model results.

Spectra 38 till 44 stem from within the crater cavity. The SIR-1 orbit crossed the crater from north to south. While spectrum 44 is the single spectrum at the southern wall, the footprints on the northern wall incorporate more and more of the darker crater floor, and the albedo of the reflectance spectra decreases (dark blue spectra in right panel of Figure 6.13). Model results for these spectra are displayed in Figure 6.10 (spec.38-43). All of these spectra are modeled with about 40 % pyroxene, mainly augite with stable but smaller amounts of orthopyroxene and Fe-clinopyroxene. Spectra 41 and 43 also exhibit some pigeonite. Pigeonite and augite have absorption bands at approximately the same wavelengths, but absorption bands are stronger for pigeonites, which contain more iron (see spectra in Figure 3.3). In spectrum 41, 43 and 44_2, augite is partly replaced with pigeonite, and the overall pyroxene content decreases, because less pigeonite is needed to reproduce the strong absorptions of these footprint spectra. The fact, that only the very low space-weathering runs (ϕ=0) for spectra of the Eimmart A crater cavity gave a good fit, indicates that we found rather a global minimum, than a local minimum. Hence these model results are more reliable than those cases were many start configurations lead to

good χ^2 values. The high ilmenite in the models for spectra 40, 42 and 43 is probably due to compensation for the different fractions of bright surface within the different footprints. Once again the problem of disentangling agglutinate content, photometric effects, and ilmenite content becomes visible.

Assuming that the composition found for the less weathered materials on the crater walls and floor of Eimmart A represents the local lithology, and examining the model results of spectra from the crater ejecta (spec.28-37) we can follow along two lines of argumentation. First, all other spectra selected for Mare Crisium exhibit olivine between a few and 30 % indicating a probably generally higher olivine content for those regoliths. For Luna 24 basalt samples, Papike and Vaniman (1978) give an olivine content of 10 % for basalt fragments found in the drill core from Mare Crisium. Thus the high modeled olivine is not unrealistic. So probably Eimmart A penetrated through a high olivine basalt layer and uncovered olivine-free lithologies in his central cavity. The ejecta of Eimmart A are intermediate between the olivine-richer surface material and the excavated olivine-free material due to mixing of both lithologies in the ejecta blanket.

One could also argue that, within the more weathered ejecta blankets (Figure 6.13, center panel), olivine is mimicking the space weathering effect, because the SIR-1 wavelegth range reaches only to 0.94 micrometer and does not comprise the whole olivine band. This would imply that for a spectrum with a certain space weathering degree the olivine content modeled would increase with decreasing start values for the iron volume fraction. The contrary is observed: with increasing start values for iron volume fraction (Run 1 to 3), the modeled olivine content also increases. Thus olivine does not compensate for space weathering, but rather increases with it. One reason could be, that with increasing space weathering the generally weaker two micrometer pyroxene band is more and more obliterated by the increasing slope, and with this constraint diminishing, the broader band at 1 micrometer can also be modeled with olivine.

Another 27 selected spectra (spec.1-27) stem from a uniform mare region in Mare Anguis north of Mare Crisium. No fresh features are visible in the area were the footprint spectra are observed. Also this area extends over 0.6 degrees and without bright ejecta it should exhibit very strong space weathering as most of the lunar surface. This is an unusual candidate for beeing selected with the automated procedure. Usually small young craters, their ejecta blanket, or steeper slopes make up most active spectra selected. One possibility is that within this orbit fewer spectra exhibited very strong absorptions, so that those footprints were selected. Furthermore, the surface material could contain more iron so that even after long surface exposure, strong absorptions are still visible. Nevertheless, color-ratio images (Bussey and Spudis 2000) rather indicate a somewhat lower FeO content within this region of about 14 to 16 % compared to central Mare Crisium with over 18 %. The cross-calibrated spectra of this region exhibit uniform shape and albedo (see Figure 6.12, right upper panel, broad yellow/red stripe starting at 0.15 absolute reflectance). Consequently the model results are uniform for this area (Figure 6.8 and 6.9) and yield an olivine-rich composition with augite and orthopyroxene. As already observed, the exact olivine content varies with the start value of the iron volume fraction.

Table 6.2: Mare Crisium: Table with spectrum numbers and corresponding coordinates for identification of model results in Figures 6.8–6.11 with positions within Mare Crisium in Figure 6.7. The numbers in parentheses represent the indices of these spectra in the original selection of 125 active spectra and indicate how many spectra were omitted because the agreement between SIR-1 and Clementine measurements was not sufficient for combined modeling. Small numbers indicate objects of which more than one footprint spectrum is available.

Spec.	Lat	Long	Spec.	Lat	Long	Spec.	Lat	Long
1(1)	23.5436	68.2522	23(23)	23.0519	68.2511			
2(2)	23.535	68.2521	24(24)	23.0354	68.2511			
3(3)	23.5267	68.2521	25(25)	23.0187	68.251			
4(4)	23.5019	68.2521	26(26)	22.9934	68.251	$47(81)_2$	18.3728	52.1135
5(5)	23.4688	68.252	27(27)	22.9518	68.2509	$48(82)_2$	18.3635	52.1135
6(6)	23.4605	68.252				$49(83)_2$	18.3553	52.1134
7(7)	23.4525	68.252	$28(28)_1$	24.3217	65.5509	$50(84)_2$	18.3375	52.1134
8(8)	23.4355	68.2519	$29(32)_1$	24.264	65.5508			
9(9)	23.4269	68.2519	$30(33)_1$	24.2561	65.5507	$52(98)_3$	14.5681	56.6722
10(10)	23.4105	68.2519	$31(34)_1$	24.2478	65.5507	$53(100)_3$	14.6262	56.6717
11(11)	23.4021	68.2519	$32(35)_1$	24.2311	65.5507			
12(12)	23.3934	68.2518	$33(36)_1$	24.2232	65.5507	54(101)	10.741	58.8404
13(13)	23.3854	68.2518	$34(37)_1$	24.2146	65.5506	55(110)	13.5513	60.9312
14(14)	23.3693	68.2518	$35(38)_1$	24.2068	65.5506			
15(15)	23.3606	68.2518	$36(39)_1$	24.1982	65.5506	$56(112)_4$	11.2484	58.7904
16(16)	23.3522	68.2518	$37(40)_1$	24.1906	65.5506	$57(113)_4$	11.2357	58.7923
17(17)	23.3435	68.2517	$38(47)_1$	24.1318	65.5504			
18(18)	23.3359	68.2517	$39(48)_1$	24.1242	65.5504	$58(115)_5$	13.2132	56.2324
19(19)	23.3272	68.2517	$40(49)_1$	24.1156	65.5504	$59(116)_5$	13.1981	56.2315
20(20)	23.1349	68.2513	$41(50)_1$	24.1077	65.5504	$60(118)_5$	13.1669	56.2297
21(21)	23.1186	68.2513	$42(51)_1$	24.0987	65.5504			
22(22)	23.0691	68.2512	$43(52)_1$	24.0908	65.5503	61(119)	10.3777	56.055
			$44(61)_1$	24.0082	65.5501	62(137)	21.3932	58.1913
			$45(66)_1$	23.9421	65.55			
			$46(67)_1$	23.9252	65.55	$63(144)_6$	11.669	59.1478
						$51(90)_6$	11.681	59.1271

Most spectra of the dark basalts in the Mare Crisium region yield model results with unusually high olivine contents. Only little ilmenite is found, which is consistent with the findings from Luna 24, that Mare Crisium basalts are very low in titanium.
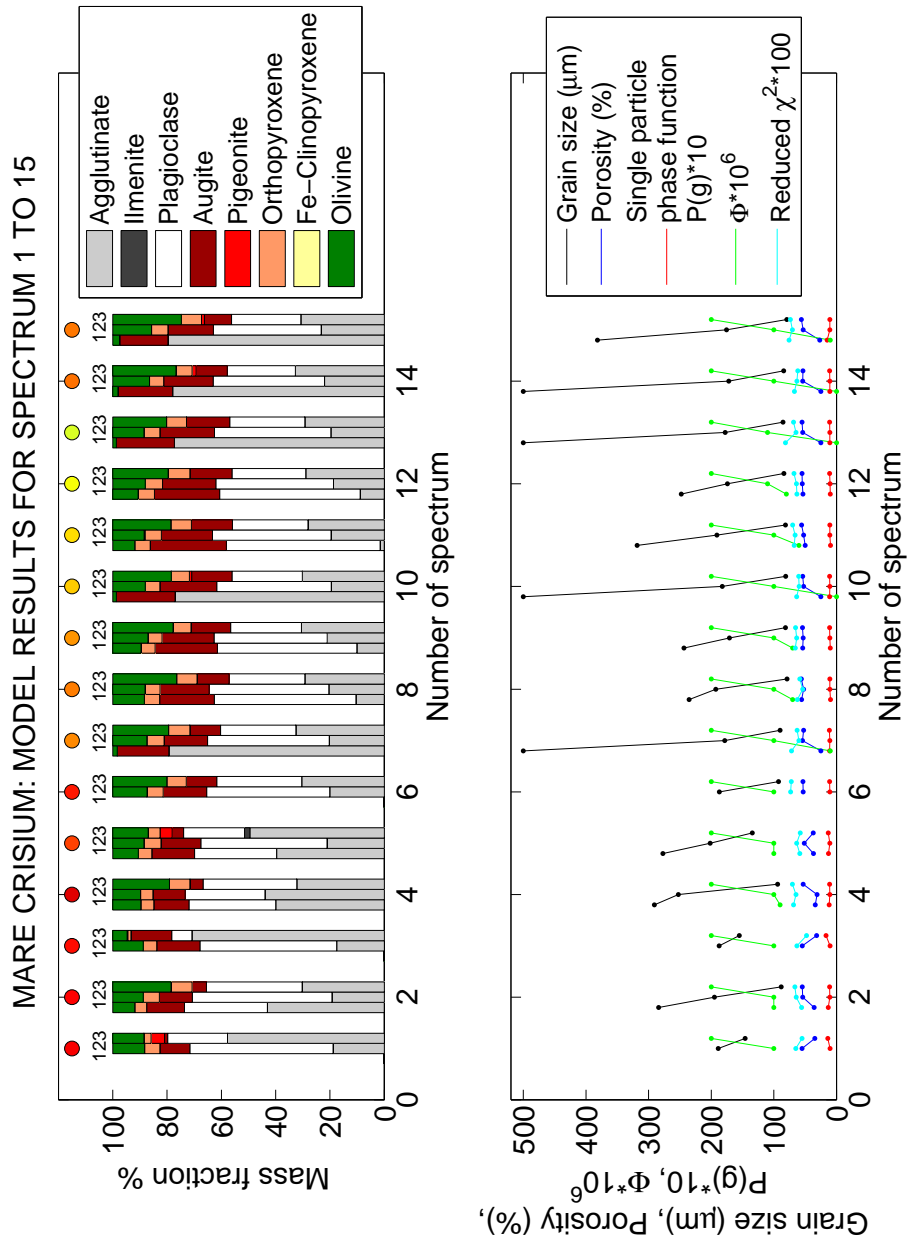
Figure 6.8: Model results for selected spectra 1 to 15. **Upper panel:** Bar diagrams with mineral mass fractions. Grouped bars represent different model attempts for the same spectrum. The 3 different runs were started with variable iron volume fraction values: (1) 0, (2) 0.0001, (3) 0.0002 . In principle the run, exhibiting the lowest χ^2 should represent the best model fit. Model runs with $\chi^2 > 1$ are excluded. **Lower panel:** Further model parameters as: grain size, porosity, single particle phase function, and iron volume fraction are displayed. Additionally, the χ^2 value of each run is plotted. Single particle phase function, iron volume fraction, and χ^2 are scaled for representation in one image.
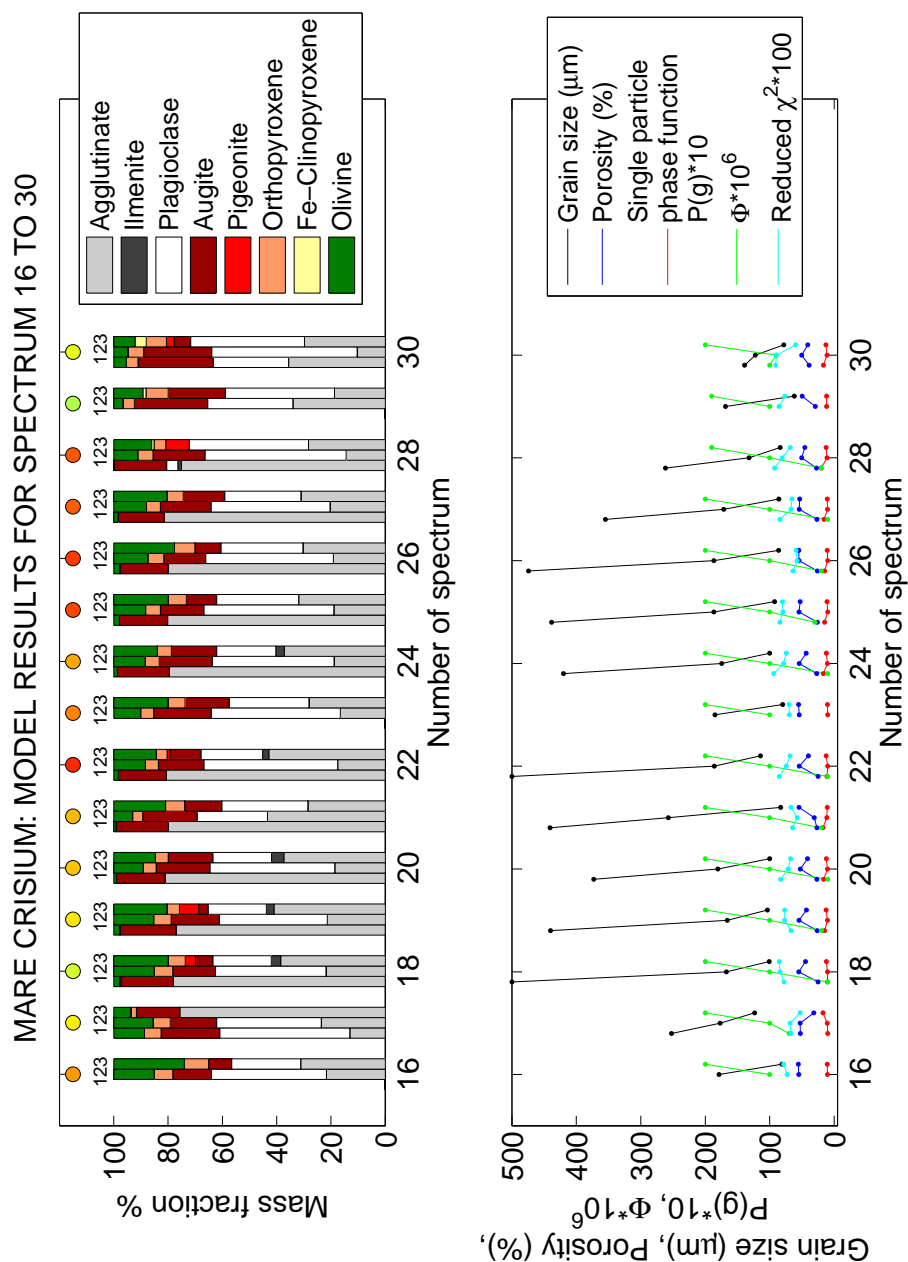
Figure 6.9: Model results for selected spectra 16 to 30. **Upper panel:** Bar diagrams with mineral mass fractions. Grouped bars represent different model attempts for the same spectrum. The 3 different runs were started with variable iron volume fraction values: (1) 0, (2) 0.0001, (3) 0.0002 . In principle the run, exhibiting the lowest χ^2 should represent the best model fit. Model runs with $\chi^2 > 1$ are excluded. **Lower panel:** Further model parameters as: grain size, porosity, single particle phase function, and iron volume fraction are displayed. Additionally, the χ^2 value of each run is plotted. Single particle phase function, iron volume fraction, and χ^2 are scaled for representation in one image.
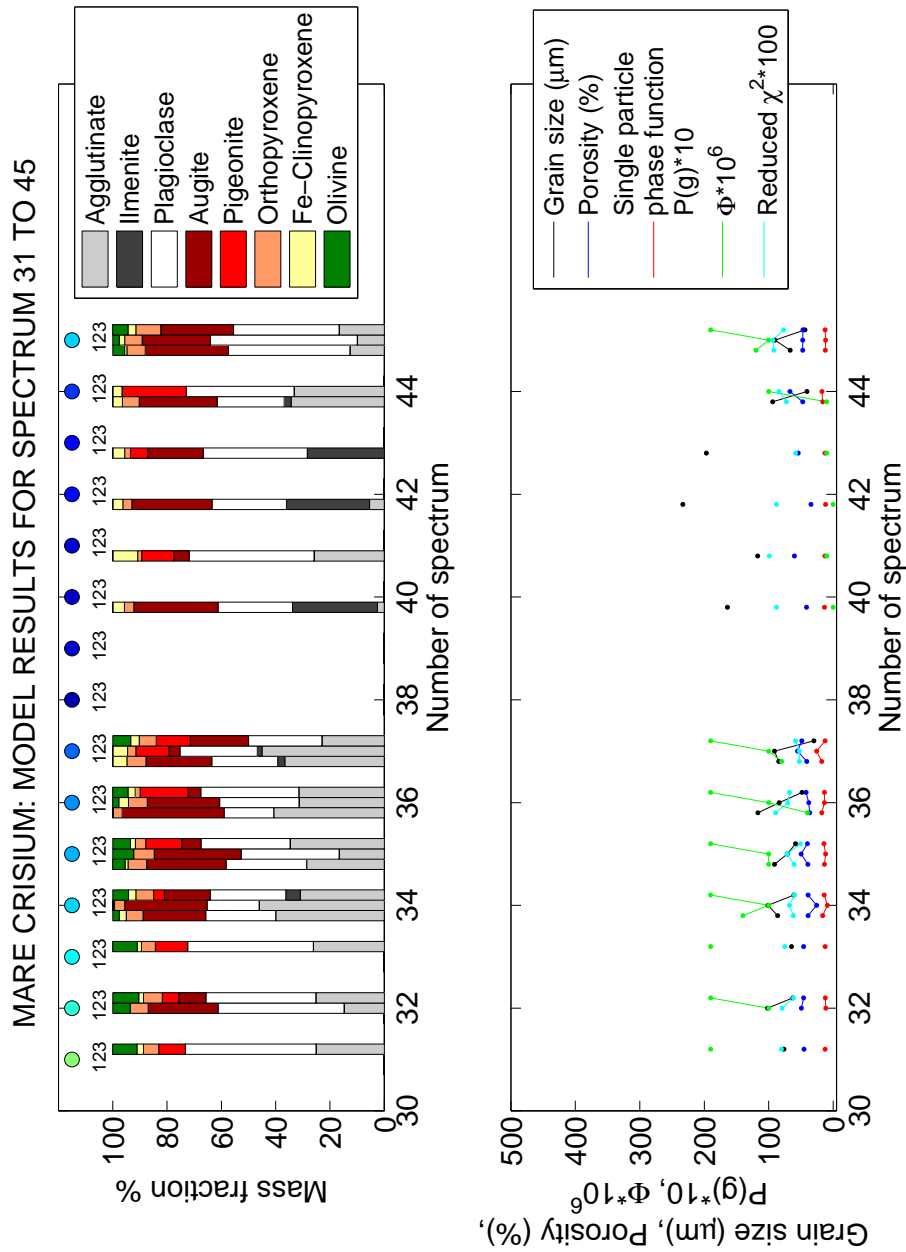
Figure 6.10: Model results for selected spectra 31 to 45. **Upper panel:** Bar diagrams with mineral mass fractions. Grouped bars represent different model attempts for the same spectrum. The 3 different runs were started with variable iron volume fraction values: (1) 0, (2) 0.0001, (3) 0.0002 . In principle the run, exhibiting the lowest χ^2 should represent the best model fit. Model runs with $\chi^2 < 1$ are excluded. **Lower panel:** Further model parameters as: grain size, porosity, single particle phase function, and iron volume fraction are displayed. Additionally, the χ^2 value of each run is plotted. Single particle phase function, iron volume fraction, and χ^2 are scaled for representation in one image.
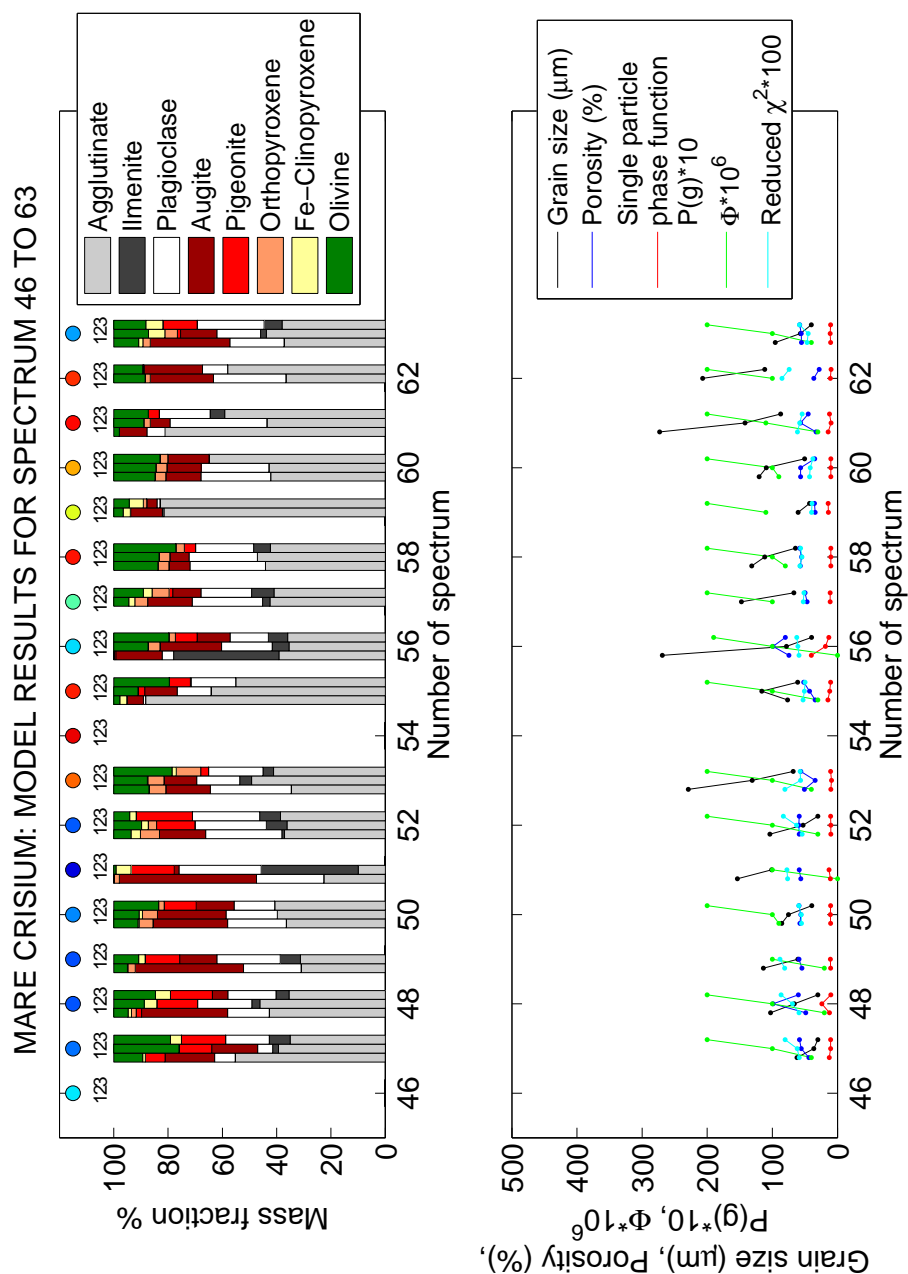
Figure 6.11.: Model results for selected spectra 46 to 63. **Upper panel:** Bar diagrams with mineral mass fractions. Grouped bars represent different model attempts for the same spectrum. The 3 different runs were started with variable iron volume fraction values: (1) 0, (2) 0.0001, (3) 0.0002. In principle the run, exhibiting the lowest χ^2 should represent the best model fit. Model runs with $\chi^2 > 1$ are excluded. **Lower panel:** Further model parameters as: grain size, porosity, single particle phase function, and iron volume fraction are displayed. Additionally, the χ^2 value of each run is plotted. Single particle phase function, iron volume fraction, and χ^2 are scaled for representation in one image.
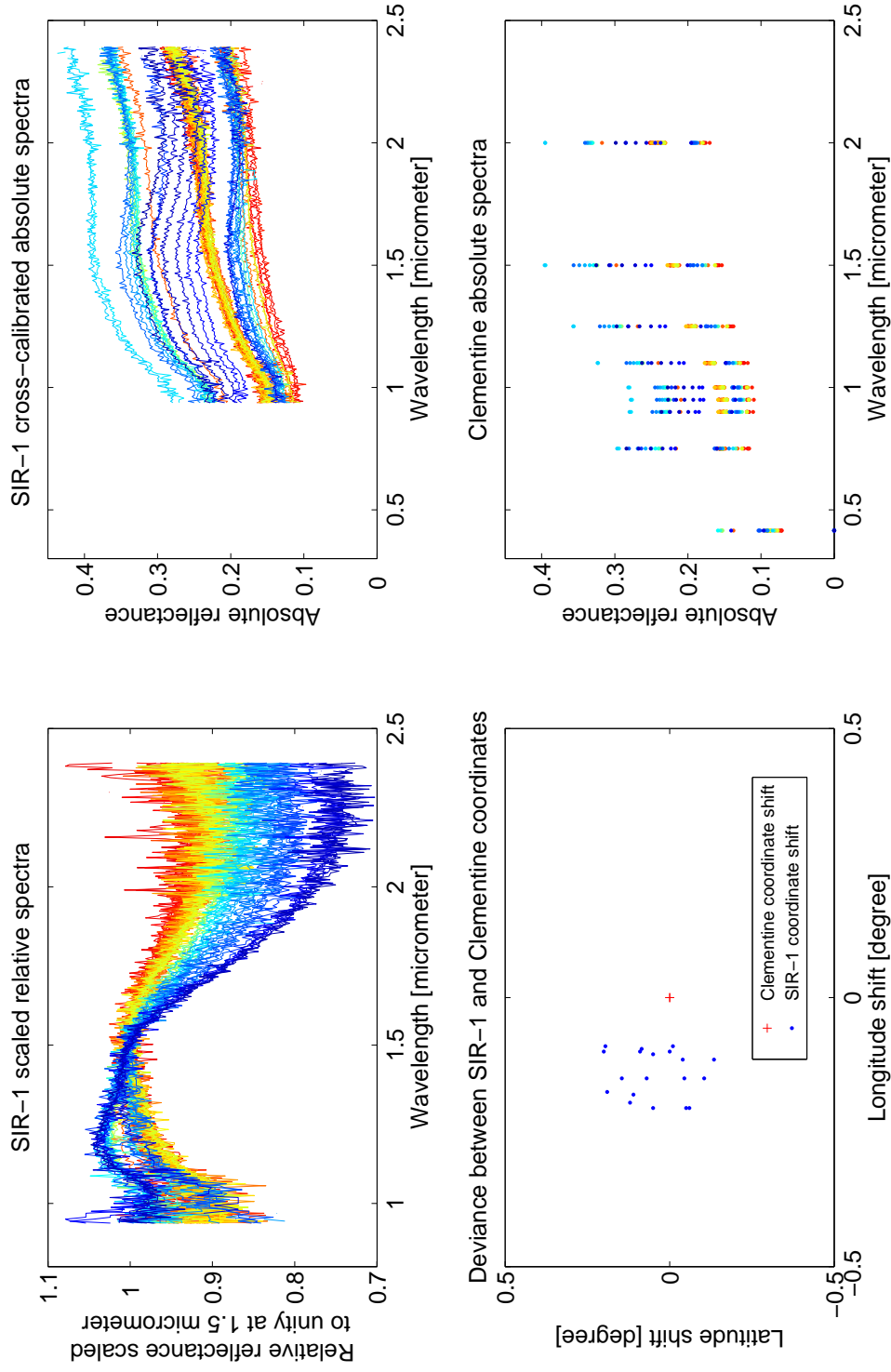
Figure 6.12: Active spectra selected for Mare Crisium. Spectra are color-coded according to the 2-micrometer value of scaled relative spectra. **Left upper panel:** relative spectra scaled to unity at 1.5 micrometer. **Right upper panel:** cross-calibrated absolute SIR-1 spectra (color-coding as in left upper panel). **Left lower panel:** Coordinate shifts necessary to align SIR-1 and Clementine UVVIS/NIR lighcurves. The red cross represents the Clementine coordinates. **Right lower panel:** Clementine measurements at the selected footprints.
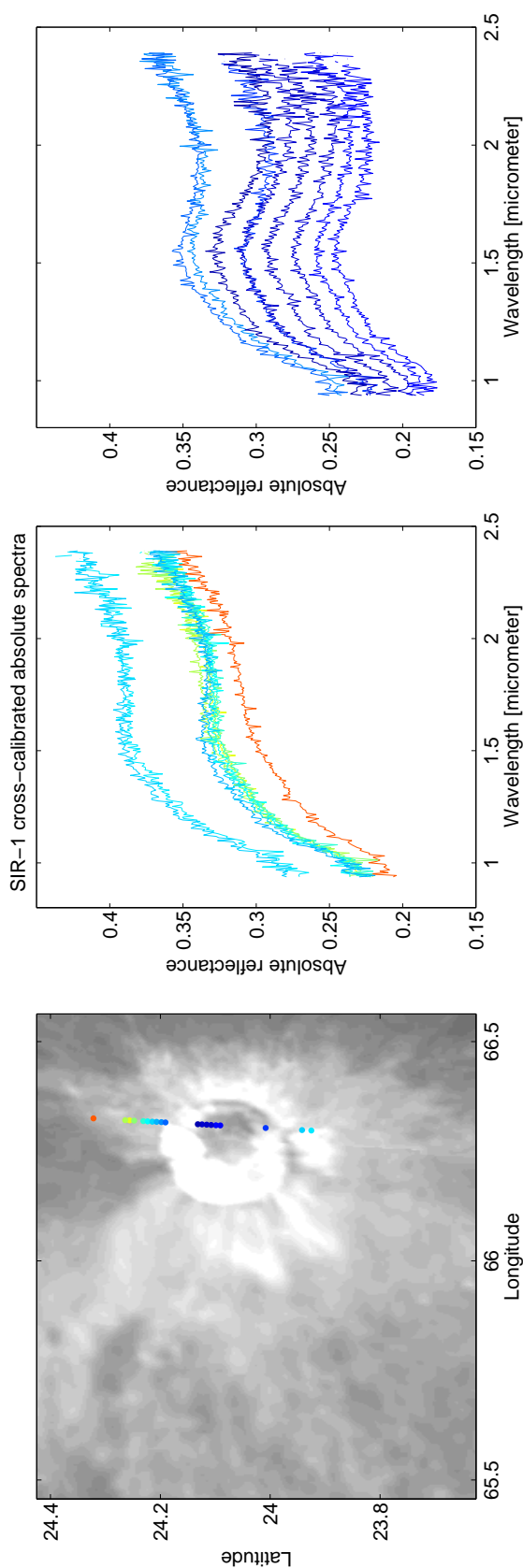
Figure 6.13: Left panel: Crater Eimmart A at the rim of Eimmart crater at the northern borders of Mare Crisium. This crater has a diameter of approximately 7 km and was already displayed in Figure 5.2. The spectra of this crater split into two groups according to their value at 2 micrometer in the scaled relative spectra (Figure 6.12). The spectra at the crater rim (center panel) show slightly redder slopes probably due to stronger space weathering. The spectra in the bowl-shaped crater itself (right panel) have nearly no red slopes and are thus less space weathered. Also they show stronger absorptions. The crater was observed during orbit 746 with a solar illumination of 35 degrees, which is close to local noon. For Clementine observed usually close to local noon we can assume that the illumination conditions in the Clementine image are close to those during SIR-1 observation. The weaker space weathering might be explained by gravitational slumpings that prevent material from maturing at the steep crater walls and deposit fresh material onto the crater floor.

7   Conclusions and future prospects

During this work, for the first time remotely sensed data from different instruments have been compared in many surface areas. It was shown that the measurements agree in general, and thus our remote observations are a reliable tool for studying the surface of the moon. Nevertheless, differences in observing geometry, which are usually corrected for an assumed flat surface, need to be refined and adapted to local large scale surface roughness.

In the beginning it became obvious, that the coordinate systems of SIR-1 and Clementine UVVIS/NIR data deviated slightly. To compare images with foot-point spectra confidence that both instruments observe the same surface spot is crucial. Clementine lightcurves were extracted along SIR-1 orbits by calculating the shape of each elliptical SIR-1 footprint and identifying Clementine pixels within each footprint. The coordinate shifts necessary to match both datasets vary systematically with lunar surface coordinates, but still scatter to much for a direct analytic correction. Thus each orbit is aligned individually with a automatic correlation routine. In principle this routine can be adopted for other instruments that measure intensity variations and are to be compared to images.

A regolith reflectance modeling program based on the bidirectional reflectance theory was developed together with a graphical user interface for easy access by other scientists. It was shown that in principle the surface mineralogy can be derived from remotely sensed spectra of unweathered surfaces, but that the obliterating space weathering effect complicates the analysis and lowers the reliability of the results.

From the 28 million spectra observed during the SIR-1 mission, a dataset of about 10000 active spectra with strong absorptions was extracted. This gives the opportunity to study the lunar surface, employing locations where recent events unveiled fresh surfaces, as probes into the local mineralogy. Further testing of the model will improve results, and we might be able to extend this analysis to stronger weathered surfaces.

The case studies conducted for active spectra at Mare Humorum and Mare Crisium have shown that measurements of extended less weathered surfaces like larger young craters, as for example Eimmart A, offer the opportunity to test local photometric models yet to be developed. Those models are especially important, for the most promising sample areas usually have topographies very different from a flat surface.

The detection of a set of unusual active spectra in an undisturbed, probably older surface area in Mare Anguis and the consistent modeling off those spectra give confidence that the

model can be applied to more mature surfaces. Nevertheless, extensive testing employing the 10000 active spectra identified within SIR-1 measurements will help to further improve the reliability of the model.

A renewed selection of spectra could concentrate on fresh highland material. Although less mafic and thus showing only very weak to none absorptions and less variability, they could be used to study the highly shocked lunar highlands with fresh material excavated from megaregolith through the 10 to 15 meter strong regolith layer. Modeling the small differences in anorthosite-rich samples to entangle the global distribution of large scale basin ejecta will be a challenging task for the future.

The artificial spectral sensitivity curves, derived for observations with different detector temperatures and at different phases of the mission can be used to analyze the systematic variation of the instrument sensitivity.

Bibliography

Adams, J. B., 1974, Visible and near-infrared diffuse reflectance spectra of pyroxenes as applied to remote sensing of solid objects in the solar system, J. Geophys. Res., 79, 4829–4836

Antonenko, I., Head, J. W., Mustard, J. F., Ray Hawke, B., 1995, Criteria for the Detection of Lunar Cryptomaria, Earth Moon and Planets, 69, 141–172

Basu, A., Wentworth, S. J., McKay, D. S., 2002, Heterogeneous agglutinitic glass and the fusion of the finest fraction (F3) model, Meteoritics and Planetary Science, 37, 1835–1842

Blewett, D. T., Lucey, P. G., Hawke, B. R., Jolliff, B. L., 1997, Clementine images of the lunar sample-return stations: Refinement of FeO and TiO2 mapping techniques, J. Geophys. Res., 102, 16 319–16 326

Bussey, D. B. J., Spudis, P. D., 2000, Compositional studies of the Orientale, Humorum, Nectaris, and Crisium lunar basins, J. Geophys. Res., 105, 4235–4244

Carrier, W. D. I., 1973, Lunar Soil Grain Size Distribution, Moon, 6, 250–263

Cintala, M. J., Hoerz, F., 1992, An experimental evaluation of mineral-specific comminution, Meteoritics, 27, 395–403

Clark, R. N., Swayze, G. A., Gallagher, A., 1993, Mapping Minerals with Imaging Spectroscopy, U.S. Geological Survey,Office of Mineral Resources Bulletin 2039, pp. 141–150

Clark, R. N., Swayze, G. A., Wise, R., Livo, E., Hoefen, T., Kokaly, R., Sutley, S. J., 2007, USGS digital spectral library splib06a: U.S. Geological Survey, Digital Data Series 231

Dehon, R. A., Waskom, J. D., 1976, Geologic structure of the eastern mare basins, in Lunar and Planetary Science Conference, (Ed.) D. C. Kinsler, vol. 7 of Lunar and Planetary Science Conference, pp. 2729–2746

Denevi, B. W., Lucey, P. G., Sherman, S. B., 2008, Radiative transfer modeling of near-infrared spectra of lunar mare soils: Theory and measurement, Journal of Geophysical Research (Planets), 113, 2003–+

Hackwill, T., Guest, J., Spudis, P., 2006, Stratigraphy and evolution of basalts in Mare Humorum and southeastern Procellarum, Meteoritics and Planetary Science, 41, 479–488

Hapke, B., 1981, Bidirectional reflectance spectroscopy. I - Theory, J. Geophys. Res., 86, 3039–3054

Hapke, B., 1984, Bidirectional reflectance spectroscopy. III - Correction for macroscopic roughness, Icarus, 59, 41–59

Hapke, B., 1986, Bidirectional reflectance spectroscopy. IV - The extinction coefficient and the opposition effect, Icarus, 67, 264–280

Hapke, B., 1993, Theory of reflectance and emittance spectroscopy, Topics in Remote Sensing, Cambridge, UK: Cambridge University Press, |c1993

Hapke, B., 2001, Space weathering from Mercury to the asteroid belt, J. Geophys. Res., 106, 10 039–10 074

Hapke, B., 2002, Bidirectional Reflectance Spectroscopy5. The Coherent Backscatter Opposition Effect and Anisotropic Scattering, Icarus, 157, 523–534

Hapke, B., 2008, Bidirectional reflectance spectroscopy. 6. Effects of porosity, Icarus, 195, 918–926

Hapke, B., Wells, E., 1981, Bidirectional reflectance spectroscopy. II - Experiments and observations, J. Geophys. Res., 86, 3055–3060

Hapke, B. W., 1963, A theoretical photometric function for the lunar surface, J. Geophys. Res., 68, 4571–4586

Head, J. W., 1982, Lava flooding of ancient planetary crusts - Geometry, thickness, and volumes of flooded lunar impact basins, Moon and Planets, 26, 61–88

Heiken, G. H., Vaniman, D. T., French, B. M. (Eds.), 1991, Lunar Sourcebook: A User's Guide to the Moon, Cambridge University Press, |c1991

Hiroi, T., Pieters, C. M., 1994, Estimation of grain sizes and mixing ratios of fine powder mixtures of common geologic minerals, J. Geophys. Res., 99, 10 867–10 880

Hunt, G. R., Salisbury, J. W., 1970, Visible and near infrared spectra of minerals and rocks. I. Silicate minerals, Modern Geology, 1, 283–300

Hunt, G. R., Salisbury, J. W., Lenhoff, C. J., 1973, Visible and near infrared spectra of minerals and rocks. VI. Additional silicates, Modern Geology, 4, 85–106

Hunt, G. R., Salisbury, J. W., Lenhoff, C. J., 1974, Visible and near infrared spectra of minerals and rocks: IX. Basic and ultrabasic igneous rocks, Modern Geology, 5, 15–22

Johnson, J. R., Hörz, F., 2003, Visible/near-infrared spectra of experimentally shocked plagioclase feldspars, Journal of Geophysical Research (Planets), 108, 5120–+

Johnson, P. B., Cristy, R. W., 1974, Optical constants of metals: Ti, V, Cr, Mn, Fe, Co, Ni, and Pd, prb, 9, 5056–5070

Jolliff, B. L., Gillis, J. J., Haskin, L. A., Korotev, R. L., Wieczorek, M. A., 2000, Major lunar crustal terranes: Surface expressions and crust-mantle origins, J. Geophys. Res., 105, 4197–4216

Jolliff, B. L., Wieczorek, M. A., Shearer, C. K., Neal, C. R. (Eds.), 2006, New Views of the Moon, vol. 60 of Reviews in Mineralogy and Geochemistry, The Mineralogical Society of America

Keller, L. P., Clemett, S. J., 2001, Formation of Nanophase Iron in the Lunar Regolith, in Lunar and Planetary Institute Conference Abstracts, vol. 32 of Lunar and Planetary Institute Conference Abstracts, pp. 2097–+

Keller, L. P., McKay, D. S., 1997, The nature and origin of rims on lunar soil grains, gca, 61, 2331–2341

King, T. V. V., Ridley, W. I., 1987, Relation of the spectroscopic reflectance of olivine to mineral chemistry and some remote sensing implications, J. Geophys. Res., 92, 11 457–11 469

Klima, R. L., Pieters, C. M., Dyar, M. D., 2005, Pyroxene Spectroscopy: Effects of Major Element Composition on Near, Mid and Far-Infrared Spectra, in 36th Annual Lunar and Planetary Science Conference, (Eds.) S. Mackwell, E. Stansbery, vol. 36 of Lunar and Planetary Institute Science Conference Abstracts, pp. 1462–+

Klima, R. L., Pieters, C. M., Dyar, M. D., 2007a, Vis-NIR Spectroscopy of Synthetic Pyroxenes: Calcium Bearing Pyroxenes and Application to the HED Meteorites, in Lunar and Planetary Institute Science Conference Abstracts, vol. 38 of Lunar and Planetary Institute Science Conference Abstracts, pp. 1733–+

Klima, R. L., Pieters, C. M., Dyar, M. D., 2007b, Spectroscopy of synthetic Mg-Fe pyroxenes I: Spin-allowed and spin-forbidden crystal field bands in the visible and near-infrared, Meteoritics and Planetary Science, 42, 235–253

Korotev, R. L., Gillis, J. J., 2001, A new look at the Apollo 11 regolith and KREEP, J. Geophys. Res., 106, 12 339–12 354

Lawrence, D. J., Feldman, W. C., Barraclough, B. L., Binder, A. B., Elphic, R. C., Maurice, S., Thomsen, D. R., 1998, Global Elemental Maps of the Moon: The Lunar Prospector Gamma-Ray Spectrometer, Science, 281, 1484–+

Lawson, S. L., Jakosky, B. M., Park, H.-S., Mellon, M. T., 2000, Brightness temperatures of the lunar surface: Calibration and global analysis of the Clementine long-wave infrared camera data, J. Geophys. Res., 105, 4273–4290

Lucey, P. G., Blewett, D. T., Hawke, B. R., 1998, Mapping the FeO and TiO2 content of the lunar surface with multispectral imagery, J. Geophys. Res., 103, 3679–+

Lucey, P. G., Blewett, D. T., Jolliff, B. L., 2000a, Lunar iron and titanium abundance algorithms based on final processing of Clementine ultraviolet-visible images, J. Geophys. Res., 105, 20 297–+

Lucey, P. G., Blewett, D. T., Taylor, G. J., Hawke, B. R., 2000b, Imaging of lunar surface maturity, J. Geophys. Res., 105, 20 377–20 386

McKay, D. S., Fruland, R. M., Heiken, G. H., 1974a, Grain Size Distribution as an Indicator of the Maturity of Lunar Soils, in Lunar and Planetary Institute Conference Abstracts, vol. 5 of Lunar and Planetary Institute Conference Abstracts, pp. 480–+

McKay, D. S., Fruland, R. M., Heiken, G. H., 1974b, Grain size and the evolution of lunar soils, in Lunar and Planetary Science Conference, vol. 5 of Lunar and Planetary Science Conference, pp. 887–906

Morris, R. V., 1980, Origins and size distribution of metallic iron particles in the lunar regolith, in Lunar and Planetary Science Conference, (Ed.) S. A. Bedini, vol. 11 of Lunar and Planetary Science Conference, pp. 1697–1712

Mustard, J. F., Pieters, C. M., 1989, Photometric phase functions of common geologic minerals and applications to quantitative analysis of mineral mixture reflectance spectra, J. Geophys. Res., 94, 13 619–13 634

Nimura, T., Hiroi, T., Pieters, C. M., 2008, An improved scheme for modeling the reflectance spectra of space-weathered regoliths, Earth, Planets, and Space, 60, 271–275

Noble, S. K., Pieters, C. M., Hiroi, T., Taylor, L. A., 2006, Using the modified Gaussian model to extract quantitative data from lunar soils, Journal of Geophysical Research (Planets), 111, 11 009–+

Noble, S. K., Pieters, C. M., Keller, L. P., 2007, An experimental approach to understanding the optical effects of space weathering, Icarus, 192, 629–642

Papike, J. J., Vaniman, D. T., 1978, Luna 24 ferrobasalts and the mare basalt suite - Comparative chemistry, mineralogy, and petrology, in Mare Crisium: The view from Luna 24, (Eds.) R. B. Merrill, J. J. Papike, pp. 371–401

Petro, N. E., Pieters, C. M., 2007, Foreign Material in the Lunar Regolith: Lateral Transport by Post-Basin Cratering, in Lunar and Planetary Institute Conference Abstracts, vol. 38 of Lunar and Planetary Institute Conference Abstracts, pp. 2069–+

Petro, N. E., Pieters, C. M., 2008, The lunar-wide effects of basin ejecta distribution on the early megaregolith, Meteoritics and Planetary Science, 43, 1517–1529

Phillips, W. R., Griffen, D. T., 1980, Optical Mineralogy: The nonopaque minerals, W.H.Freeman and Company

Pieters, C. M., Belton, M., Fischer, E., Greeley, R., Jaumann, R., Head, J. W., Hoffmann, H., McEwen, A., Murchie, S., Neukum, G., Sunshine, J., 1992, Compositional Implications of SSI Multispectral Images of the Unexplored Lunar Farside, in Lunar

and Planetary Institute Conference Abstracts, vol. 23 of Lunar and Planetary Institute Conference Abstracts, pp. 1069–+

Pieters, C. M., Fischer, E. M., Rode, O., Basu, A., 1993, Optical effects of space weathering: The role of the finest fraction, J. Geophys. Res., 98, 20 817–+

Pieters, C. M., Tompkins, S., He, G., Head, J. W., Hess, P. C., 1997, Mineralogy of the mafic anomaly at South Pole-Aitken and implications for mantle excavation, in Lunar and Planetary Institute Conference Abstracts, vol. 28 of Lunar and Planetary Institute Conference Abstracts, pp. 1113–+

Pieters, C. M., Gaddis, L., Jolliff, B., Duke, M., 2001, Rock types of South Pole-Aitken basin and extent of basaltic volcanism, J. Geophys. Res., 106, 28 001–28 022

Pieters, C. M., Isaacson, P. J., Klima, R. L., Hiroi, T., Sarbadhikari, A. B., Liu, Y., Taylor, L. A., 2008, Lunar Rock and Mineral Characterization Consortium (LRMCC): Links to Global Science and Exploration, in Lunar and Planetary Institute Conference Abstracts, vol. 39 of Lunar and Planetary Institute Conference Abstracts, pp. 1900–+

Ryder, G., 1992, Chemical variation and zoning of olivine in lunar dunite 72415 - Near-surface accumulation, in Lunar and Planetary Science Conference Proceedings, (Eds.) G. Ryder, V. L. Sharpton, vol. 22 of Lunar and Planetary Science Conference Proceedings, pp. 373–380

Shepard, M. K., Helfenstein, P., 2007, A test of the Hapke photometric model, Journal of Geophysical Research (Planets), 112, 3001–+

Shkuratov, Y., Starukhina, L., Hoffmann, H., Arnold, G., 1999a, A Model of Spectral Albedo of Particulate Surfaces: Implications for Optical Properties of the Moon, Icarus, 137, 235–246

Shkuratov, Y. G., Bondarenko, N. V., 2001, Regolith Layer Thickness Mapping of the Moon by Radar and Optical Data, Icarus, 149, 329–338

Shkuratov, Y. G., Kreslavsky, M. A., Ovcharenko, A. A., Stankevich, D. G., Zubko, E. S., Pieters, C., Arnold, G., 1999b, Opposition Effect from Clementine Data and Mechanisms of Backscatter, Icarus, 141, 132–155

Smith, J. V., Anderson, A. T., Newton, R. C., Olsen, E. J., Crewe, A. V., Isaacson, M. S., Johnson, D., Wyllie, P. J., 1970, Petrologic history of the moon inferred from petrography, mineralogy and petrogenesis of Apollo 11 rocks, Geochimica et Cosmochimica Acta Supplement, 1, 897–+

Spudis, P. D., Reisse, R. A., Gillis, J. J., 1994, Ancient Multiring Basins on the Moon Revealed by Clementine Laser Altimetry, Science, 266, 1848–+

Sunshine, J. M., Pieters, C. M., 1998, Determining the composition of olivine from reflectance spectroscopy, J. Geophys. Res., 103, 13 675–13 688

Sunshine, J. M., Pieters, C. M., Pratt, S. F., 1990, Deconvolution of Mineral Absorption Bands: An Improved Approach, J. Geophys. Res., 95, 6955–6966

Sunshine, J. M., Pieters, C. M., Pratt, S. F., McNaron-Brown, K. S., 1999, Absorption Band Modeling in Reflectance Spectra: Availability of the Modified Gaussian Model, in Lunar and Planetary Institute Conference Abstracts, vol. 30 of Lunar and Planetary Institute Conference Abstracts, pp. 1306–+

Taylor, L. A., Pieters, C. M., Keller, L. P., Morris, R. V., McKay, D. S., 2001, Lunar mare soils: Space weathering and the major effects of surface-correlated nanophase Fe, J. Geophys. Res., 106, 27 985–28 000

Taylor, L. A., Pieters, C., Patchen, A., Taylor, D.-H., Morris, R. V., Keller, L. P., McKay, D. S., 2003, Mineralogical Characterization of Lunar Highland Soils, in Lunar and Planetary Institute Conference Abstracts, (Eds.) S. Mackwell, E. Stansbery, vol. 34 of Lunar and Planetary Institute Conference Abstracts, pp. 1774–+

Weidner, V. R., Hsia, J. J., 1981, Reflection properties of pressed polytetrafluoroethylene powder, Journal of the Optical Society of America (1917-1983), 71, 856–+

Wood, J. A., Dickey, Jr., J. S., Marvin, U. B., Powell, B. N., 1970, Lunar anorthosites and a geophysical model of the moon, Geochimica et Cosmochimica Acta Supplement, 1, 965–+

Publications

- Wiese, Manuela; Vilenius, Esa; Mall, Urs: Hapke modeling of lunar infrared spectra using SIR-1 and Clementine UVVIS/NIR data. In: *European Planetary Science Congress 2008*, p. 257

- Wiese, Manuela; Mall, Urs; Vilenius, Esa: Selected lunar craters as seen in joint data of SMART-1/SIR and Clementine/UVVIS/NIR. In: *European Planetary Science Congress 2006*, p. 239

- Wiese, Manuela; Neuhäuser, Ralph: Extrasolar Planets Host Stars – What do they look like in the X-ray? In: *Astronomische Nachrichten, Vol. 325, Supplement 1*, p. 325

- Seifahrt, Andreas; Mugrauer, Markus; Wiese, Manuela; Neuhäuser, Ralph; Guenther, Eike W.: New brown dwarf companions to dM(e) stars. In: *Astronomische Nachrichten, Vol. 326, Issue 10*, p. 974

Acknowledgments

Curriculum Vitae

Zur Person

Voller Name	Manuela Wiese
Geburtsdatum	25. Aug. 1978
Geburtsort	Frankfurt-Oder
Staatsangehörigkeit	Deutsch

Werdegang

1986 – 1992	Grundschule in Müllrose/Brandenburg
1992 – 1998	Gymnasium in Neuzelle/Brandenburg
1998 – 2005	Studium der Physik an der Ruprecht-Karls-Universität in Heidelberg/Baden-Würthemberg
2003 – 2005	Externe Diplomarbeit am Astrophysikalischen Institut und der Universitätssternwarte (AIU) in Jena/Thüringen zum Thema "Röntgenstrahlung von Sternen mit extrasolaren Planeten" unter Betreuung von Prof. Ralph Neuhäuser
2005	Diplom in Physik
2005-2009	Doktorarbeit am Max-Planck-Institut für Sonnensystemforschung in Katlenburg-Lindau/Niedersachsen im Rahmen der IMPRS-International Max-Planck Research School Betreuung durch Dr. Urs Mall und Prof. Andreas Pack

Göttingen, 1. April 2009

Manuela Wiese

Manuela Wiese: Lunar Mineralogy with SIR-1 and Clementine UVVIS/NIR

The mineralogy of the lunar surface can be investigated through remote sensing in the near infrared. Within this work infrared reflectance spectra of the SIR-1 point spectrometer are analyzed together with Clementine UVVIS/NIR images. Methods to combine these diverse data sets are developed. A regolith reflectance model based on the Bidirectional Reflectance Theory of Bruce Hapke is developed and tested on laboratory mixtures. Model results for spectra with prominent absorptions from Mare Humorum and Mare Crisium are presented. It was shown, that the mineral mass fractions of lunar surface regolith, can be derived from infrared reflectance spectra via modeling. The reliability of the derived mineralogy is large where the surface age is small. A database of spectra from immature surfaces exhibiting strong mineral absorption features and observed with SIR-1 was build. This spectra are less affected by space weathering, and can be used as probes of fresh material into the surrounding more mature surface.